

**Monte Carlo Studies  
of the Aggregation of Alkyltrimethylammonium Surfactants  
on Montmorillonite- and Muscovite-Water Interfaces**

Von der Fakultät für Mathematik und Physik  
der Gottfried Wilhelm Leibniz Universität Hannover  
zur Erlangung des Grades

**Doktorin der Naturwissenschaften  
Dr. rer. nat.**

genehmigte Dissertation  
von

**Birthe Klebow**

geboren am 24. Februar 1983 in Uelzen

2012

Referent:	Prof. Dr. Rolf Michel
Korreferent:	Prof. Dr. Herbert Pfnür
Tag der Promotion:	02.05.2012

# Abstract

Organically modified clays exhibit adsorption capacities for cations, anions, and non-polar organic compounds, which make them valuable for their use in various environmental technical applications. To improve the understanding of the adsorption processes, the molecular-scale characterization of the structures of the aggregates formed by organic cations on the external basal surfaces of clay particles is essential. In contrast to experimental methods, which face fundamental difficulties caused by the structural properties of clay particles, classical molecular simulations have proven to be a powerful tool for the exploration of mineral structures on a molecular scale. In this work, the structures of alkyltrimethylammonium ( $C_n\text{TMA}^+ = (\text{CH}_3)_3\text{N}(\text{CH}_2)_{n-1}\text{CH}_3^+$ ,  $n \in \{8, 12, 16\}$ ) aggregates assembled on montmorillonite–water and muscovite–water interfaces were investigated by means of Monte Carlo simulations.

$C_n\text{TMA}^+$  ions form inner-sphere or outer-sphere complexes on the basal surfaces of montmorillonite and muscovite or aggregate through hydrophobic interactions of their alkyl chains. Compared to montmorillonite, muscovite exhibits an approximately threefold higher charge density of its mineral layers. As a result, the binding of water molecules to the muscovite surface is considerably stronger, which impedes the formation of  $C_n\text{TMA}^+$  inner-sphere surface complexes on muscovite. Thus, less than 50 % of the adsorbed  $C_n\text{TMA}^+$  ions form inner-sphere complexes, whereas their fraction on montmorillonite amounts to approximately 90 %. The amount of adsorbed  $C_n\text{TMA}^+$  is independent of the alkyl chain length  $n$ . However, with decreasing chain length, increasing amounts of  $C_n\text{TMA}^+$  are detached from the aggregates and reside in solution. These simulation results successfully explain the experimentally observed increase of the amounts of  $C_n\text{TMA}^+$  aggregating at mineral–water interfaces with increasing alkyl chain length.

At low coverages, the  $C_n\text{TMA}^+$  ions adsorb on the mineral surfaces as monomers or dimers. With increasing coverages, aggregates form, which partially cover the mineral surfaces and are laterally separated from water regions. Due to the weaker hydrophobic interactions between short-chained  $C_n\text{TMA}^+$  ions, the conformational order of the alkyl chains of the aggregated  $C_n\text{TMA}^+$  ions substantially decreases with decreasing chain length. The simulations further indicate that considerable amounts of inorganic ions are located in the vicinity of the mineral–aggregate and aggregate–water interfaces. These observations finally allow to draw conclusions about the mechanisms of anion and cation adsorption by organically modified clays.

**Keywords:** Monte Carlo Simulation, Phyllosilicates, Alkyltrimethylammonium



# Kurzzusammenfassung

Organisch modifizierte Tone sind aufgrund ihrer Eigenschaften, sowohl Kationen und Anionen als auch ungeladene organische Verbindungen zu sorbieren, für eine Vielzahl umwelttechnischer Anwendungen von herausragender Bedeutung. Für ein besseres Verständnis der Sorptionsprozesse ist die Charakterisierung der auf den äußeren basalen Oberflächen von Tonteilchen gebildeten Aggregate organischer Kationen essentiell. Im Gegensatz zu experimentellen Methoden, die aufgrund der Struktureigenschaften von Tonteilchen auf grundlegende Schwierigkeiten stoßen, haben sich klassische molekulare Simulationen für die Untersuchung von Mineralstrukturen auf molekularem Maßstab in vorangegangenen Arbeiten erfolgreich bewährt. In dieser Arbeit wurden die Strukturen von Alkyltrimethylammonium-Aggregaten ( $C_n\text{TMA}^+ = (\text{CH}_3)_3\text{N}(\text{CH}_2)_{n-1}\text{CH}_3^+$ ,  $n \in \{8, 12, 16\}$ ), die in wässriger Lösung an den basalen Oberflächen von Montmorillonit und Muskovit gebildet werden, unter Anwendung von Monte-Carlo-Simulationen erforscht.

$C_n\text{TMA}^+$ -Ionen adsorbieren als inner-sphere- oder outer-sphere-Komplexe an den basalen Oberflächen von Montmorillonit und Muskovit oder aggregieren über hydrophobe Wechselwirkung ihrer Alkylketten. Die gegenüber Montmorillonit etwa dreifach erhöhte Oberflächenladung von Muskovit führt zu einer deutlich stärkeren Bindung von Wassermolekülen durch doppelte Wasserstoffbrückenbindung an die Mineraloberfläche. Infolgedessen bilden an Muskovit weniger als 50 % der adsorbierten  $C_n\text{TMA}^+$ -Ionen inner-sphere-Komplexe. An Montmorillonit hingegen beträgt ihr Anteil etwa 90 %. Die Menge der gebildeten Sorptionskomplexe ist unabhängig von der Länge  $n$  der Alkylketten. Mit abnehmender Kettenlänge steigt jedoch der Anteil der nicht aggregierten, sich in wässriger Lösung befindender organischer Kationen. Die experimentell beobachtete Zunahme der Menge von in wässriger Lösung an Mineraloberflächen aggregierten  $C_n\text{TMA}^+$ -Ionen mit zunehmender Kettenlänge  $n$  lässt sich durch diese Simulationsergebnisse erfolgreich erklären.

Bei geringen Belegungsgraden adsorbieren die  $C_n\text{TMA}^+$ -Ionen als Monomere oder Dimere an der Mineraloberflächen. Mit zunehmender Belegung bilden sich Aggregate, die lateral von den Bereichen wässriger Lösung getrennt sind. Durch die schwächere hydrophobe Wechselwirkung kürzerer Alkylketten untereinander sinkt die Ordnung der Alkylketten innerhalb der gebildeten  $C_n\text{TMA}^+$ -Aggregate mit abnehmender Kettenlänge. Die beobachteten hohen Konzentrationen anorganischer Ionen an den Mineral-Aggregat- und Aggregat-Wasser-Grenzflächen ermöglichen schließlich Rückschlüsse auf die Mechanismen der Anionen- und Kationensorption durch organisch modifizierte Tone.

**Schlagerworte:** Monte-Carlo-Simulation, Schichtsilikate, Alkyltrimethylammonium



# Contents

<b>List of Abbreviations</b>	<b>ix</b>
<b>List of Figures</b>	<b>xi</b>
<b>List of Tables</b>	<b>xv</b>
<b>1 Introduction</b>	<b>1</b>
1.1 Background and Motivation . . . . .	1
1.2 Aspects of Radioactive Waste Disposal . . . . .	2
1.2.1 Disposal in Deep Geological Formations . . . . .	2
1.2.2 Potential Application of Organoclays as Part of Geotechnical Barriers . . . . .	5
1.3 Application of Classical Molecular Simulations in Clay Research . . . . .	8
1.4 Aim and Structure of the Thesis . . . . .	9
<b>2 Theoretical Methods</b>	<b>11</b>
2.1 Overview . . . . .	11
2.2 Classical Molecular Simulations . . . . .	12
2.3 Monte Carlo Algorithms . . . . .	13
2.3.1 Metropolis Monte Carlo . . . . .	13
2.3.2 Configurational Bias Monte Carlo . . . . .	16
2.4 Description of the Interactions Between Atoms and Molecules . . . . .	18
2.4.1 The OPLS-AA Force Field . . . . .	18
2.4.2 Periodic Boundary Conditions, Minimum Image Convention, and Ewald Summation . . . . .	20

<b>3</b>	<b>Setup, Equilibration, and Final Sampling of the Systems</b>	<b>23</b>
3.1	Overview . . . . .	23
3.2	The Model Systems . . . . .	24
3.2.1	The Montmorillonite Model . . . . .	24
3.2.2	The Muscovite Model . . . . .	26
3.2.3	The $C_nTMA^+$ Model . . . . .	29
3.2.4	The Water Model . . . . .	31
3.2.5	The Simulation Cells . . . . .	32
3.3	Equilibration of the Systems . . . . .	35
3.4	Final Sampling . . . . .	39
<b>4</b>	<b>Aggregation of <math>C_nTMA^+</math> Ions at the Cleaved Muscovite–Water Interface</b>	<b>47</b>
4.1	Overview of Experimental Findings . . . . .	47
4.2	Adsorption Positions of the $C_nTMA^+$ Ions . . . . .	48
4.3	Positions of the Inorganic Ions . . . . .	56
4.4	Structure of the Water Film . . . . .	59
4.5	Structure and Thickness of the Adsorbed Aggregates . . . . .	63
4.6	Discussion on the Transferability of the Simulation Results to Real Systems . . . . .	68
4.7	Summary of the Simulation Results . . . . .	70
<b>5</b>	<b>Aggregation of <math>C_nTMA^+</math> Ions at the External Surface of Montmorillonite</b>	<b>73</b>
5.1	Structure of the Water Film . . . . .	73
5.2	Adsorption Positions of the $C_nTMA^+$ Ions . . . . .	78
5.3	Amount of $C_nTMA^+$ Adsorbed on the External Surface of Montmorillonite . . . . .	83
5.4	Positions of the Inorganic Ions . . . . .	88
5.5	Structure and Thickness of the Adsorbed Aggregates . . . . .	92
5.6	Summary of the Simulation Results . . . . .	98
<b>6</b>	<b>Summary and Outlook</b>	<b>101</b>



<b>Bibliography</b>	<b>107</b>
<b>A Extended Figures</b>	<b>119</b>
<b>B Used Software</b>	<b>123</b>
<b>Curriculum Vitae</b>	<b>125</b>
<b>Scientific Publications and Presentations</b>	<b>127</b>
<b>Acknowledgements</b>	<b>129</b>



## List of Abbreviations

AFM	Atomic Force Microscope
$A_{uc}$	Area of a Unit Cell
BE <sup>+</sup>	Benzethonium (C <sub>27</sub> H <sub>42</sub> NO <sub>2</sub> <sup>+</sup> )
BMU	Bundesministerium für Umwelt, Naturschutz und Reaktorsicherheit (Federal Ministry for the Environment, Nature Conservation and Nuclear Safety)
C <sub>8</sub> TMA <sup>+</sup>	Octyltrimethylammonium (C <sub>11</sub> H <sub>26</sub> N <sup>+</sup> )
C <sub>12</sub> TMA <sup>+</sup>	Dodecyltrimethylammonium (C <sub>14</sub> H <sub>34</sub> N <sup>+</sup> )
C <sub>16</sub> TMA <sup>+</sup>	Hexadecyltrimethylammonium (C <sub>17</sub> H <sub>42</sub> N <sup>+</sup> )
CBMC	Configurational Bias Monte Carlo
CMC	Critical Micelle Concentration
C <sub>n</sub> TMA <sup>+</sup>	Alkyltrimethylammonium (C <sub>n+3</sub> H <sub>2n+10</sub> N <sup>+</sup> )
FTIR	Fourier Transform Infrared Spectroscopy
HDPy <sup>+</sup>	Hexadecylpyridinium (C <sub>21</sub> H <sub>38</sub> N <sup>+</sup> )
HLW	High Level Waste
IAEA	International Atomic Energy Agency
IfB	Institut für Bodenkunde (Institute of Soil Science)
IR	Infrared Spectroscopy
IRS	Institut für Radioökologie und Strahlenschutz (Institute of Radioecology and Radiation Protection)

x LIST OF ABBREVIATIONS

LILW	Low- and Intermediate-Level Waste
MC	Monte Carlo
MD	Molecular Dynamics
NEXAFS	Near Edge X-ray Absorption Fine Structure Spectroscopy
NMR	Nuclear Magnetic Resonance Spectroscopy
NR	Neutron Reflectometry
OPLS-AA	Optimized Potentials for Liquid Simulations - All Atom
RRZN	Central Services Information Technology (previously: Regionales Rechenzentrum für Niedersachsen)
SFA	Surface Force Apparatus
TIP4P	Transferable Intermolecular Potential Four Point
TPP <sup>+</sup>	Tetraphenylphosphonium (C <sub>24</sub> H <sub>20</sub> P <sup>+</sup> )
XPS	X-ray Photoelectron Spectroscopy
ZSR	Zentrum für Strahlenschutz und Radioökologie (Center for Radiation Protection and Radioecology)

# List of Figures

3.1	Illustrations of a Wyoming-type montmorillonite with the formula unit $\text{Na}_{0.375}(\text{Si}_{3.875}\text{Al}_{0.125})(\text{Al}_{1.625}\text{Fe}_{0.125}^{3+}\text{Mg}_{0.25})\text{O}_{10}(\text{OH})_2$ . . . . .	24
3.2	Illustrations of muscovite mica . . . . .	28
3.3	Illustration of a $\text{C}_{16}\text{TMA}^+$ cation . . . . .	29
3.4	Snapshot of the simulated equilibrium configuration for the bilayer arrangement at a coverage of $1.25 \text{C}_{12}\text{TMA}^+ / A_{\text{uc}}$ . . . . .	33
3.5	Schematic representations of monolayer and bilayer aggregates of organic cations assembled on mineral surfaces . . . . .	34
3.6	Convergence profile of the total potential energy for the bilayer arrangement at the muscovite surface at a coverage of $0.75 \text{C}_{16}\text{TMA}^+ / A_{\text{uc}}$ . . . . .	36
3.7	Vertical atomic density profiles for potassium and headgroup carbon atoms of $\text{C}_{16}\text{TMA}^+$ as functions of the distance $z$ from the muscovite surface for the bilayer arrangement at a coverage of $0.75 \text{C}_{16}\text{TMA}^+ / A_{\text{uc}}$ . . . . .	38
3.8	Vertical atomic density profiles for water oxygen as functions of the distance $z$ from the unmodified muscovite surface . . . . .	40
3.9	Vertical atomic density profiles for water hydrogen as functions of the distance $z$ from the unmodified muscovite surface . . . . .	41
3.10	Lateral atomic density profiles for water and potassium at the unmodified muscovite–water interface . . . . .	43
3.11	Vertical atomic density profiles for carbon and nitrogen of $\text{C}_{16}\text{TMA}^+$ , $\text{Na}^+$ and $\text{Cl}^-$ as functions of the distance $z$ from the montmorillonite surface for the bilayer arrangement at a coverage of $0.75 \text{C}_{16}\text{TMA}^+ / A_{\text{uc}}$ . . . . .	45
4.1	Vertical atomic density profiles for carbon atoms of $\text{C}_n\text{TMA}^+$ as functions of the distance $z$ from the muscovite surface . . . . .	49
4.2	Top view and side view of an inner-sphere and an outer-sphere surface complex of $\text{C}_{16}\text{TMA}^+$ on the muscovite surface . . . . .	50

xii List of Figures

4.3	Radial distribution functions of water oxygen around $C_{16}TMA^+$ headgroups for the bilayer arrangement at a coverage of $0.5 C_{16}TMA^+/A_{uc}$ . . . . .	51
4.4	Vertical atomic density profiles for water, $C_{16}TMA^+$ , potassium, and chloride as functions of the distance $z$ from the muscovite surface for the monolayer arrangement at a coverage of $1 C_{16}TMA^+/A_{uc}$ . . . . .	52
4.5	Lateral atomic density profiles for water, $C_{16}TMA^+$ headgroup carbon and potassium at the muscovite–water interface for the monolayer arrangement at a coverage of $1 C_{16}TMA^+/A_{uc}$ . . . . .	53
4.6	Cumulative contents of nitrogen atoms as functions of the distance $z$ from the muscovite surface for monolayer and bilayer arrangements at different $C_{16}TMA^+$ coverages . . . . .	55
4.7	Vertical atomic density profiles for potassium as functions of the distance $z$ from the muscovite surface . . . . .	57
4.8	Vertical atomic density profiles for chloride as functions of the distance $z$ from the muscovite surface . . . . .	58
4.9	Vertical atomic density profiles for water oxygen as functions of the distance $z$ from the muscovite surface for monolayer and bilayer arrangements at coverages of 0 and $1 C_{16}TMA^+/A_{uc}$ . . . . .	59
4.10	Water film thicknesses as functions of the $C_nTMA^+$ coverage . . . . .	60
4.11	Relation between the alkyl chain length $n$ and the volume $V$ displaced per $C_nTMA^+$ ion . . . . .	62
4.12	Snapshots of the simulated interfacial equilibrium structures in the regions $15 \text{ \AA} < z < 26 \text{ \AA}$ for the $C_{16}TMA^+$ bilayer arrangements at the coverages of 0.5 and $1.5 C_{16}TMA^+/A_{uc}$ . . . . .	63
4.13	Snapshots of the simulated equilibrium configurations for the $C_{16}TMA^+$ and $C_8TMA^+$ bilayer arrangements at coverages of $1.25 C_nTMA^+/A_{uc}$ . . . . .	65
4.14	Fractions of gauche conformations of the alkyl chains for monolayer and bilayer arrangements as functions of the $C_nTMA^+$ coverage . . . . .	67
5.1	Vertical atomic density profiles for water oxygen and hydrogen as functions of the distance $z$ from the montmorillonite surface . . . . .	74
5.2	Snapshots of $C_{16}TMA^+$ ions adsorbed as inner-sphere and outer-sphere complexes on the montmorillonite surface . . . . .	75
5.3	Lateral atomic density profiles for water and surface cations at the unmodified montmorillonite–water and muscovite–water interfaces . . . . .	76
5.4	Vertical atomic density profiles for carbon atoms of $C_nTMA^+$ as functions of the distance $z$ from the montmorillonite surface . . . . .	79

5.5	Vertical atomic density profiles for water, $C_{16}TMA^+$ , sodium, and chloride as functions of the distance $z$ from the montmorillonite surface for the bilayer arrangement at a coverage of $0.75 C_{16}TMA^+ / A_{uc}$ . . . . .	81
5.6	Radial distribution functions of basal oxygen atoms of the montmorillonite surface around $C_{16}TMA^+$ headgroup atoms for the monolayer arrangement at a coverage of $0.375 C_{16}TMA^+ / A_{uc}$ . . . . .	82
5.7	Lateral atomic density profiles for (a) water hydrogen and (b) $C_{12}TMA^+$ headgroup carbon, nitrogen, and $K^+$ at the montmorillonite–water interface for the monolayer arrangement at a coverage of $0.5 C_{12}TMA^+ / A_{uc}$ . . . . .	83
5.8	Cumulative contents of nitrogen atoms as functions of the distance $z$ from the montmorillonite surface for monolayer and bilayer arrangements at different $C_{16}TMA^+$ coverages . . . . .	84
5.9	Amounts of $C_nTMA^+$ adsorbed on the montmorillonite surface for monolayer and bilayer arrangements as functions of the $C_nTMA^+$ coverage . . . . .	86
5.10	Number of molecules in the first water layer adsorbed on the montmorillonite surface as a function of the number of $C_nTMA^+$ inner-sphere surface complexes. . . . .	88
5.11	Vertical atomic density profiles for sodium as functions of the distance $z$ from the montmorillonite surface . . . . .	90
5.12	Vertical atomic density profiles for chloride as functions of the distance $z$ from the montmorillonite surface . . . . .	91
5.13	Snapshots of the simulated equilibrium configurations for the monolayer arrangement at a coverage of $1 C_{16}TMA^+ / A_{uc}$ and the bilayer arrangement at a coverage of $1.5 C_{16}TMA^+ / A_{uc}$ . . . . .	93
5.14	Snapshots of the simulated equilibrium configurations for the monolayer arrangement at a coverage of $1 C_8TMA^+ / A_{uc}$ and the bilayer arrangement at a coverage of $1.5 C_8TMA^+ / A_{uc}$ . . . . .	94
5.15	Fractions of gauche conformations of the alkyl chains for monolayer and bilayer arrangements as functions of the $C_nTMA^+$ coverage . . . . .	96
A.1	Side view and top view of a $C_8TMA^+$ ion adsorbed parallel to the montmorillonite surface . . . . .	119
A.2	Vertical atomic density profiles for $C_nTMA^+$ nitrogen, aliphatic carbon, water oxygen, and water hydrogen atoms as functions of the distance $z$ from the muscovite surface for the bilayer arrangement at a coverage of $0.75 C_{16}TMA^+ / A_{uc}$ . . . . .	120





## List of Tables

3.1	Partial atomic charges $q(e)$ for the montmorillonite and the muscovite layers as used in the simulations . . . . .	26
3.2	Partial atomic charges for $C_nTMA^+$ computed by means of the Mulliken population analysis . . . . .	30
3.3	Overview of the simulated mineral-water-organic systems . . . . .	35
3.4	Average water oxygen density in the vertical region of $10 \text{ \AA} \leq z \leq 35 \text{ \AA}$ of the muscovite-water reference system . . . . .	42
4.1	Calculated volumes displaced per $C_nTMACl$ , methyl(ene) or headgroup	61
B.1	Software employed for the calculations of this work. . . . .	123
B.2	Software employed for the creation of figures and typesetting. . . . .	123



---

# Introduction

## 1.1 Background and Motivation

This work was carried out from May 2008 until December 2011 at the *Institute of Radioecology and Radiation Protection* (IRS, until April 2010 *Center for Radiation Protection and Radioecology* (ZSR)) of the Gottfried Wilhelm Leibniz Universität Hannover. In the last two decades, the IRS has actively contributed to scientific research in the context of radioactive waste disposal with the study of organically modified clays (organoclays). Significant parts of the experimental studies were carried out in close collaboration with the *Institute of Soil Science* (IfB).

On the international stage, clays are considered as materials suitable for the application in engineered barrier systems of final radioactive waste repositories [1]. Their properties of swelling in the presence of water, their plasticity and ability to adsorb cationic pollutants are of great interest in the context of the safe disposal of radioactive waste [2]. However, clay minerals exhibit almost no retention capacity for anions. This is of concern because several dose-relevant radionuclides like  $^{129}\text{I}$ ,  $^{79}\text{Se}$ , and  $^{36}\text{Cl}$  predominantly exist in anionic form in aqueous solution [3].

During the production of organoclays, the inorganic cations in the interlayer spaces and on the external surfaces of clay particles are exchanged by certain organic cations, for example quaternary alkylammonium ions. Compared to naturally occurring clays, the adsorption capacity of organoclays for anionic radionuclides is

substantially higher [4–8]. Their possible application as part of engineered barriers has been in the focus of research at the IRS. Different organoclays were examined with respect to their anion and cation adsorption capacities and their selectivity for different anions [4, 6, 7, 9–14]. Furthermore, the impact of organic modification on the microstructure and the mechanical properties of clays was investigated [5, 8, 15, 16]. Regarding their long-term stability under repository-relevant conditions, the influence of external parameters as increased temperatures or ionizing radiation on the properties of organoclays has been investigated [8, 17–21].

In the last years, the experimental research at the institute was complemented by theoretical computer simulation studies [22–37]. Revealing the structure of the organoclays on a molecular scale, the simulation studies carried out by means of classical *Monte Carlo* (MC) simulations have successfully contributed to the explanation of experimental observations as, e. g., the increase of basal plane spacings or the changes of surface wetting properties and surface charges. Among others, in the simulation studies that preceded this work, the adsorption of *hexadecylpyridinium* cations ( $\text{HDPy}^+ = \text{C}_{21}\text{H}_{38}\text{N}^+$ ) on the basal surfaces of montmorillonite and muscovite and the structure of the surface aggregates formed in aqueous solution were investigated [28, 29]. In this work, the theoretical study of the aggregation of alkylammonium cations on the basal surfaces of montmorillonite and muscovite is continued.

## 1.2 Aspects of Radioactive Waste Disposal

### 1.2.1 Disposal in Deep Geological Formations

The vast bulk of the radioactive waste produced in Germany results from the operation or decommissioning of nuclear power plants and research reactors, from the reprocessing of spent nuclear fuel, and from the application of radioactive material in medicine, industry, research, and development [3]. In Germany, this waste is divided into two categories, namely *heat-generating radioactive waste* and *radioactive waste with negligible heat generation* [38]. This classification is based on the fact that

radioactive decay is accompanied by the release of heat, the magnitude of which is mainly determined by the level of activity concentration. The predicted volume of radioactive waste with negligible heat generation produced in Germany amounts to approximately 300 000 m<sup>3</sup>, whereas the predicted volume of heat-generating radioactive waste amounts to only approximately 22 000 m<sup>3</sup>. However, this small volume of heat-generating radioactive waste corresponds approximately 99.9 % of the activity of all radioactive waste in Germany [3]. Heat-generating radioactive waste mainly consists of spent fuel elements and vitrified waste block containers from the reprocessing of spent fuel elements, which was permitted in Germany until 2005. Furthermore, it contains compacted fuel cladding and structural parts from the reprocessing of fuel elements [3, 38].

On the international stage, slightly different waste classification systems are used. For instance, according to the guideline of the *International Atomic Energy Agency* (IAEA) for the classification of radioactive waste, the waste is divided into three categories based on activity as a measure. The guideline distinguishes between *high-level waste* (HLW), *low- and intermediate-level waste* (LILW) and exempt waste, which is waste that exhibits negligible activity and can thus be treated as conventional waste [39].

According to § 9a of the German *Atomic Energy Act* (Atomgesetz), it is the duty of the Federal Republic of Germany to “establish installations for the safekeeping and disposal of radioactive waste” [40, 41]. In September 2010, the German *Federal Ministry for the Environment, Nature Conservation and Nuclear Safety* (BMU) published the *Safety Requirements Governing the Final Disposal of Heat-Generating Radioactive Waste* [38, 42]. These safety requirements shall serve as a standard for the evaluation of potential final repository sites and designs. In agreement with international concepts of radioactive waste disposal [1], Germany decided that after a period of interim storage to reduce the decay heat to a manageable level, heat-generating radioactive waste shall be disposed in deep geological formations several hundreds of meters underground within the borders of the country [38]. The concept of the disposal of radioactive waste in deep geological formations builds up on the

combined safety functions of different natural and technical components of the repository system and is therefore termed a *multi barrier concept*.

In German concepts, three types of barriers, namely technical, geotechnical and geological barriers are distinguished [38, 43]. The waste matrix and the surrounding waste containers represent the *technical barrier*, which is supposed to retain the radionuclides and to delay their release. The *geotechnical barrier* consists of buffer material between the waste containers and the host rock and of the material used for the backfilling of hollow spaces and the sealing of the connecting galleries. It is supposed to retard the migration of radionuclides in the direction of the biosphere after corrosion induced leakage of the waste containers. Moreover, it protects the waste containers from external mechanical stress caused, e. g., by shifts in the host rock formation and from the inflow of water. On the international stage, the technical and the geotechnical barrier are commonly subsumed under the term *engineered barrier system* [1]. The *geological barrier* consists of the host rock formation and its geological surroundings. It is intended to limit the influx of water and to delay the transport of radionuclides to the biosphere. Among others, rock clay (for example in Belgium, France, Switzerland, and Hungary), rock salt (for example in Germany) and granite (for example in Sweden, Finland, and Japan) are considered as candidates for host rock formations [2].

A final radioactive waste repository shall concentrate the waste and isolate it from the biosphere for as long as possible to protect people and the environment from ionizing radiation and other harmful effects caused by the waste [38]. To ensure the isolation of the waste, the final repository has to be protected against both external natural influences as , e. g., floodings or earthquakes and unintentional or unauthorized human access to guarantee, for example, non-proliferation [3]. Furthermore, from an ethical point of view, the final repository shall be designed in such a way that future generations are not confronted with disproportional burdens or obligations resulting from the waste disposal site [38]. Therefore, in the post-closure phase of a waste disposal, interventions as surveillance, maintenance or repair and administrative measures as usage restrictions must not be required.

However, during the operation phase of the final repository, both passive and active safety precautions are envisaged, and the retrieval of the waste containers must be rendered possible [3, 38]. In the first 500 years of the post-closure phase, the recovery of the waste containers from the sealed final repository shall be feasible [38]. To ensure the long-term safety of a final repository for heat-generating radioactive waste in Germany, a site-specific safety analysis covering a period of one million years is to be carried out [38]. Among others, it is to be proven that “any release of radioactive substances from the final repository only negligibly increases the risks associated with natural radiation exposure.” [38, 42]. However, at the time of writing this thesis, effective dose limits for individuals resulting from this claim were still under discussion [38, 43, 44].

### **1.2.2 Potential Application of Organically Modified Clays as Part of Geotechnical Barriers**

In various international concepts of radioactive waste disposal, bentonite is considered as a material suitable for backfilling and for the construction of engineered barriers [1, 18]. Montmorillonite clay is the main component of bentonite (75 wt% of Wyoming bentonite). Other components of Wyoming bentonite are quartz (15 wt%) and feldspars (5 wt% to 8 wt%) [45]. Montmorillonite swells in the presence of water, exhibits high plasticity, and shows an excellent adsorption capacity for cations [45]. These properties are advantageous with respect to its possible application in geotechnical barriers: Due to their self-sealing property, bentonite barriers can compensate geophysical disturbances and reduce the inflow of water. Furthermore, they avert the advective transport of solute radionuclides and the corrosion of waste canisters. The diameters of clay particles are in the dimension of 1  $\mu\text{m}$  [46]. Each clay particle consists of some tens of negatively charged silicate layers, which are held together by charge balancing inorganic cations [46] (see subsection 3.2.1). This layered structure explains the swelling behavior of clays: The variable layer spacing is caused by the affinity of the clay cations for water leading to the intercalation of

water molecules in the interlayer spaces [47]. Cationic radionuclides are adsorbed by clay particles through their exchange with interlayer or surface clay cations.

Unfortunately, naturally occurring clay minerals exhibit almost no retention capacities for anions. This is of concern because several radionuclides that are of relevance for the long-term safety of final repositories for heat-generating radioactive waste mainly exist in anionic forms in aqueous solution. These are, for example,  $^{129}\text{I}$ ,  $^{79}\text{Se}$ ,<sup>1</sup> and  $^{36}\text{Cl}$  with long half-lives of  $1.6 \times 10^7$  a,  $\sim 3 \times 10^5$  a, and  $3.0 \times 10^5$  a, respectively [3, 37, 48, 49]. Furthermore, they show high solubility and mobility in aqueous solutions [3]. Model studies of the long-term safety of radioactive waste repositories in the post-closure phase for an Opalinus clay host rock scenario and a salt host rock scenario have shown that, in these cases, the radiation doses are dominated by the anionic radionuclides  $^{129}\text{I}$  [50] and  $^{79}\text{Se}$  [3], respectively.

Clay cations can be exchanged not only with inorganic, but also with organic cations that intercalate in the interlayer spaces and form organic aggregates on the external surfaces of the clay particles. This exchange property is exploited in the production of organoclays, whose adsorption capacity for anionic radionuclides is increased substantially as compared to naturally occurring clays [4–8]. In the context of their possible application in engineered barriers, different bentonite additives have been investigated with respect to their potential of artificially increasing the anion adsorption capacities of clays, and organoclays have turned out to be promising candidates [51].

Clays adsorb organic cations not only through cation exchange but also through hydrophobic bonding of the organic cations and the uptake of the organic cations as ion pairs together with their inorganic counterions. The retention of anionic radionuclides by organoclays can thus be supposed to occur by the exchange with previously adsorbed counterions [17, 52, 53]. Even though slightly decreased, organoclays possess adsorption capacities for cations. This is because during the production of organoclays, not all inorganic clay cations are exchanged by organic ones [12, 17].

---

<sup>1</sup>The exact determination of the half-life of  $^{79}\text{Se}$  has been an ongoing subject of research. Newest estimates are in the range of  $3.0 \times 10^5$  a [37, 48, 49].



Due to the adsorption of organic cations on the external surfaces of clay particles, the hydrophobicity of the organoclays is increased, and they are capable of adsorbing nonpolar organic substances [54–56]. These adsorption properties render organoclays valuable for their application in industrial and environmental engineering processes. They are used as adsorbents to remove ionic and organic pollutants – e. g. herbicides, fats, or solvents – from soil, groundwater or waste water [54–56] or serve as additives in the production of paints or cosmetics [54].

To be applicable as part of engineered barriers, organoclays are required to keep their adsorption capacities over long time scales under repository-relevant conditions. The adsorption behavior of different organoclays modified with HDPy<sup>+</sup>, *hexadecyltrimethylammonium* (C<sub>16</sub>TMA<sup>+</sup> = C<sub>17</sub>H<sub>42</sub>N<sup>+</sup>), *benzethonium* (BE<sup>+</sup> = C<sub>27</sub>H<sub>42</sub>NO<sub>2</sub><sup>+</sup>), and *tetraphenylphosphonium* (TPP<sup>+</sup> = C<sub>24</sub>H<sub>20</sub>P<sup>+</sup>) has been investigated under varying conditions at the IRS in close collaboration with the IfB. The different organoclays were examined with respect to their anion and cation adsorption capacities and their selectivity for different anions [4, 6, 7, 9–14]. The impact of organic modification on the micro structure and the mechanical properties of clays as, e. g., the increase of basal spacings and the changes of particle shape, surface charge, wettability and diffusion properties have been studied [5, 8, 15, 16]. Moreover, the impact of external factors like increased temperatures [17–20] or ionizing radiation [21] on the stability of the organoclays and the retention of their adsorption capacities, have been studied.

In general, the adsorption capacity of organoclays for anions turned out to be dependent on the type and the amounts of cations used for the modification. Clays modified with HDPy<sup>+</sup>, C<sub>16</sub>TMA<sup>+</sup>, and BE<sup>+</sup> exhibit considerably higher exchange capacities for anions than clays modified with TPP<sup>+</sup>. On the other hand, TPP<sup>+</sup> modified clays show a much higher thermal stability of their anion adsorption capacities [8, 20]. Of all candidates that were investigated, C<sub>16</sub>TMA<sup>+</sup> modified bentonite proved to be the most promising one for the application in engineered barriers because of its comparatively high anion exchange capacity and thermal stability [8].

### 1.3 Application of Classical Molecular Simulations in Clay Research

The idea of using naturally occurring and organically modified clays as part of engineered barriers of radioactive waste repositories has not only motivated experimental work but also various theoretical studies. Classical molecular simulation methods provide insight into the structures of (organically modified) clay minerals on a molecular scale, which are currently not yet accessible to experimental methods.

However, the molecular simulation of mineral-water(-organics) systems is computationally very expensive. Therefore, the size of model systems is generally limited to the size range of several nanometers, which is significantly smaller than the spatial extension of a single clay particle of approximately 1  $\mu\text{m}$ . In most cases, simulation studies are thus limited to the investigation of the properties of either interlayer spaces, basal or lateral surfaces of clay particles. With the aid of super computers that can execute massively parallel codes under the acceptance of extremely long computation times of several ten thousands of CPU hours, the simulation of systems with extensions in the micrometer range was shown to be manageable [57].

Despite these limitations, molecular simulations have substantially contributed to the understanding of the swelling behavior of clays [47, 58, 59], the diffusion of water and inorganic ions in the interlayer spaces [60, 61], the expansion of interlayer spaces due to the intercalation of organic cations, and the arrangement and conformational order of intercalated organic molecules [62–65]. The structures of ultrathin water films adsorbed on the external surfaces of the mineral particles have been deciphered [66–69] and the adsorption positions of various inorganic and organic cations in dehydrated and hydrated states have been identified [67, 69–72]. The approach of complementing the experimental studies of mineral-water-organics systems with numerical analyses featuring classical MC simulations has been established during the past years at the IRS in collaboration with the IfB [8, 16, 22–37].

## 1.4 Aim and Structure of the Thesis

The aim of this thesis is a molecular-scale characterization of the structures of alkyltrimethylammonium ( $C_n\text{TMA}^+ = (\text{CH}_3)_3\text{N}(\text{CH}_2)_{n-1}\text{CH}_3^+$ ,  $n \in \{8, 12, 16\}$ ) surfactant aggregates formed on the external basal surfaces of montmorillonite and muscovite in aqueous solution. Such a characterization is a prerequisite for understanding the high adsorption capacities of organoclays for inorganic anions, cations, and organic compounds, which make them valuable for their use in various environmental technical applications.

In the case of montmorillonite, however, an experimental characterization currently appears to be nearly impossible because of the prohibitively small size of its particles (typically below 1  $\mu\text{m}$ ), their low crystallinity and their property of swelling in the presence of water. On the contrary, classical molecular simulations represent a powerful tool for the exploration of mineral structures on a molecular scale. In this work, the Monte Carlo method, which has proved to be particularly appropriate for studying organoclays, will be applied to conduct an extensive computational study of the montmorillonite-alkyltrimethylammonium-water system.

Owing to the scarcity of available experimental data for montmorillonite, which is required to test the simulation output against, an accompanying computational study of the muscovite-alkyltrimethylammonium-water system will be conducted. Both muscovite and montmorillonite belong to the group of dioctahedral phyllosilicates, and their basal surfaces exhibit substantial structural similarities. Differently from montmorillonite, however, muscovite particles can have comparatively large extensions with diameters of several  $\text{cm}^2$ . They show a high crystallinity, do not swell in the presence of water, and can be cleaved along their planes of interlayer cations to produce atomically smooth surfaces. These properties of muscovite have allowed the determination of structural parameters in previous experiments as, e. g., the thicknesses of surfactant aggregates assembled on the cleaved surface. By comparing these measured values to the simulated ones, the computational model can be tested for the validity of its results.

In this thesis, the impact of the  $C_n\text{TMA}^+$  surface coverage and the alkyl chain length  $n$  on the structures of the interfacial surfactant aggregates will be examined. Additionally, the comparison of the simulation results for montmorillonite with those for muscovite, which exhibits an approximately 2.7-fold higher layer charge density of its mineral layers, allows to evaluate the influence of the surface charge density on the structures of the assembled  $C_n\text{TMA}^+$  aggregates and the interfacial water films.

This thesis consists of six chapters. In chapter 2, which follows this introduction, a brief overview of the theoretical methods that are important within the scope of this work is given. The key concepts of the applied Monte Carlo algorithms are presented. Furthermore, the OPLS-AA Force Field, which was employed to model the interactions between atoms and molecules and the application of periodic boundary conditions are discussed. In chapter 3, the model systems, which the Monte Carlo simulations of this work are based upon, are described in detail. In this context, the process of system equilibration and the sampling of structural properties for the calculation of system averages are explained. Finally, an optimization of the sampling process is proposed, which allows a significant reduction of the statistical uncertainties of the calculated structural properties.

In the chapters 4<sup>2</sup> and 5, the results of the performed Monte Carlo studies of the adsorption and aggregation of alkyltrimethylammonium surfactant ions on the basal surfaces of muscovite and montmorillonite are presented. A discussion of the adsorption positions of the  $C_n\text{TMA}^+$  ions, the vertical and lateral structures of the assembled surfactant aggregates, and the changes of the interfacial water films induced by the organic modification of the mineral surfaces is given. The thesis concludes with chapter 6, in which the main results of this work are summarized.

---

<sup>2</sup>Reproduced in part with permission from B. Klebow and A. Meleshyn. Aggregation of Alkyl-trimethylammonium Ions at the Cleaved Muscovite Mica–Water Interface: A Monte Carlo Study. *Langmuir*, 27: 12968-12976, 2011. Copyright 2011 American Chemical Society.

---

## Theoretical Methods

### 2.1 Overview

In this chapter, a brief overview of the theoretical methods employed in the context of this thesis is given. All MC simulations of this work were carried out with the code *mclay*, which was developed by Meleshyn at the IRS [22] and has been successfully applied in various computational studies of clay-water(-organics) systems [22–35]. The *Fortran 95* code renders it possible to model the molecular arrangement of water and (in)organic ions in the interlayer spaces and on the external basal surfaces of clay minerals in  $NpT$  and  $NVT$  ensembles. It implements the Metropolis MC algorithm [73], which enables the translation of movable particles and the rotation of water molecules, as well as the configurational-bias MC algorithm [74], which enables conformational changes of flexible molecules.

In the sections 2.2 and 2.3, the essential ideas of the implemented MC algorithms are presented. In section 2.4, the *Optimized Potentials for Liquid Simulations - All Atom* (OPLS-AA) force field, which was used for the calculation of the potential interaction energies between atoms and molecules, and the application of *periodic boundary conditions* are described.

## 2.2 Classical Molecular Simulations

The clay-water-organics systems studied in this work consist of approximately 1700 to 2800 atoms. Simulating systems of this size by means of *ab initio* methods still clearly exceeds computational feasibility [75]. On the contrary, classical molecular simulations are much less computationally demanding and allow the calculation of equilibrium properties of classical many-body systems consisting of several thousands of atoms [76]. To represent the interactions between atoms and molecules, classical molecular simulations take advantage of empirical force fields incorporating classical potential energy functions for intra- and intermolecular interactions. This classical approach implies that, in contrast to *ab initio* methods, any effects depending on the electronic structure of the system, which cannot be covered by suitable parametrization procedures, are excluded from the calculations [37]. In general, two alternatives are available, namely the *Monte Carlo* (MC) and the *molecular dynamics* (MD) methods.

In a MD simulation, the time evolution of a model system is calculated by solving the classical equations of motion [75–77]. As an analytic solution is computationally not feasible, the equations are integrated numerically. After each time step  $\Delta t$ , the new coordinates of the particles and the forces on all particles are calculated. The simulation is continued until the equilibrium state is reached. Time-dependent system properties of interest are derived from the trajectories of the particles. Thermodynamic averages are calculated by averaging the instantaneous values recorded at each time step. Unfortunately, MD simulations are computationally very expensive. The simulation of clay systems having sizes comparable to those studied in this work is limited to time spans that are several magnitudes of order smaller than one second [75, 76].

On the contrary, MC algorithms follow a different approach: During a MC simulation, a phase space trajectory of a model system based on a chosen statistical ensemble is generated [75, 77]. Of course, the sampling of all states in configuration space is computationally not feasible. The Metropolis MC algorithm follows the idea

of importance sampling: Starting from an initial state, a random walk is performed in such a way that the number of times each state is visited is proportional to the probability that the system occupies that state in thermal equilibrium. Accordingly, after a sufficiently long equilibration run starting from an arbitrary initial state of the system,<sup>1</sup> only those states that exhibit a non-negligible probability density are considered for the sampling. When the system has attained the equilibrium state, thermodynamic properties and structural parameters as, e. g., particle distribution functions can be calculated.

The Metropolis MC scheme allows nonphysical moves of atoms and molecules during the equilibration. This leads to a significant speed up of the equilibration as compared to MD simulations. However, as MC algorithms do not reproduce the natural dynamics of model systems, the calculation of time-dependent properties such as diffusion coefficients is inhibited. In experiments of surfactant aggregation on mineral surfaces, the equilibration of aggregate structures was observed to take time spans reaching from seconds to up to several months depending on the conditions of the studied systems [53, 78, 79]. These time spans clearly exceed those that can be covered by MD simulations. For this reason, all simulations of this study were carried out by means of the MC method.

## 2.3 Monte Carlo Algorithms

### 2.3.1 Metropolis Monte Carlo

The MC method was given its name because of the extensive use of random numbers for the calculations. The Metropolis MC algorithm was originally developed by Metropolis and Ulam for the study of the diffusion of neutrons in fissionable material [73, 80–82].

---

<sup>1</sup>In an ideal MC simulation, which does not erroneously converge to a local energy minimum, the sampled equilibrium properties are independent of the chosen start coordinates.

To initialize a thermodynamic system, start coordinates are given to all particles. The state of the system is changed performing translational and rotational trial moves of the system particles according to the following scheme [22, 73, 75]:

1. Calculate the total potential energy  $E_o$  of the system.
2. Randomly chose one particle.
3. Change the coordinates of that particle by an arbitrary translation  $\delta\mathbf{r}$  or rotation  $\delta\Theta$ .<sup>2</sup>
4. Calculate the new potential energy  $E_n$  of the system.
5. Accept or reject the trial move obeying the Metropolis importance sampling rule.<sup>3</sup>
6. Repeat the steps 1 to 5 until the system has satisfactorily reached the equilibrium.
7. Calculate the averages of the desired properties as, e. g., the average potential energy of the system, interaction energies or distributions of particles.

The acceptance rule to decide whether a trial move is accepted or rejected has to be designed in such a way that the equilibrium distribution of the particles is not destroyed by the MC moves. Accordingly, for a system in equilibrium, for each state  $o$ , the averaged number of accepted trial moves leading away from the state  $o$  to another state  $n$  must equal the averaged number of accepted trial moves leading from other states  $n$  to the state  $o$ :

$$P(o) \sum_n [\alpha(o \rightarrow n) \text{acc}(o \rightarrow n)] = \sum_n [P(n) \alpha(n \rightarrow o) \text{acc}(n \rightarrow o)], \quad (2.1)$$

---

<sup>2</sup>The trial of translation or rotation of the chosen particle is limited by fixed values  $r_{\max}$  and  $\Theta_{\max}$ , respectively. The actual trial displacement  $\delta\mathbf{r}$  or trial rotation  $\delta\Theta$  is chosen from a Gaussian distribution with a variance of  $r_{\max}$  or  $\Theta_{\max}$ , respectively. The choice of  $r_{\max}$  and  $\Theta_{\max}$  affects the equilibration speed of the simulations, which is decreased by both too big and too small values: Too small values imply that a great deal of MC moves is needed for the equilibration of the system, whereas too big values imply the rejection of most trial moves. As a rule of thumb,  $r_{\max}$  and  $\Theta_{\max}$  should be chosen in such a way, that an acceptance ratio of 0.5 is yielded [75].

<sup>3</sup>A valid rule for the *NVT* ensemble is presented in the next paragraphs.



with  $P(i)$  denoting the probability that the system is in state  $i$ ,  $\alpha(i \rightarrow j)$  denoting the probability of attempting a trial move from state  $i$  to state  $j$  and  $\text{acc}(i \rightarrow j)$  denoting the probability of accepting the trial move from state  $i$  to state  $j$ . This condition of balance is necessary and sufficient for the validity of an importance sampling MC scheme [83].

The Metropolis importance sampling rule satisfies the much stronger condition of detailed balance, which is sufficient but not necessary for a valid algorithm. For each pair of states  $o, n$ , the averaged number of accepted trial moves leading from  $o$  to  $n$  must equal the averaged number of accepted trial moves leading from  $n$  to  $o$ :

$$P(o) \alpha(o \rightarrow n) \text{acc}(o \rightarrow n) = P(n) \alpha(n \rightarrow o) \text{acc}(n \rightarrow o). \quad (2.2)$$

Accordingly,

$$\frac{\text{acc}(o \rightarrow n)}{\text{acc}(n \rightarrow o)} = \frac{P(n) \alpha(n \rightarrow o)}{P(o) \alpha(o \rightarrow n)}. \quad (2.3)$$

In an  $NVT$  ensemble, the probability  $P(i)$  is proportional to the Boltzmann weight  $\exp(-\beta E_i)$  of the state with  $\beta = \frac{1}{k_B T}$ :

$$P(i) = C \exp(-\beta E_i). \quad (2.4)$$

As described above,  $\alpha$  is symmetric in the Metropolis MC sampling scheme:

$$\alpha(o \rightarrow n) = \alpha(n \rightarrow o), \quad (2.5)$$

and equation (2.3) leads to following condition:

$$\frac{\text{acc}(o \rightarrow n)}{\text{acc}(n \rightarrow o)} = \exp(-\beta(E_n - E_o)). \quad (2.6)$$

Among various other valid choices of  $\text{acc}(o \rightarrow n)$ , which mostly result in a less efficient sampling of configuration space [77], the Metropolis acceptance rule satisfies the condition equation (2.6) with

$$\text{acc}(o \rightarrow n) = \min[1, \exp(-\beta(E_n - E_o))]. \quad (2.7)$$

Accordingly, trial moves reducing the system energy are always accepted, whereas trial moves increasing the system energy are only accepted with the probability  $\exp(-\beta(E_n - E_o))$ .

### 2.3.2 Configurational Bias Monte Carlo

The *configurational bias Monte Carlo* (CBMC) algorithm renders it possible to simulate conformational changes of flexible molecules.<sup>4</sup> It is based on the Rosenbluth sampling scheme [84], after which flexible molecules are separated into  $N$  segments and regrown segment by segment. In the case of randomly directed insertion of long chain molecules, it is very likely that at least one of the segments overlaps with other molecules, which would lead to the rejection of the whole trial move. For instance, the probability that a trial insertion of a molecule of length  $N$  is free of hard-core overlaps scales as  $P \sim (1 - P_{\text{overlap}})^N$ . To increase the acceptance rate of conformational changes and avoid regions with high potential energies, the bonded segments are not added randomly but instead one after another in directions that preferably have large Boltzmann weights. In contrast to the Rosenbluth sampling scheme, the CBMC scheme obeys detailed balance [75]. As implemented in *mclay*, in one CBMC step, parts of a randomly chosen chain molecule are regrown segment by segment according to the following scheme [22, 74, 75]:

1. Randomly chose one molecule, which is to be regrown.
2. Randomly chose one segment  $i \in 1, \dots, N$ .
3. Randomly decide on forward or backward regrowth. In the case of forward regrowth, all segments  $< i$  remain at their positions and only segments with numbers  $\geq i$  are regrown. In the case of backward regrowth, only segments with numbers  $\leq i$  are regrown.<sup>5</sup>
4. Split the potential energy into a bonded part  $E^{\text{bonded}}$  comprising bond-bending and torsion energies and a non-bonded one  $E^{\text{non-bonded}}$  comprising Lennard-Jones and Coulomb interactions.<sup>6</sup>

---

<sup>4</sup>In this work,  $C_n\text{TMA}^+$  ions were the only flexible species (see section 3.2). The  $C_n\text{TMA}^+$  ions were separated into  $n + 3$  segments:  $n - 1$   $\text{CH}_2$  groups, three  $\text{CH}_3$  groups and one  $\text{NCH}_3$  group.

<sup>5</sup>To enhance readability, in the following lines, the CBMC algorithm is only explained for forward regrowth. The analogous procedure for backward regrowth is omitted.

<sup>6</sup>For further information on bonded and non-bonded interactions see section 2.4.

5. To regrow segment  $i$ , the following procedure is applied:

- a) Generate  $k_i$  trial positions  $\mathbf{b}_j$  to regrow segment  $i$ :<sup>7</sup>
  - i. Calculate a trial change  $\delta\theta_j$  of the bond angle  $\theta_i$  between the segments  $i - 2, i - 1$  and  $i$ .<sup>8</sup>
  - ii. Chose a trial position  $\mathbf{b}_j$  randomly upon a cone having its apex at the position of segment  $i - 1$ , the apex angle being  $\delta\theta_j$ , and the symmetry axis being described by the former bond between the segments  $i - 1$  and  $i$ .
  - iii. Calculate the torsional energy  $E_j^{\text{tors}}(\phi_j)$ , with  $\phi_j$  denoting the torsional angle defined by the positions of the segments  $i - 3, i - 2, i - 1$ , and  $\mathbf{b}_j$ .
  - iv. Accept the trial position  $\mathbf{b}_j$  with the probability  $\exp(-\beta E_j^{\text{tors}}(\phi_j))$ .
  - v. If  $\mathbf{b}_j$  is rejected, repeat the steps ii to iv until one position  $\mathbf{b}_j$  is accepted.
- b) Calculate the Boltzmann weight  $\exp(-\beta E^{\text{non-bonded}}(\mathbf{b}_j))$  for each trial position  $\mathbf{b}_j$ .  $E^{\text{non-bonded}}(\mathbf{b}_j)$  comprises all those interactions, which have not been taken into consideration for the calculation of the trial position  $\mathbf{b}_j$ , namely the sum of all non-bonded intramolecular interactions of  $\mathbf{b}_j$  with all segments  $< i$  and the intermolecular interactions of  $\mathbf{b}_j$  with all other particles of the system.
- c) Chose the new position  $\mathbf{b}_n$  among the  $k_i$  trial positions with probabilities  $P(\mathbf{b}_j)$  according to their Boltzmann weights:

$$P(\mathbf{b}_j) = \frac{\exp(-\beta E^{\text{non-bonded}}(\mathbf{b}_j))}{\sum_{l=1}^{k_i} \exp(-\beta E^{\text{non-bonded}}(\mathbf{b}_l))}. \quad (2.8)$$

<sup>7</sup>Both too small and too big values for  $k_i$  decrease the equilibration speed: If  $k_i$  is chosen too small, many regrow attempts will be refused. If  $k_i$  is chosen too big, the cost of each simulation cycle will be increased [75]. In this study,  $k_i$  was set to 10 for all the segments of  $C_n\text{TMA}^+$ .

<sup>8</sup>The change of  $\theta_i$  is limited by  $\theta_{\text{max}}$ .  $\delta\theta_j$  is chosen from a Gaussian distribution with a variance of  $\theta_{\text{max}}$ . As well as for  $r_{\text{max}}$  and  $\Theta_{\text{max}}$  in the case of the Metropolis MC scheme (see subsection 2.3.1), the choice of  $\theta_{\text{max}}$  affects the equilibration speed of the simulations.

6. Repeat the steps 2 to 5 for the remaining segments  $i + 1, \dots, N$  until the complete chain is regrown.
7. To obey detailed balance, correct for the bias introduced by the above-described non-random sampling:

Calculate the Rosenbluth weight  $W(n)$  [84] of the molecule in the new conformation:

$$W(n) = \prod_{i=1}^N w_i(n), \quad (2.9)$$

with  $w_i(n)$  denoting the contribution of each segment  $i$

$$w_i(n) = \frac{1}{k_i} \sum_{j=1}^{k_i} \exp(-\beta E^{\text{non-bonded}}(\mathbf{b}_j)). \quad (2.10)$$

8. Calculate the Rosenbluth weight [84] of the molecule in the old conformation. For this calculation perform the steps 5 to 7 with the difference that around each segment  $j$ , only  $k_j - 1$  trial positions are calculated and that the original position of segment  $j$  is taken as the trial position  $\mathbf{b}_{k_j}$ .
9. Accept the trial move with the probability

$$\text{acc}(o \rightarrow n) = \min(1, W(n)/W(o)), \quad (2.11)$$

the ratio of the Rosenbluth weights of the new and the old conformations.

## 2.4 Description of the Interactions Between Atoms and Molecules

### 2.4.1 The OPLS-AA Force Field

In this study, the interactions between mineral surfaces, organic cations, inorganic ions, and water molecules are described using the OPLS-AA force field [85]. The total potential energy of a model system is composed of pairwise non-bonded

inter- and intramolecular interaction energies  $E^{\text{non-bonded}}$  and bonded intramolecular interaction energies  $E^{\text{bonded}}$  between all atom pairs  $i, j$ :

$$E = \sum_i \sum_{j>i} E_{ij}^{\text{non-bonded}} + \sum_i \sum_{j>i} E_{ij}^{\text{bonded}}. \quad (2.12)$$

The non-bonded interaction energy between an atom pair  $i, j$  consists of Lennard-Jones and Coulomb interactions and is described by the following equation:

$$E_{ij}^{\text{non-bonded}}(r_{ij}) = a_{ij} \left( \frac{q_i q_j}{r_{ij}} + 4\epsilon_{ij} \left[ \left( \frac{\sigma_{ij}}{r_{ij}} \right)^{12} - \left( \frac{\sigma_{ij}}{r_{ij}} \right)^6 \right] \right), \quad (2.13)$$

with  $q_i$  and  $q_j$  denoting the (partial) charges of the atoms  $i$  and  $j$ .  $\sigma_{ij}$  and  $\epsilon_{ij}$  are empirical parameters that are derived by following combining rules from the OPLS-AA parameters  $\sigma_i$  and  $\epsilon_i$ :

$$\sigma_{ij} = \sqrt{\sigma_i \sigma_j}, \quad \epsilon_{ij} = \sqrt{\epsilon_i \epsilon_j}. \quad (2.14)$$

The scaling factor  $a_{ij}$  is introduced to ensure that intramolecular non-bonded interactions are counted only for atoms that are three or more bonds apart, and that interactions between atoms being exactly three bonds apart are scaled down by a factor of 0.5:

$$a_{ij} = \begin{cases} 0 & \text{for neighboring and next neighboring atoms} \\ 0.5 & \text{for atoms being three bonds apart} \\ 1 & \text{else} \end{cases}. \quad (2.15)$$

Intramolecular bonded energies are only calculated for flexible molecules and are composed of bond bending  $E^{\text{bend}}$  and torsion  $E^{\text{tors}}$  energies.<sup>9</sup> The total bonded potential energy of the system is calculated by summing  $E^{\text{bend}}$  over all bond angles  $\theta_i$  and  $E^{\text{tors}}$  over all dihedral angles  $\phi_i$ :

$$E^{\text{bonded}} = \sum_i E^{\text{bend}}(\theta_i) + \sum_i E^{\text{tors}}(\phi_i) \quad (2.16)$$

<sup>9</sup>The OPLS-AA force field additionally includes equations for bond stretching energies. For computational reasons (see section 3.1), all bond lengths were fixed during the simulations of this study. Bond stretching energies were therefore not calculated.

with

$$E^{\text{bend}}(\theta_i) = k_{\theta,i}(\theta_i - \theta_{0,i})^2 \quad (2.17)$$

and

$$E^{\text{tors}}(\phi_i) = \sum_{l=1}^3 V_{l,i} \left( 1 + (-1)^{l+1} \cos(l\phi_i) \right). \quad (2.18)$$

$\theta_{0,i}$  describes the bond angles of the flexible molecules in their energetically optimized conformations. The OPLS-AA parameters  $k_{\theta,i}$  and  $V_{l,i}$  depend on the types of the atoms constituting the accordant angles. Values for  $q_i$ ,  $q_j$ ,  $\sigma_i$ ,  $\epsilon_i$ ,  $\theta_{0,i}$ ,  $k_{\theta,i}$ , and  $V_{l,i}$  are available in the literature for various atom types in diverse molecular compositions [25, 85–91].

#### 2.4.2 Periodic Boundary Conditions, Minimum Image Convention, and Ewald Summation

In small systems, boundary effects have a large effect on the simulation results. For instance, in a simple cubic crystal consisting of 1 000 atoms, nearly 50 % are boundary atoms. In a crystal consisting of 1 000 000 atoms, still 6 % are boundary atoms. Accordingly, to model bulk behavior, which is negligibly influenced by boundary effects, the number of particles that has to be considered rapidly exceeds the limits of computational feasibility.

The application of periodic boundary conditions offers a solution for this problem: The simulation cell is replicated infinitely in all three dimensions such that the simulated system behaves like an infinite periodic system without any boundary atoms. If a particle leaves the simulation cell, an identical particle enters the cell on the opposite side [75, 77]. It has been shown that for clay–water systems, simulation cells with lateral dimensions of a few clay unit cells are sufficiently large to predict macroscopic properties as, e. g., structural parameters and density distributions without being affected by the artificial long-range periodicity [92]. Furthermore, in case of doubt, the impact of periodicity can be systematically investigated by changing the system size [76].

The application of periodic boundary conditions gives rise to an infinite number of atoms and molecules that have to be considered for the calculation of interaction energies: Each atom in the original simulation cell receives an infinite number of interaction partners. In practice, it is impossible to calculate this infinite series of pairwise interactions. Fortunately, the short-ranged Lennard-Jones interactions between particles that are apart farther than a certain *cut-off radius*  $r_c$  are negligibly weak. A value typical for molecular simulations is  $r_c = 9 \text{ \AA}$ , which was also chosen in this study.

In all simulations of this work, the extension of the simulation cell in all three dimensions exceeded twice the cut-off radius. In cases like this, the *minimum image convention* can be applied: The short-ranged interaction energy of each particle  $i$  with all other particles  $j$  that satisfy the condition  $r_{ij} \leq r_c$  can be calculated considering only the nearest images of every other particle  $j$  [76]. Interactions with far-away atoms do not have to be considered in detail because the summed interaction energy with these atoms converges to a constant value. The resulting small background potential is corrected as an integral for  $r > r_c$  assuming an isotropic distribution of all particles in that separation range [75, 77].

On the contrary, the sum of the long-ranged coulomb interactions does not converge and interactions between particles with distances  $r > r_c$  cannot be simply truncated. The *Ewald summation* method, which was originally developed in the study of ionic crystals [93] and takes advantage of the system periodicity, is used to solve that problem: Every point charge in the system is screened by a surrounding Gaussian charge distribution holding the same absolute charge as the point charge but the opposite sign. The resulting screened interactions are short-ranged and can be treated as described above. To maintain the system charge, a canceling charge distribution that is identical to the first Gaussian charge distribution but has the opposite sign is added and summed by means of Fourier transformation in reciprocal space [77, 93]. In this simulation study, a modification of the Ewald summation technique, which was optimized for systems with slab geometry by the addition of an according correction term, was applied [94].





---

## Setup, Equilibration, and Final Sampling of the Systems

### 3.1 Overview

In section 3.2 of this chapter, an overview of the model systems, which the MC simulations of this work are based upon, is given. The models describing the montmorillonite and the muscovite layers, the organic  $C_nTMA^+$  cations, and the water molecules are lined out in the subsections 3.2.1 to 3.2.4. The described mineral-water models in combination with various organic cations have been successfully applied in preceding MC studies at the IRS, and the simulation results have shown excellent agreement with experimental data [22, 25, 28, 29, 34, 35].

In subsection 3.2.5, the initial arrangements of atoms and molecules in the simulation cells are described in detail. The process of system equilibration is lined out in section 3.3, and criteria to estimate the number of MC cycles required for the equilibration of each system are derived. In section 3.4, the sampling of potential energies and structural properties for the calculation of system averages is explained. Finally, an optimization of the sampling process is proposed, which allows a significant reduction of the statistical uncertainties of the calculated structural properties.

## 3.2 The Model Systems

### 3.2.1 The Montmorillonite Model

Montmorillonite is a member of the phyllosilicate group. Each clay particle consists of some tens of negatively charged silicate layers, which are held together by charge balancing inorganic cations [46] (see figure 3.1(a)). Each of these silicate layers is composed of a sheet of octahedrally coordinated trivalent cations, mainly  $\text{Al}^{3+}$ , which is sandwiched by two sheets of tetrahedrally coordinated tetravalent cations, mainly  $\text{Si}^{4+}$ . One of the four oxygen atoms of each  $\text{SiO}_4$  tetrahedron bonds the tetrahedral sheets to the octahedral ones (see figure 3.1(a)). The remaining three *basal oxygen atoms* bridge the structural  $\text{Si}^{4+}$  ions (see figure 3.1(b)). Montmorillonite is a dioctahedral phyllosilicate. This means that only two of the three symmetrically independent octahedrally coordinated positions of the octahedral sheets are occupied by cations [95].

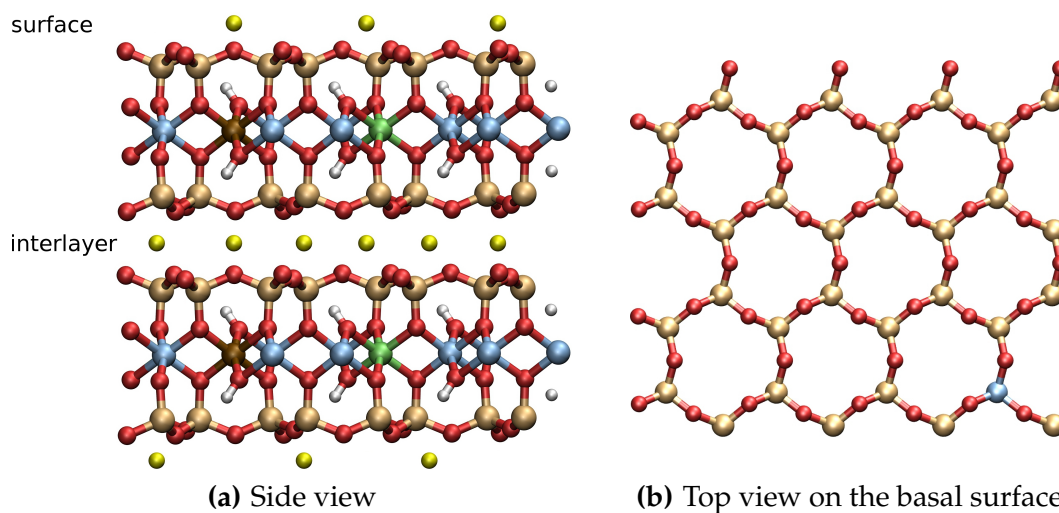


**Figure 3.1** – Illustrations of a Wyoming-type montmorillonite with the formula unit  $\text{Na}_{0.375}(\text{Si}_{3.875}\text{Al}_{0.125})(\text{Al}_{1.625}\text{Fe}_{0.125}^{3+}\text{Mg}_{0.25})\text{O}_{10}(\text{OH})_2$ . Ball and stick colors: beige (Si), light blue (Al), brown (Fe), green (Mg), red (O), white (H), yellow (Na).

Naturally occurring montmorillonites exhibit excess negative charges in both the octahedral and the tetrahedral sheets. These charges result from the exchange of structural  $\text{Al}^{3+}$  and  $\text{Si}^{4+}$  with ions of lower valence. In the octahedral sheets, some  $\text{Al}^{3+}$  are substituted by bivalent cations as, e. g.,  $\text{Mg}^{2+}$ . In the tetrahedral sheets, some  $\text{Si}^{4+}$  are substituted by trivalent cations as, e. g.,  $\text{Al}^{3+}$ . The resulting negative charge of the montmorillonite layers is compensated by interlayer and surface cations. The compositions of naturally occurring montmorillonites and the charge distributions within their layers vary in a broad range. Sodium and calcium are the most common interlayer cations of smectite clays [96]. The experimentally determined formula unit of Wyoming montmorillonite equals  $\text{Na}_{0.30}(\text{Si}_{3.96}\text{Al}_{0.04})(\text{Al}_{1.55}\text{Fe}_{0.20}^{3+}\text{Fe}_{0.01}^{2+}\text{Mg}_{0.24})\text{O}_{10}(\text{OH})_2$  [45].

The model of the Wyoming-type montmorillonite was adopted from Meleshyn [22, 28]. The lateral extension of the simulation cells used in this work was limited to the area of eight unit cells (cf. subsection 3.2.5). Accordingly, the formula unit was adjusted to  $\text{Na}_{0.375}(\text{Si}_{3.875}\text{Al}_{0.125})(\text{Al}_{1.625}\text{Fe}_{0.125}^{3+}\text{Mg}_{0.25})\text{O}_{10}(\text{OH})_2$ . This adjustment ensures that both octahedral and tetrahedral charges are accounted for in the montmorillonite model. The negative charge of the montmorillonite layers is compensated by sodium cations with coverages of 0.75 and 0.375  $\text{Na}^+$  per *unit cell area*<sup>1</sup> ( $A_{\text{uc}} = 46.36 \text{ \AA}^2$ ) in the interlayer spaces and on the external surfaces, respectively. Furthermore, to avoid the formation of dipoles, both tetrahedral sheets of the montmorillonite layer were given the same charge density of one charge substitution per simulation cell. The octahedral charge substitutions are distributed uniformly among the *cis-octahedral* positions.<sup>2</sup> The charges resulting from the substitutions were delocalized between the oxygen atoms surrounding the tetrahedral and octahedral charge substitutions by means of the method developed by Skipper et al. [92] for rigid clay minerals (see table 3.1).

<sup>1</sup>  $A_{\text{uc}}$  represents the area of the muscovite surface that corresponds to the area of one unit cell in the crystallographic *a-b* plane.

<sup>2</sup> In Wyoming montmorillonite, the octahedral charge substitutions are located only at *cis-octahedral* positions that possess two neighboring hydroxyl groups in contrast to *trans-octahedral* positions that possess two opposed hydroxyl groups.

**Table 3.1** – Partial atomic charges  $q(e)$  for the montmorillonite and the muscovite layers as used in the simulations according to Skipper et al. [92].

Atom type	$q(e)$	Description
Si	1.2	Silicon in the tetrahedral layer
Al_t	0.2	Aluminum in the tetrahedral layer
O_bas	-0.8	Surface oxygen in the tetrahedral layer
O_api	-1.0	Apical oxygen in the tetrahedral layer
Al_o	3.0	Aluminum in the octahedral layer
Fe_o	3.0	Iron ( $\text{Fe}^{3+}$ ) in the octahedral layer
Mg_o	2.0	Magnesium in the octahedral layer
O_OH	-1.52	Hydroxyl oxygen
H_OH	0.52	Hydroxyl hydrogen

According to experimental measurements by Müller-Vonmoos and Kahr [97], the dimensions of a unit cell of Wyoming montmorillonite equal  $a_0 = 5.1624 \text{ \AA}$ ,  $b_0 = 8.9796 \text{ \AA}$ ,  $\alpha = \angle(b, c) = 90^\circ$ ,  $\beta = \angle(a, c) = 99.5^\circ$ , and  $\gamma = \angle(a, b) = 90^\circ$ . The coordinates of the atoms within the mineral layer were determined following the algorithm to compute the atomic coordinates of phyllosilicates developed by Smoliar-Zviagina [98]. During the MC simulations, the montmorillonite layer was considered rigid, and consequently, only non-bonded Coulomb and Lennard-Jones interactions between montmorillonite, water, and cations had to be taken into account (see subsection 2.4.1). The OPLS-AA Lennard-Jones interaction parameters (see equation (2.13)) being crucial to carry out the MC simulations were taken from Jorgensen et al. [85, 86], Chandrasekhar et al. [87], and Aqvist [89].

### 3.2.2 The Muscovite Model

Up to now, it remains extremely difficult, or even impossible, to access the surface structure of montmorillonite particles on a molecular scale by means of experimental methods [99]. These difficulties result from the small size of the clay particles, their low crystallinity and their characteristic property of swelling in the presence of water.

The applied classical MC simulations provide insight into the system structures on a molecular scale, which are currently not yet accessible to experimental methods. Because of this low accessibility, however, only very few data is available to test the simulated  $C_n\text{TMA}^+$  aggregate structures and the underlying models on the basis of experimental measurements.

Unlike the external surface of montmorillonite, the cleaved surface of muscovite mica can easily be characterized by experimental methods. Muscovite particles can have comparatively large extensions with diameters of several  $\text{cm}^2$ . They show a high crystallinity, do not swell in the presence of water, and can be cleaved along their planes of interlayer cations to produce atomically smooth surfaces. In the past decades, many experimental studies have been carried out to determine the structures of surfactant aggregates assembled on the basal surface of muscovite (see section 4.1). Within this framework, structural parameters that are valuable for the testing of molecular model systems have been determined. These are for instance the thicknesses of the assembled  $C_n\text{TMA}^+$  aggregates, the conformational order of the alkyl chains within the aggregates, or the dependency of the observed aggregate structures on the surfactant concentration in the solution (see section 4.1).

Both montmorillonite and muscovite belong to the group of dioctahedral phyllosilicates, and the structures of their basal surfaces exhibit substantial similarities (cf. figures 3.1(b) and 3.2(b)). Hence, in this work, muscovite mica is considered as a reference system. This allows testing the model systems and the simulated aggregate structures on the basis of available experimental measurements (see sections 4.5 and 4.6, in which a detailed analyses of the simulated structures and a comparison with experimentally measured structural properties are given).

The formula unit of muscovite mica is  $\text{KAl}_2(\text{OH})_2(\text{AlSi}_3\text{O}_{10})$ . On average, every fourth silicon atom in the tetrahedral sheets is replaced by aluminum (see figure 3.2). In contrast to montmorillonite, muscovite holds no charge substitutions in the octahedral sheets. The total layer charge of muscovite is approximately 2.7 times higher than that of the studied Wyoming-type montmorillonite. The negative charge

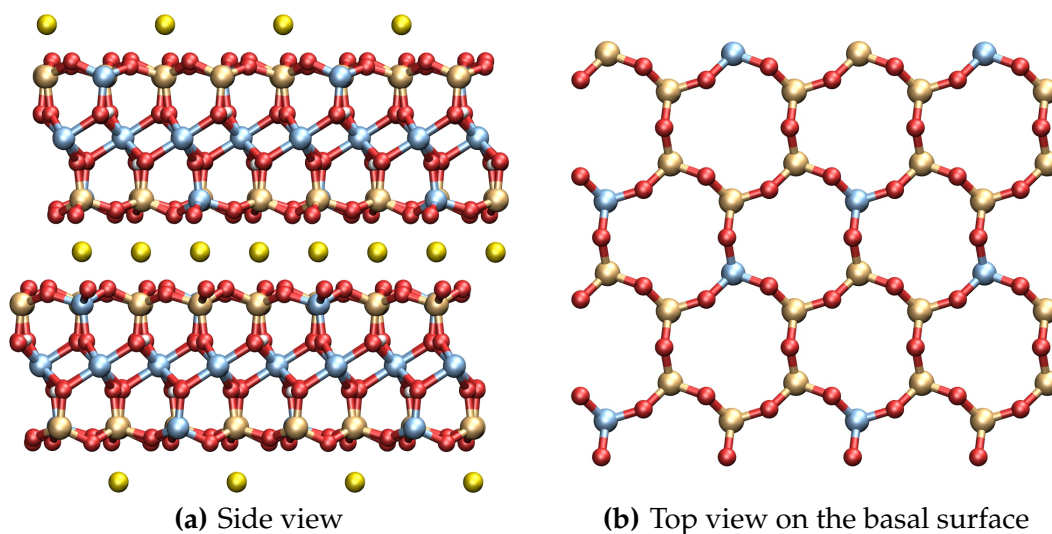


**Figure 3.2** – Illustrations of muscovite mica. Ball and stick colors: beige (Si), light blue (Al), red (O), white (H), yellow (K).

of the muscovite layers is compensated by potassium cations with coverages of one and two cations per unit cell area ( $A_{uc} = 46.72 \text{ \AA}^2$ ) on the external surfaces and in the interlayer spaces, respectively.

The muscovite model was adopted from Meleshyn [27]. The aluminum substitutions of the tetrahedral sheets were arranged according to Loewenstein’s rule of Al–O–Al avoidance [100]. The charges resulting from the tetrahedral substitutions were delocalized between the oxygen atoms of the mineral surface by means of the method developed by Skipper et al. [92] for rigid clay minerals (see table 3.1). According to an experimental study by Schlegel et al. [101], the dimensions of a unit cell of muscovite are  $a_0 = 5.1872 \text{ \AA}$ ,  $b_0 = 9.007 \text{ \AA}$ ,  $\alpha = \angle(b, c) = 90^\circ$ ,  $\beta = \angle(a, c) = 95.804^\circ$ , and  $\gamma = \angle(a, b) = 90^\circ$ . The coordinates of the atoms of the mineral layer were taken from the same study. The OPLS-AA Lennard-Jones interaction parameters, which were required to carry out the MC simulations (see equation (2.13)), were taken from Jorgensen et al. [85, 86], Chandrasekhar et al. [87], and Aqvist [89].

### 3.2.3 The $C_n\text{TMA}^+$ Model

The cationic alkyltrimethylammonium *surfactants*  $C_n\text{TMA}^+$  have a hydrophilic cationic headgroup  $\text{N}(\text{CH}_3)_3$  and a hydrophobic alkyl chain  $(\text{CH}_2)_{n-1}\text{CH}_3$  of length  $n$  (see figure 3.3). The expression surfactant stands for **surface active agent**. This notion emphasizes the fact that, owing to their molecular structure, surfactants assemble at and adsorb to interfaces and in this way change the characteristics of those. This behavior renders surfactants valuable for the application in many fields as, e. g., detergency, medicine or micellar catalysis.

The geometry of  $C_{16}\text{TMA}^+$  was taken from an X-ray diffractometry study of  $C_{16}\text{TMABr}$  in crystalline state by Campanelli and Scaramuzza [102]. As the geometry of  $C_{16}\text{TMABr}$  in crystalline state does not necessarily coincide with that of an isolated  $C_{16}\text{TMA}^+$  ion, this initial geometry was further optimized by means of quantum chemical energy optimizations [103]. These calculations were conducted with the GAMESS-US quantum chemistry software package [104, 105]. The B3LYP density functional [106–108] was employed as implemented in GAMESS-US, incorporating the correlation functional VWN I [109] and the SVP basis set [110].

The optimized bond angles were taken as parameters  $\theta_{0,i}$  for the calculation of the OPLS-AA bond bending potentials (see equation (2.17)). The partial charges within the  $C_{16}\text{TMA}^+$  ion (see table 3.2) required for the calculation of the Coulomb interactions during the MC simulations (see equation (2.13)) were computed by means of the Mulliken population analysis [103, 111–114]. For  $C_{12}\text{TMA}^+$  and  $C_8\text{TMA}^+$ ,



**Figure 3.3** – Illustration of a  $C_{16}\text{TMA}^+$  cation. Ball and stick colors: blue (N), brown (C), white (H).

**Table 3.2** – Partial atomic charges for  $C_nTMA^+$ ,  $n \in \{8, 12, 16\}$ , computed by means of the Mulliken population analysis.

	$C_{16}TMA^+$	$C_{12}TMA^+$	$C_8TMA^+$	
N	-0.36	-0.36	-0.36	Total partial charge of the headgroup: 0.65
C1 <sub>head</sub>	0.10	0.10	0.10	
H1.1 <sub>head</sub>	0.08	0.08	0.08	
H1.2 <sub>head</sub>	0.08	0.08	0.08	
H1.3 <sub>head</sub>	0.08	0.08	0.08	
C2 <sub>head</sub>	0.09	0.09	0.09	
H2.1 <sub>head</sub>	0.09	0.09	0.09	
H2.2 <sub>head</sub>	0.08	0.08	0.08	
H2.3 <sub>head</sub>	0.08	0.08	0.08	
C3 <sub>head</sub>	0.09	0.09	0.09	
H3.1 <sub>head</sub>	0.08	0.08	0.08	
H3.2 <sub>head</sub>	0.08	0.08	0.08	
H3.3 <sub>head</sub>	0.09	0.09	0.09	
C1	0.08	0.08	0.08	
H1.1	0.05	0.05	0.05	
H1.2	0.05	0.05	0.05	
C2	0.00	0.00	0.00	Total partial charge of the remaining alkyl chain: 0.16
H2.1	0.03	0.03	0.03	
H2.2	0.03	0.03	0.03	
C3	-0.02	-0.02	-0.02	
H3.1	0.01	0.01	0.02	
H3.2	0.01	0.01	0.02	
C4	0.02	0.02	0.02	
H4.1	0.00	0.00	0.00	
H4.2	0.00	0.00	0.00	
C5	0.02	0.02	0.01	
H5.1	0.00	0.00	0.00	
H5.2	0.00	0.00	0.00	
C6	0.02	0.02	0.00	
H6.1	-0.01	-0.01	0.00	
H6.2	-0.01	-0.01	0.00	
C7	0.02	0.02	-0.01	
H7.1	-0.01	-0.01	0.00	
H7.2	-0.01	-0.01	0.00	
C8	0.02	0.02	0.02	
H8.1	-0.01	-0.01	0.01	
H8.2	-0.01	-0.01	0.01	
C9 / H8.3	0.02	0.02	0.02	
H9.1	-0.01	-0.01		
H9.2	-0.01	-0.01		
C10	0.02	0.00		
H10.1	-0.01	-0.01		
H10.2	-0.01	-0.01		
C11	0.02	-0.01		
H11.1	-0.01	0.00		
H11.2	-0.01	0.00		
C12	0.02	0.02		
H12.1	-0.01	0.01		
H12.2	-0.01	0.01		
C13 / H12.3	0.02	0.01		
H13.1	-0.01			
H13.2	-0.01			
C14	0.00			
H14.1	-0.01			
H14.2	-0.01			
C15	-0.01			
H15.1	0.00			
H15.2	0.00			
C16	0.02			
H16.1	0.01			
H16.2	0.01			
H16.3	0.01			



the calculations were performed analogously using the energetically optimized  $C_{16}TMA^+$  geometry with a shortened alkyl chain as input. The resulting partial charges, bond lengths, and angles of  $C_nTMA^+$  are virtually independent of the alkyl chain length. In agreement with previous studies by Huibers and Minisini et al. [115, 116], in which different quantum chemical methods of charge determination were compared, the bulk of the positive charge of  $C_nTMA^+$  (84%) was identified to be located on the headgroup and the  $\alpha$ -methylene group, while the remaining positive charge (16%) is delocalized over the alkyl chain (see table 3.2).

To keep the computational effort within reasonable boundaries<sup>3</sup>, all bond lengths within the  $C_nTMA^+$  ion were fixed, and only bond bending and torsional angles were given the freedom to change in the MC simulations. For the same reason, bond angles within  $CH_2$  and  $CH_3$  groups were kept constant, assuming that changes of intramolecular energy within these groups have negligible impact on the equilibrium structures of the simulated aggregates. The remaining OPLS-AA interaction parameters  $\sigma_i$ ,  $\epsilon_i$ ,  $k_{\theta,i}$ , and  $V_{l,i}$  that were required to carry out the MC simulations (see subsection 2.4.1) were taken from Jorgensen et al. [85, 88, 90], Price et al. [91], and Meleshyn and Bunnenberg [25].

### 3.2.4 The Water Model

The water molecules were modeled on the basis of the *Transferable Intermolecular Potential Four Point* (TIP4P) water model, parameters for which are included in the OPLS-AA force field [85, 86]. The TIP4P water molecule exhibits four interaction sites, namely one oxygen atom, two hydrogen atoms, and one massless charge R, which is located between the two hydrogen atoms on the symmetry axis of the molecule. The TIP4P geometry is defined by the angle  $\angle(HOH) = 104.52^\circ$  and the bond lengths  $r(H - O) = 0.9572 \text{ \AA}$  and  $r(R - O) = 0.15 \text{ \AA}$ . The partial charges of the molecule are located on the hydrogen atoms and the charge interaction site R with  $q_H = 0.52 e$  and  $q_R = -1.04 e$ . The only interaction site that is subjected to

---

<sup>3</sup>Even with these constraints, the simulation of a single system took up to several months of CPU time (see section 3.3).

Lennard-Jones interactions with other atoms or molecules is the oxygen atom. Thus, the parameters  $\epsilon_i$  and  $\sigma_i$  (see equation (2.13)) are set to zero for the hydrogen atoms and the charge interaction site.

### 3.2.5 The Simulation Cells

The simulation cells of the montmorillonite and the muscovite systems (see figure 3.4) had extensions of eight unit cells in the lateral direction, corresponding to mineral surface areas of  $\sim 371 \text{ \AA}^2$  and  $\sim 374 \text{ \AA}^2$ , respectively. Employing three-dimensional periodic boundary conditions, simulation cells with such lateral dimensions have been proven to be sufficiently large to reproduce macroscopic properties of clay-water systems without being influenced by the artificial long-range system periodicity [92] (see subsection 2.4.2).

For montmorillonite, the cell contained one mineral layer with a thickness of approximately  $7 \text{ \AA}$ . For muscovite, two layers with a total thickness of approximately  $20 \text{ \AA}$  were modeled. The mineral layers were fixed at the bottom of the simulation cells. To model external mineral surfaces, the simulation cells were expanded in the  $z$ -direction by vacuum slabs pulling the mineral layers  $100 \text{ \AA}$  away from their neighboring periodic images. As a result of the cleaving, the mineral surfaces that are exposed to the vacuum interface exhibit cation coverages of  $0.375 \text{ Na}^+ / A_{\text{uc}}$  for montmorillonite and  $1 \text{ K}^+ / A_{\text{uc}}$  for muscovite, corresponding to half of the respective interlayer coverages.

For the initial configurations, the inorganic sodium and potassium cations were uniformly distributed in the lateral direction and positioned  $7.5 \text{ \AA}$  above the mineral surfaces ( $z = 7.5 \text{ \AA}$ ). Both monolayer and bilayer aggregate structures (see figure 3.5) of  $\text{C}_n\text{TMA}^+$  were studied. For the monolayer arrangements and the inner layers of the bilayer arrangements, the  $\text{C}_n\text{TMA}^+$  ions were oriented with their headgroups facing the muscovite surface. For the outer layers of the bilayer arrangements, they were oriented with their headgroups facing the water-vacuum interface. The  $\text{C}_n\text{TMA}^+$  ions were uniformly distributed in the lateral

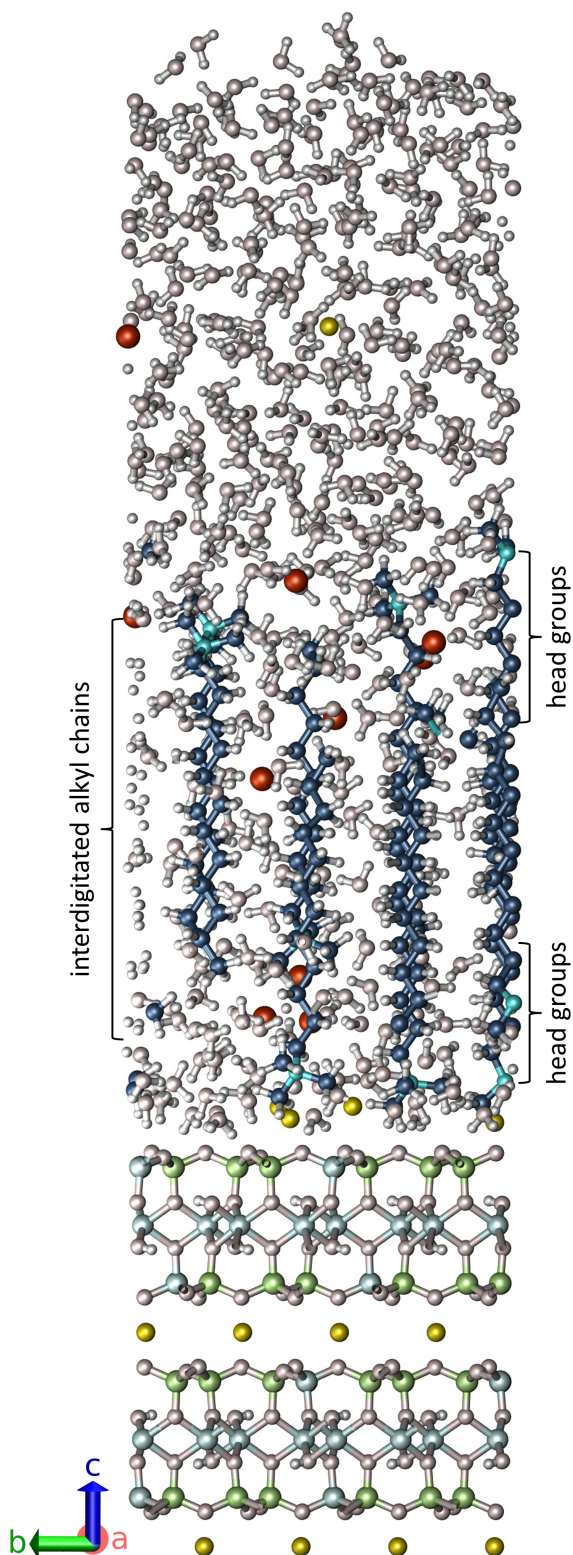


**Figure 3.4** – Snapshot of the simulated equilibrium configuration for the bilayer arrangement at a coverage of  $1.25 \text{ C}_{12}\text{TMA}^+ / A_{uc}$ , viewed parallel to the muscovite–water interface. Ball and stick colors: yellow ( $\text{K}^+$ ), light blue (Al), light green (Si), reddish gray (O), white (H), turquoise (N), dark blue (C), red ( $\text{Cl}^-$ ).

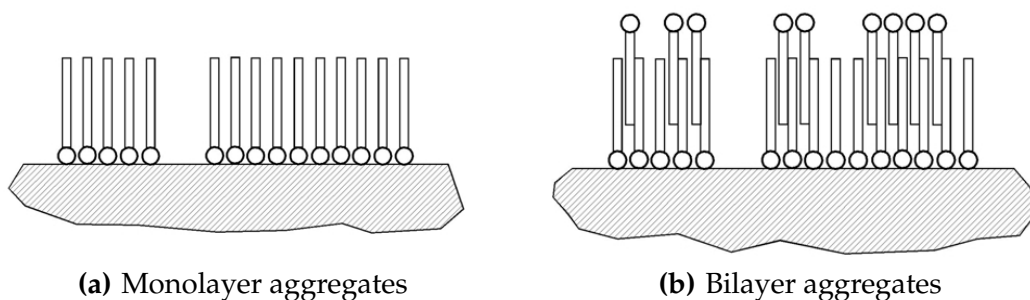


**Figure 3.5** – Schematic representations of (a) monolayer and (b) bilayer aggregates of organic cations assembled on mineral surfaces.

direction and the distances  $z$  between the nitrogen atoms of the headgroups and the mineral surfaces were set to  $4.95 \text{ \AA}$  for the inner layers and to  $32.5 \text{ \AA}$ ,  $27.5 \text{ \AA}$ , and  $22.45 \text{ \AA}$  for the outer layers of  $C_{16}\text{TMA}^+$ ,  $C_{12}\text{TMA}^+$ , and  $C_8\text{TMA}^+$  ions, respectively. For montmorillonite, the monolayer and bilayer aggregates were studied at coverages ranging from  $0.125 C_n\text{TMA}^+ / A_{uc}$  to  $1 C_n\text{TMA}^+ / A_{uc}$  and from  $0.5 C_n\text{TMA}^+ / A_{uc}$  to  $1.5 C_n\text{TMA}^+ / A_{uc}$ , respectively. For muscovite, the coverages ranged from  $0.25 C_n\text{TMA}^+ / A_{uc}$  to  $1.25 C_n\text{TMA}^+ / A_{uc}$  and from  $0.5 C_n\text{TMA}^+ / A_{uc}$  to  $1.5 C_n\text{TMA}^+ / A_{uc}$  for the monolayer and bilayer aggregates, respectively. To maintain charge balance, a corresponding amount of chloride was positioned at  $z = 15 \text{ \AA}$ .

Finally, 463 water molecules per simulation cell ( $\sim 58 \text{ TIP4P} / A_{uc}$ ) were distributed randomly above the mineral surfaces in slabs, the thicknesses of which were obtained for each simulated  $C_n\text{TMA}^+$  coverage from extensive preliminary test runs. For the unmodified mineral surfaces, the used amount of water results in water film thicknesses of approximately  $38 \text{ \AA}$ , which is less than twice the end-to-end distance of approximately  $23.5 \text{ \AA}$  of a fully extended  $C_{16}\text{TMA}^+$  ion. However, an addition of  $C_n\text{TMA}^+$  ions leads to the displacement of water molecules and thus to an increase of the water film thickness. In this way, it is ensured that the examined monolayer and bilayer aggregates are fully immersed in water.

A total of 24 and 33 systems containing organic cations were modeled for muscovite and montmorillonite, respectively (see table 3.3). In addition to this, two reference systems consisting of the unmodified montmorillonite and muscovite surfaces and water only, were studied.

**Table 3.3** – Overview of the simulated mineral-water-organic systems.

			Coverage ( $C_n\text{TMA}^+ / A_{\text{uc}}$ )	Total number of systems
<b>Muscovite</b>	$C_{16}\text{TMA}^+$	monolayer	0.25 – 1.25	5
		bilayer	0.5 – 1.5	5
	$C_{12}\text{TMA}^+$	monolayer	0.25 – 1	3
		bilayer	0.5 – 1.5	4
	$C_8\text{TMA}^+$	monolayer	0.25 – 1	3
		bilayer	0.5 – 1.5	4
<b>Montmorillonite</b>	$C_{16}\text{TMA}^+$	monolayer	0.125 – 1	6
		bilayer	0.5 – 1.5	5
	$C_{12}\text{TMA}^+$	monolayer	0.125 – 1	6
		bilayer	0.5 – 1.5	5
	$C_8\text{TMA}^+$	monolayer	0.125 – 1	6
		bilayer	0.5 – 1.5	5

### 3.3 Equilibration of the Systems

All systems were equilibrated in the *NVT* ensemble at a temperature of 298 K employing the *mclay*-code (see section 2.1). To ensure that the ions and the mineral surface were hydrated prior to the start of the equilibration, only water molecules were moved in the first 2 000 *Monte Carlo cycles*.<sup>4</sup> After this pre-equilibration phase, trial moves were allowed for all particles. Each simulation run started with an initial

<sup>4</sup>Each *MC cycle* comprises *m* trial moves with *m* denoting the number of movable particles in the studied system.

distribution of the particles as described in subsection 3.2.5. These arbitrary arrangements of atoms and molecules in the simulation cells were far from representing the equilibrium states of the systems. Actually, these initial states possessed very high total potential energies and thus very low Boltzmann weights, mainly originating from overlaps of the Van der Waals radii of the randomly inserted water molecules with those of other atoms or molecules (see equation (2.13)).

Accordingly, at the beginning of each simulation run, only very few trial moves were rejected (see section 2.3) and the total system energy decreased rapidly. For instance, for the bilayer arrangement at the muscovite surface at a coverage of  $0.75 C_{16}TMA^+ / A_{uc}$ , the initial state of the system had a total potential energy of  $2 \times 10^{12}$  kJ/mol. After 100 MC cycles and 1 000 MC cycles, in which only water molecules were moved, the energy had decreased to  $2 \times 10^5$  kJ/mol and  $-3 \times 10^4$  kJ/mol, respectively. The convergence profile for the total potential energy in figure 3.6 indicates the appearance of an energy step after 2000 MC cycles, which is due to the permission of trial moves for all particles.

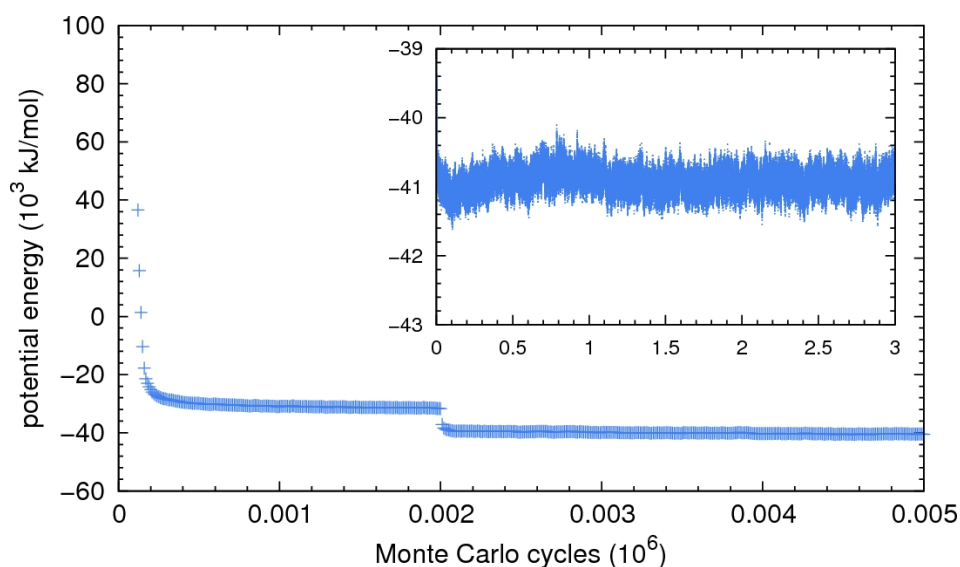


**Figure 3.6** – Convergence profile of the total potential energy for the bilayer arrangement at the cleaved muscovite surface at a coverage of  $0.75 C_{16}TMA^+ / A_{uc}$ .

A system can be assumed to have attained the equilibrium state upon the convergence of its average total potential energy to a constant value. This was in general achieved after several 100 000 MC cycles (see figure 3.6). However, it cannot be ruled out that the convergence of the MC algorithm to a local energy minimum is erroneously judged as the achievement of the global energy minimum, and, that consequently, the sampled system properties do not represent the equilibrium state but some local minimum of Helmholtz free energy [76, 92].

In several of the simulated systems, even though the average total potential energy seemed to have converged, drifts of ions towards or away from the mineral surface still occurred in excess of the random displacements around their equilibrium positions expected otherwise. In the first simulation series of the muscovite-water-organics systems, the structural changes were monitored for each system based on short test samplings every 100 000 MC cycles over 100 MC cycles, each (see figure 3.7).

For example, for the bilayer arrangement at a coverage of  $0.75 C_{16}TMA^+ / A_{UC}$ , the vertical atomic density profiles indicate that directed vertical movement of potassium occurred up to the adsorption of all potassium ions on the muscovite surface after approximately  $1.3 \times 10^6$  MC cycles (see figure 3.7(a)). The extension of the aggregates in the vertical direction (see figure 3.7(b)) converged to the value of approximately 33 Å after  $\sim 1.7 \times 10^6$  MC cycles.<sup>5</sup> In general, the simulated bilayer systems showed slower equilibration than the monolayer ones. The analysis of the vertical atomic density profiles sampled for each muscovite system (see figures 3.7 and A.2) indicated that equilibration phases of two and three million MC cycles were sufficient for the monolayer and bilayer arrangements, respectively.

Up to several months of CPU time were needed to complete the equilibration of one system on an Intel Xeon E5472, 3.0 GHz processor of the *Central Services Information Technology*<sup>6</sup> (RRZN) compute-server *Paris*.<sup>7</sup> In October 2010, the

---

<sup>5</sup>Vertical atomic density profiles for the other movable species of the system are presented in figure A.2 of the extended figures section.

<sup>6</sup>Previously *Regionales RechenZentrum für Niedersachsen* (RRZN).

<sup>7</sup>Paris stands for *Parallel computer for institutes*.

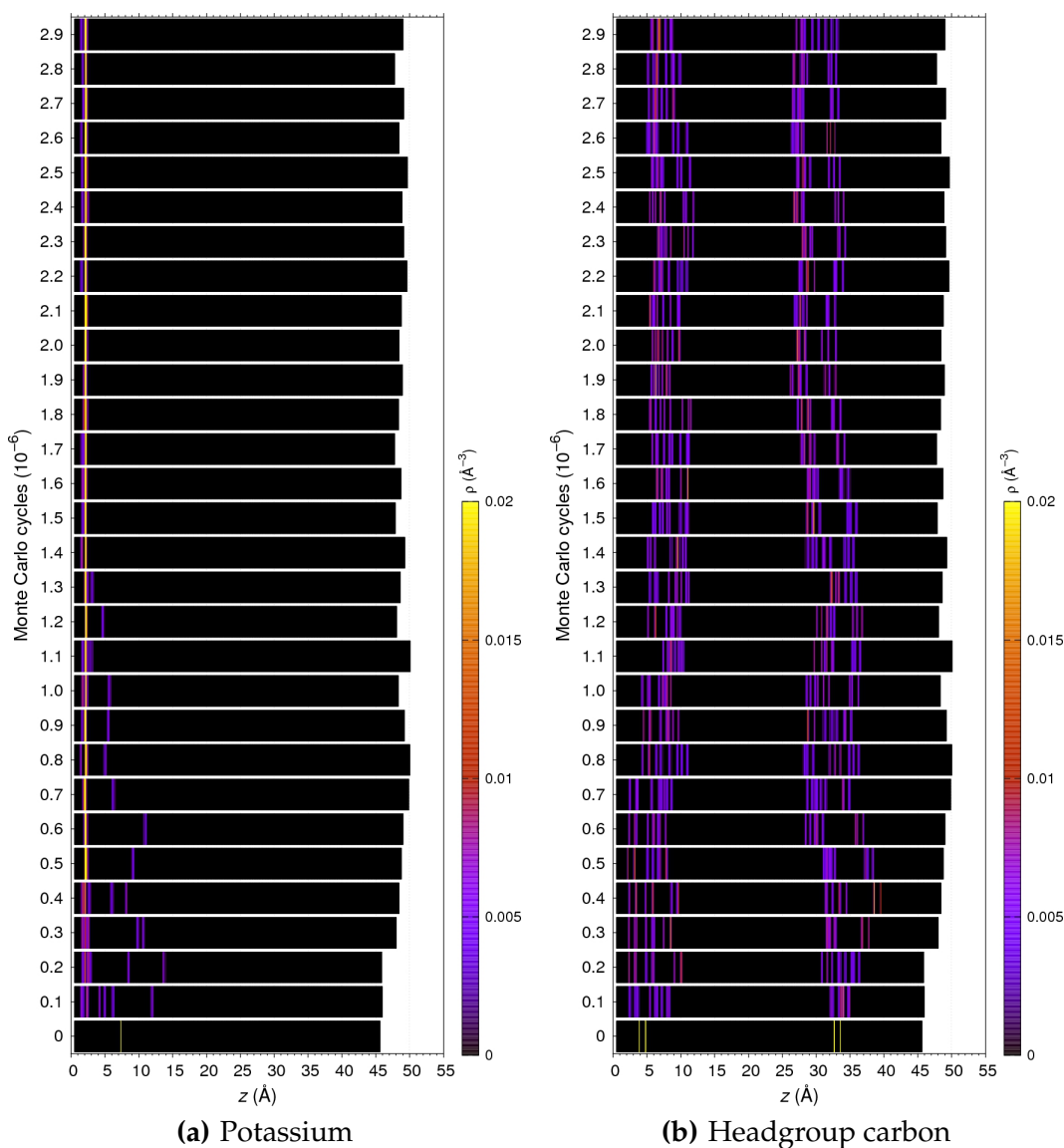


**Figure 3.7** – Vertical atomic density profiles for (a) potassium and (b) headgroup carbon atoms of  $C_{16}TMA^+$  as functions of the distance  $z$  from the muscovite surface for the bilayer arrangement at a coverage of  $0.75 C_{16}TMA^+/A_{uc}$ . The graphs show the evolution of the atomic densities of the system with simulation time. The density profiles were sampled every 100 000 MC cycles over 100 MC cycles, each. The extension of the water film between the muscovite–water interface ( $z = 0 \text{ \AA}$ ) and the water–vacuum interface is indicated by black bars.



new RRZN compute-server *Tane*<sup>8</sup> was available. It consists of 96 nodes having 12 Intel Xeon CPU X5670, 2.93GHz processors, each. This enormous upgrade of available computing resources allowed the extension of the equilibration phase for the second simulation series of montmorillonite-water(-organics) systems to four million MC cycles.

### 3.4 Final Sampling

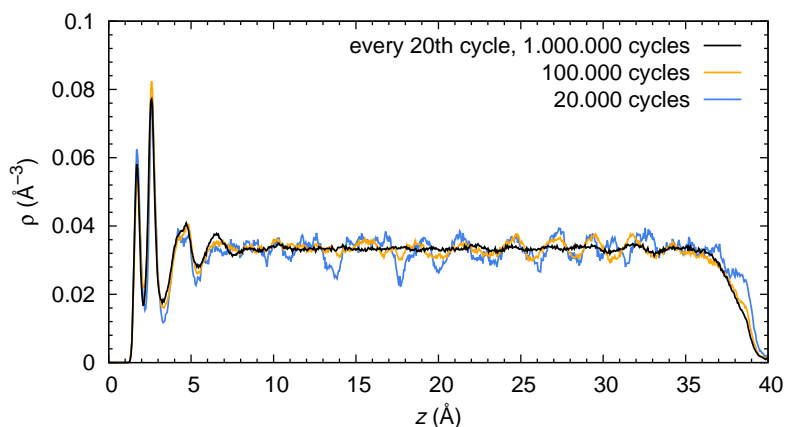
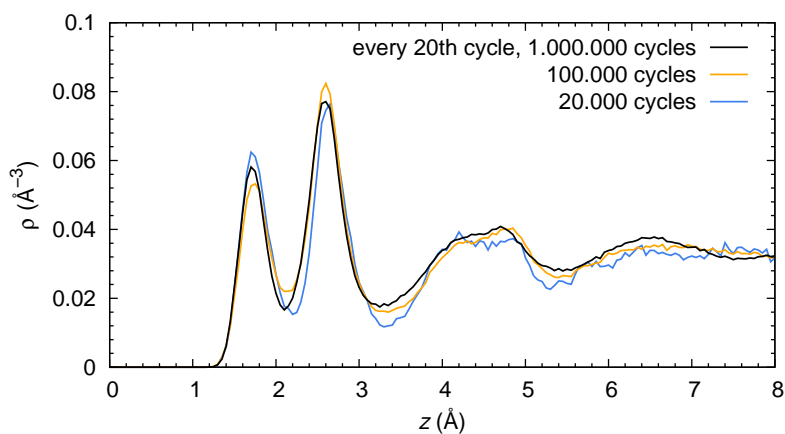
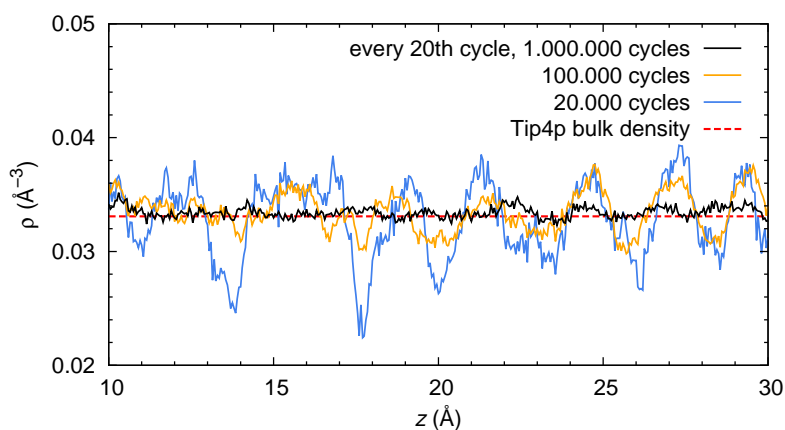
The final sampling of the potential energies and structural properties of the muscovite-water-organics systems was carried out by collecting data for averages once each MC cycle over 20 000 MC cycles. This number of sampling cycles had turned out as a practicable choice in the preceding simulation studies at the institute [28, 29]. The CPU time needed for the sampling of one system increased with the system size and ranged between four and nine days.

After the new RRZN compute server *Tane* was available in October 2010, the effect of an increased length of the sampling interval on the random noise in the simulations results could be studied in detail. The extension of the sampling interval to 100 000 MC cycles led to five-fold increased computing times needed for the sampling of the system properties. To keep the computational effort within reasonable boundaries, but nevertheless sample over a broader range of MC cycles, additional sampling was carried out for one million MC cycles, collecting data only once each 50<sup>th</sup> MC cycle. This approach led to a 50-fold increased sampling interval at the expense of increased computing times by factors between only four and six.

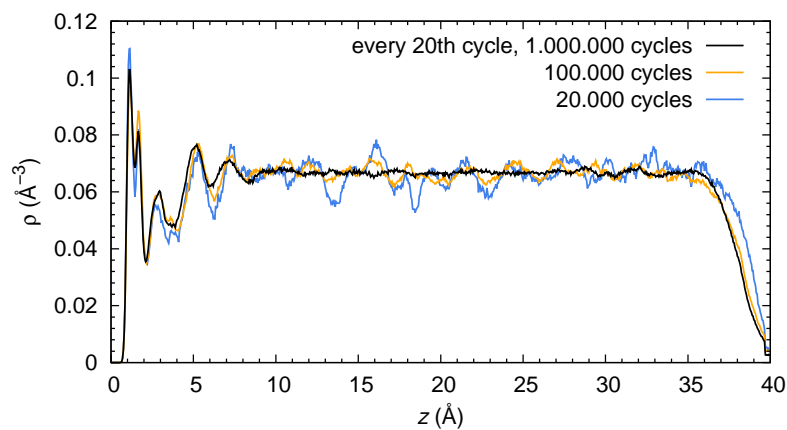
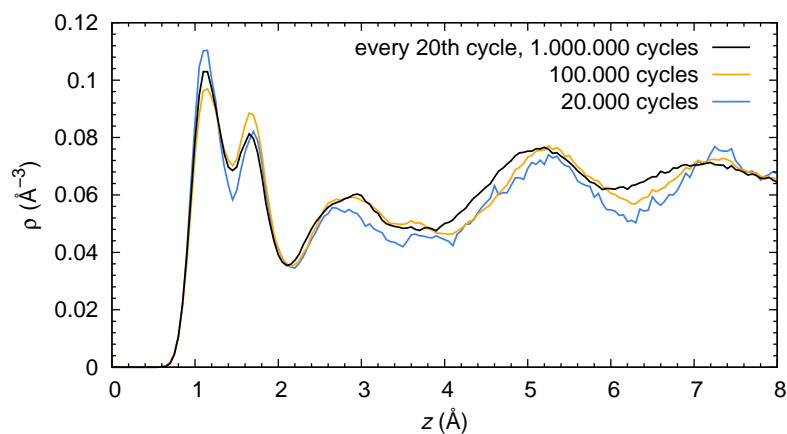
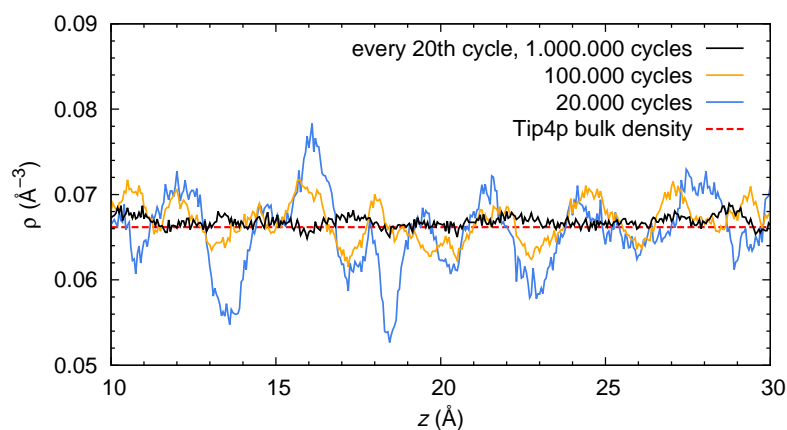
The vertical atomic density profiles for the inorganic muscovite-water reference system give insight into the density distribution of the water film adsorbed on the mineral surface. Within a distance of  $z \in [10 \text{ \AA}, 30 \text{ \AA}]$  from the muscovite surface, the water film exhibits a density of approximately  $0.033 \text{ \AA}^{-3}$ , which is comparable to the bulk density of TIP4P (see figures 3.8(c) and 3.9(c) and table 3.4). The increase of

---

<sup>8</sup>*Tane* stands for *Teraflop analytisch-numerische Einheit*.

(a)  $0 \text{ \AA} \leq z \leq 40 \text{ \AA}$ (b)  $0 \text{ \AA} \leq z \leq 8 \text{ \AA}$ (c)  $10 \text{ \AA} \leq z \leq 30 \text{ \AA}$ 

**Figure 3.8** – Vertical atomic density profiles for water oxygen as functions of the distance  $z$  from the unmodified muscovite surface. The data was obtained after sampling over different numbers of MC cycles. The red line in (c) marks the bulk density of TIP4P at 298 K [86].

(a)  $0 \text{ \AA} \leq z \leq 40 \text{ \AA}$ (b)  $0 \text{ \AA} \leq z \leq 8 \text{ \AA}$ (c)  $10 \text{ \AA} \leq z \leq 30 \text{ \AA}$ 

**Figure 3.9** – Vertical atomic density profiles for water hydrogen as functions of the distance  $z$  from the unmodified muscovite surface. The data was obtained after sampling over different numbers of MC cycles. The red line in (c) marks the bulk density of TIP4P at 298 K [86].

**Table 3.4** – Average water oxygen density in the vertical region of  $10 \text{ \AA} \leq z \leq 35 \text{ \AA}$  of the muscovite-water reference system. The data was obtained after sampling over different numbers of MC cycles. For comparison: the bulk density of TIP4P is  $0.033 \text{ \AA}^{-3}$  at 298 K [86].

Sampling interval (MC cycles)	Water oxygen density for $10 \text{ \AA} \leq z \leq 35 \text{ \AA}$ ( $\text{\AA}^{-3}$ )
20 000	$0.0329 \pm 0.0034$
100 000	$0.0335 \pm 0.0017$
1 000 000	$0.0334 \pm 0.0005$

the sampling interval length results in a significant decrease of the random noise in the water density profiles. For sampling over 20 000 MC cycles, the calculated values of the water oxygen density exhibit a standard deviation of 10.3 %. The increase of the sampling interval to 100 000 and one million MC cycles leads to a significant decrease of the standard deviations by factors of approximately two and seven to only 5.2 % and 1.4 %, respectively (see table 3.4).

In agreement with previous experiments and simulation studies of water films adsorbed on unmodified muscovite [27, 33, 66, 117], a layered structure of the adsorbed water film induced by the mineral–water interface was observed in the region of  $z \leq 8 \text{ \AA}$  (see figures 3.8(b) and 3.9(b)). As expected, the length of the sampling interval negligibly affects the locations of the minima and the maxima of the density distributions. In the range of  $z > 3.3 \text{ \AA}$ , the density curves obtained after sampling over greater intervals of MC cycles are significantly smoother. For  $z \geq 35 \text{ \AA}$ , a decrease of the water density at the water–vacuum interface was observed. For  $z > 30 \text{ \AA}$ , the density profiles that were obtained after sampling over one million MC cycles reveal a periodic structure that originates from the impact of the water–vacuum interface (see figures 3.8(a) and 3.9(a)). For the shorter sampling intervals, this structure is covered by noise.

The lateral atomic density profiles for water oxygen and hydrogen at the muscovite–water interface (see figure 3.10) were sampled within the first peaks ( $z < 2.2 \text{ \AA}$ )

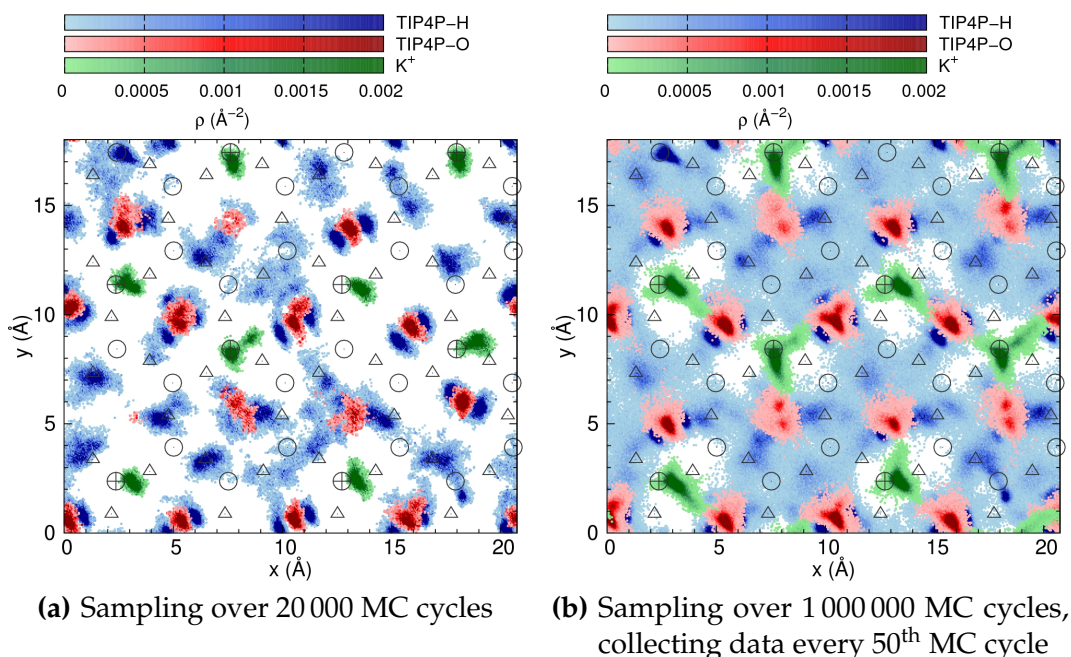


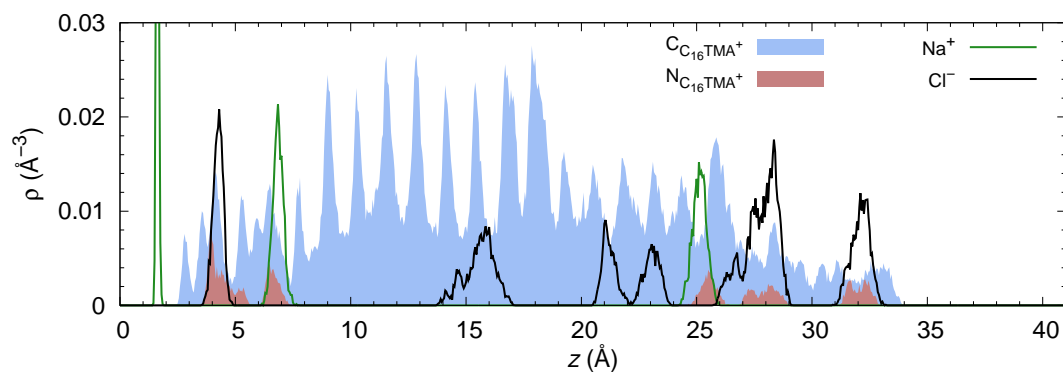
**Figure 3.10** – Lateral atomic density profiles for water and potassium at the unmodified muscovite–water interface. The data was obtained after sampling over (a) 20 000 and (b) one million MC cycles. The oxygen and hydrogen densities were sampled within the first peaks of the corresponding vertical atomic density profiles ( $z < 2.2 \text{ \AA}$ ). The  $\text{K}^+$  density was sampled within  $5.5 \text{ \AA}$  from the muscovite surface. The circles, crossed circles, and triangles represent silicon, aluminum, and basal oxygen atoms of the tetrahedral sheet at the muscovite–water interface, respectively (cf. figure 3.2(b)).

of the corresponding vertical atomic density profiles. They indicate the adsorption of strongly bound water molecules above the centers of the ditrigonal cavities of the muscovite surface, e. g., at  $(x, y) \sim (10 \text{ \AA}, 10 \text{ \AA})$ . These water molecules are doubly hydrogen-bonded to the muscovite surface and determine the first peaks of the vertical oxygen and hydrogen density distributions with  $z_{\text{oxygen}} \leq 2.2 \text{ \AA}$  and  $z_{\text{hydrogen}} \leq 1.45 \text{ \AA}$  (cf. figures 3.8 and 3.9). The density profiles further indicate that no water molecules are adsorbed above the tetrahedral substitutions of the muscovite surface (see figure 3.10, e. g., at  $(x, y) \sim (13 \text{ \AA}, 2 \text{ \AA})$ , for further details see section 4.3). Obviously, the calculated lateral density profiles strongly depend on the

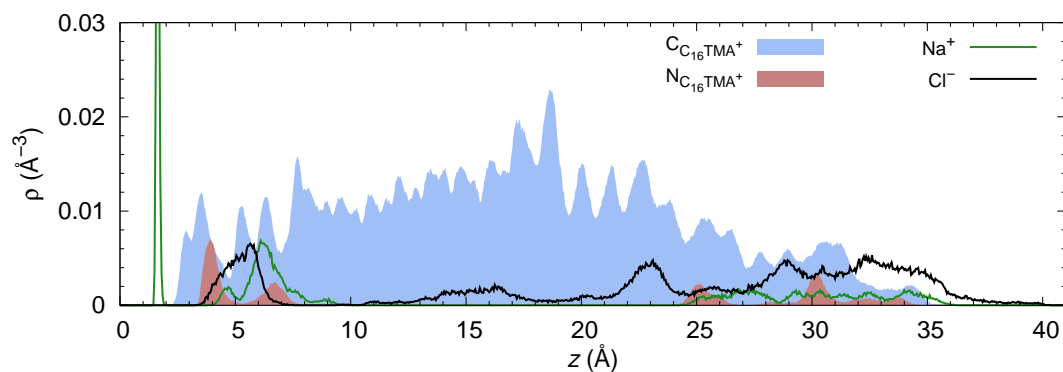
number of MC cycles used for sampling (cf. figures 3.10(a) and 3.10(b)). This effect is particularly pronounced for the distribution of water hydrogen. This is due to water molecules of the second water sublayer characterized by  $2.2 \leq z_{\text{oxygen}} \leq 3.3 \text{ \AA}$  (see figure 3.8(b)). These water molecules are only singly hydrogen-bonded to the muscovite surface and show a significantly higher mobility in the lateral direction than the doubly hydrogen-bonded molecules. As a result, their lateral density distribution obtained after sampling over one million MC cycles is broadened as compared to that obtained after sampling over 20 000 MC cycles.

In summary, the increase of the length of the sampling interval remarkably increases the quality of the sampled structural properties. For this reason, the montmorillonite-water(-organics) systems of the second part of this study were sampled over one million MC cycles collecting data each 50<sup>th</sup> MC cycle.

For the  $\text{C}_{16}\text{TMA}^+$  bilayer arrangement at the montmorillonite surface at a coverage of  $0.75 \text{ C}_{16}\text{TMA}^+ / A_{\text{uc}}$ , the vertical adsorption positions for the headgroup nitrogen atoms that face the mineral surface are located in the region of  $z \in [3.5 \text{ \AA}, 7.5 \text{ \AA}]$  for both compared sampling intervals of 20 000 and one million MC cycles (see figure 3.11). In contrast to these ions that are adsorbed on the montmorillonite-water interface, the ions whose headgroups face the aggregate-water interface show a higher mobility. Their density distribution is broadened from an interval of  $25.8 \text{ \AA} \leq z \leq 32.8 \text{ \AA}$  calculated after sampling over 20 000 MC cycles to an interval of  $24.3 \text{ \AA} \leq z \leq 34.2 \text{ \AA}$  calculated after sampling over one million MC cycles. For the inorganic sodium and chloride ions, a similar behavior was observed. The shape of the peak for the sodium ions adsorbed at  $z = 2.15 \text{ \AA}$  does not change noticeably with the increase of the length of the sampling interval, whereas the distribution functions for the ions that are detached from the muscovite surface are significantly broadened.



(a) Sampling over 20 000 MC cycles

(b) Sampling over one million MC cycles, collecting data every 50<sup>th</sup> MC cycle

**Figure 3.11** – Vertical atomic density profiles for carbon and nitrogen atoms of  $C_{16}TMA^+$ , sodium, and chloride as functions of the distance  $z$  from the montmorillonite surface for the bilayer arrangement at a coverage of  $0.75 C_{16}TMA^+ / A_{uc}$ . The data was obtained after sampling over (a) 20 000 and (b) one million MC cycles. The density profiles for  $Na^+$  and  $Cl^-$  are scaled by a factor of 20.





---

## Aggregation of $C_n\text{TMA}^+$ Ions at the Cleaved Muscovite–Water Interface

### 4.1 Overview of Experimental Findings

In the past decades, many experimental studies have been performed to determine the structures of surfactant aggregates assembled on cleaved muscovite–water interfaces. Alkyltrimethylammonium ions aggregate at mineral–water interfaces and adsorb with their positively charged hydrophilic headgroups facing the surface [53, 118, 119]. At solution concentrations far below the *critical micelle concentration*<sup>1</sup> (CMC), island-like aggregate structures are formed [78, 79]. With increasing concentration, monolayer aggregates covering the surface are observed [53, 119, 120]. The hydrophobic alkyl chains of the aggregated surfactant ions face the solution, so that the organically modified muscovite surface becomes hydrophobic. At concentrations around the CMC, a second layer with headgroups facing the solution builds up, and the surface is rendered hydrophilic again. *Atomic force microscope* (AFM) images of  $C_n\text{TMABr}$ ,  $n \in \{12, 14, 16\}$ , aggregates self-assembled on mica at concentrations of approximately twice the critical micelle concentration show striped aggregate structures that are commonly interpreted as cylindrical micelles [121–126].

---

<sup>1</sup>The *critical micelle concentration* is defined as that concentration of surfactants in solution above which micelles form.

In *infrared* (IR) and *near edge X-ray absorption fine structure spectroscopy* (NEXAFS) experiments, the conformational order within the aggregates was observed to increase with both increasing alkyl chain length  $n$  [127, 128] and surface coverage of surfactant ions [78, 79]. *Surface force apparatus* (SFA) and *neutron reflectometry* (NR) studies indicate that a certain amount of water remains within the aggregate regions [53, 129, 130].

Depending on the conditions of the studied systems, the equilibration of the aggregate structures assembled on the cleaved muscovite surface can proceed very slowly. For  $C_{16}\text{TMA}^+$ , the striped aggregates evolve into flat bilayer structures within approximately one day, whereas the striped structures of the aggregates formed by shorter-chained  $C_n\text{TMA}^+$  ions remain stable [122–124]. In some cases, structural changes are observed to occur for time spans of days up to several months [53, 78, 79]. Prevalently, rapidly occurring initial surfactant adsorption phases are followed by very slowly occurring equilibration phases. These equilibration phases are characterized by low surfactant adsorption rates, exchange competition between the surfactant ions and inorganic muscovite cations, rearrangement of the surfactant aggregates, and the gradual release of the inorganic surface cations paired with initially co-adsorbed surfactant counterions out of the aggregate regions (see section 4.6).

## 4.2 Adsorption Positions of the $C_n\text{TMA}^+$ Ions

Figure 4.1 gives an overview of the vertical arrangement of the  $C_n\text{TMA}^+$  ions at the muscovite–water interface. The vertical atomic density profiles indicate that headgroup carbon atoms of  $C_n\text{TMA}^+$  can approach as close as approximately 2 Å to the muscovite surface with no other ions or molecules interposed between. Some of the basal oxygen atoms of the muscovite surface replace water molecules of the first hydration shells of the adsorbed  $C_n\text{TMA}^+$  ions, which are thus called *inner-sphere surface complexes* [131] (see figure 4.2).

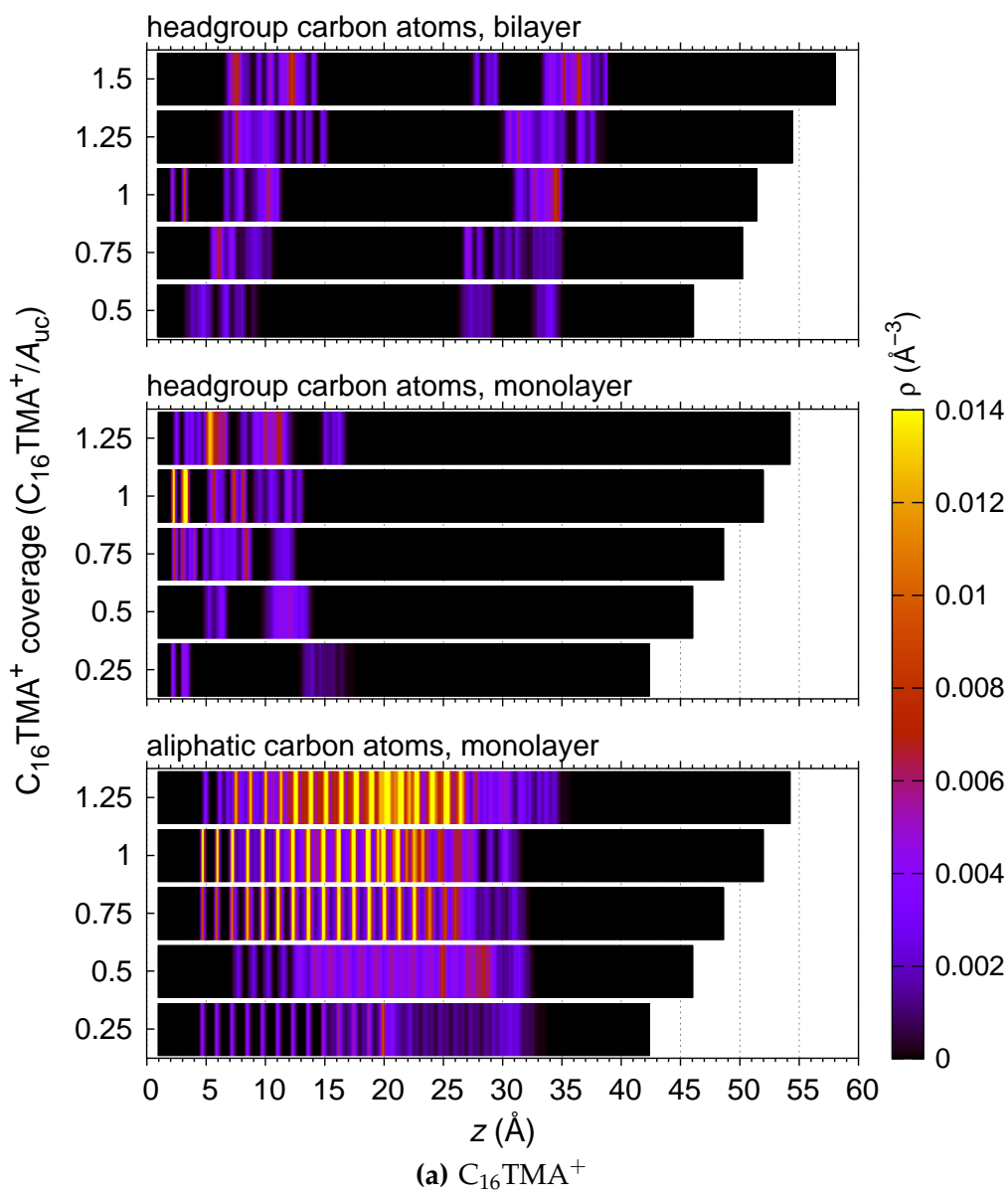


**Figure 4.1** – (a) Vertical atomic density profiles for carbon atoms of  $C_{16}TMA^+$  headgroups and alkyl chains as functions of the distance  $z$  from the muscovite surface. Coverages ranging from  $0.25 C_{16}TMA^+/A_{uc}$  to  $1.25 C_{16}TMA^+/A_{uc}$  and from  $0.5 C_{16}TMA^+/A_{uc}$  to  $1.5 C_{16}TMA^+/A_{uc}$  are shown for monolayer and bilayer arrangements, respectively. For each simulated system, the extension of the water film between the muscovite–water interface ( $z = 0 \text{ \AA}$ ) and the water–vacuum interface is indicated by a black bar.

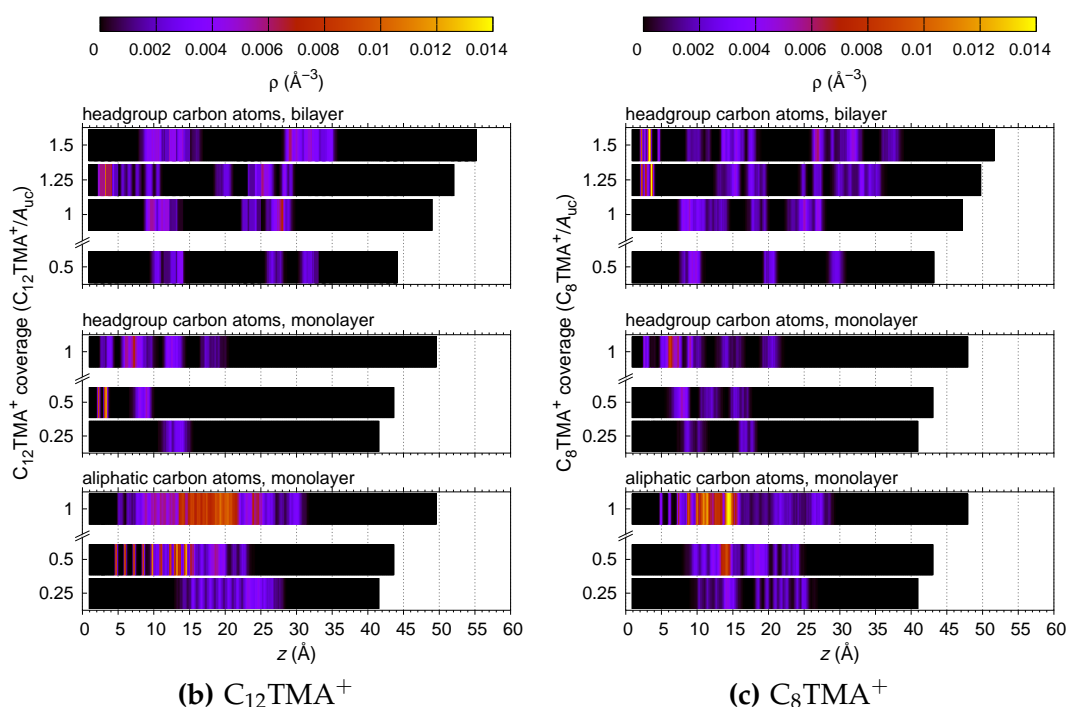


**Figure 4.1** – continued. Vertical atomic density profiles for carbon atoms of (b)  $C_{12}\text{TMA}^+$ , and (c)  $C_8\text{TMA}^+$  headgroups and alkyl chains as functions of the distance  $z$  from the muscovite surface.

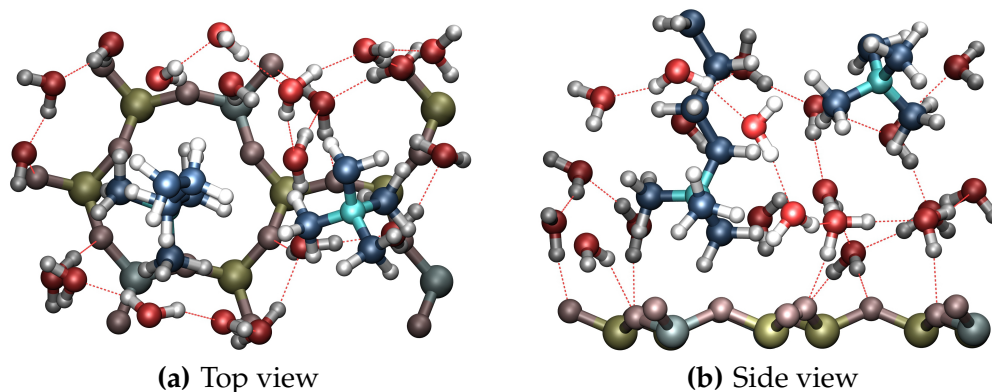


**Figure 4.2** – (a) Top view and (b) side view of an inner-sphere (left ion) and an outer-sphere (right ion) surface complex of  $C_{16}\text{TMA}^+$  on the muscovite surface. (a) and (b) are snapshots of the simulated equilibrium configuration for the monolayer arrangement at a coverage of  $1 C_{16}\text{TMA}^+ / A_{uc}$ . Ball and stick colors: dark yellow (Si), gray-blue (Al), dark rose (basal O), dark blue (C), turquoise (N), white (H), red (water O).

To estimate the maximum separation of inner-sphere adsorbed  $C_n\text{TMA}^+$  ions from the muscovite surface, the radius of their hydration shells can be used as a rough measure. It is commonly defined as the first minimum of the *radial distribution function*<sup>2</sup>  $g(r)$  of water oxygen around the considered ion.  $C_n\text{TMA}^+$  ions with headgroup atoms that are farther away from the surface than the respective radii of their hydration shells are separated from muscovite by at least one interposed atom and accordingly not adsorbed as inner-sphere complexes. Representative radial distribution functions around  $C_{16}\text{TMA}^+$  headgroup atoms are shown in figure 4.3. The calculated hydration shell radii are very similar for all three studied chain lengths ( $r_{\text{H-O}} = 3.6 \text{ \AA}$ ,  $r_{\text{C-O}} = 4.4 \text{ \AA}$ ,  $r_{\text{N-O}} = 6.2 \text{ \AA}$ ) and agree well with those calculated by Wang and Larson in a molecular dynamics study of  $C_{16}\text{TMACl}$  micelles in water utilizing the GROMOS96 force field [132].

The headgroup methyls of inner-sphere adsorbed  $C_n\text{TMA}^+$  ions penetrate the first water layer adsorbed on the muscovite surface as indicated by matching z-val-

<sup>2</sup>According to the definition by Allen and Tildesley [77], the radial distribution function  $g(r)$  represents the probability of finding a pair of atoms a distance  $r$  apart in the considered system relative to the probability expected for a completely random distribution of all particles at the same density.

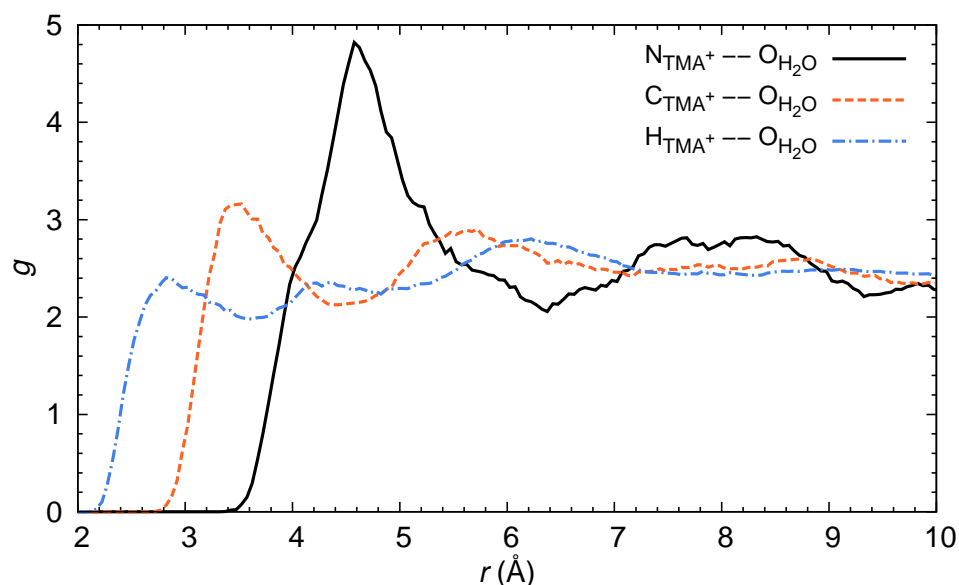


**Figure 4.3** – Radial distribution functions of water oxygen around  $C_{16}\text{TMA}^+$  headgroup atoms for the bilayer arrangement at a coverage of  $0.5 C_{16}\text{TMA}^+ / A_{\text{uc}}$ .

ues of approximately  $1.2 \text{ \AA}$  for the first maxima of the density distributions for water and  $C_n\text{TMA}^+$  hydrogen atoms (see figure 4.4). The  $z$ -values of the first maxima of the atomic density profiles for inner-sphere adsorbed  $C_n\text{TMA}^+$  ions show no dependence on the alkyl chain length and vary in the ranges of  $1.2 \text{ \AA}$  to  $1.7 \text{ \AA}$  for hydrogen,  $2.1 \text{ \AA}$  to  $2.6 \text{ \AA}$  for carbon, and  $3.3 \text{ \AA}$  to  $3.8 \text{ \AA}$  for hydrogen atoms.

The lateral adsorption positions of inner-sphere adsorbed  $C_n\text{TMA}^+$  ions are located above the ditrigonal cavities of the muscovite surface. Those methyl groups of the adsorbed surfactant ions that are closest to the surface are positioned directly above the cavity centers (see figure 4.2(a)). For the monolayer arrangement at a coverage of  $1 C_{16}\text{TMA}^+ / A_{uc}$ , inner-sphere complexes are adsorbed at  $(x, y) \sim (6 \text{ \AA}, 0 \text{ \AA})$ ,  $(19 \text{ \AA}, 4 \text{ \AA})$ , and  $(19 \text{ \AA}, 13 \text{ \AA})$  (see figure 4.5). The inner-sphere adsorption of  $C_n\text{TMA}^+$  ions above ditrigonal cavities leads to the desorption of strongly bound water molecules, which occupy these positions in the case of unmodified muscovite [27, 66] (see sections 3.4 and 5.1).

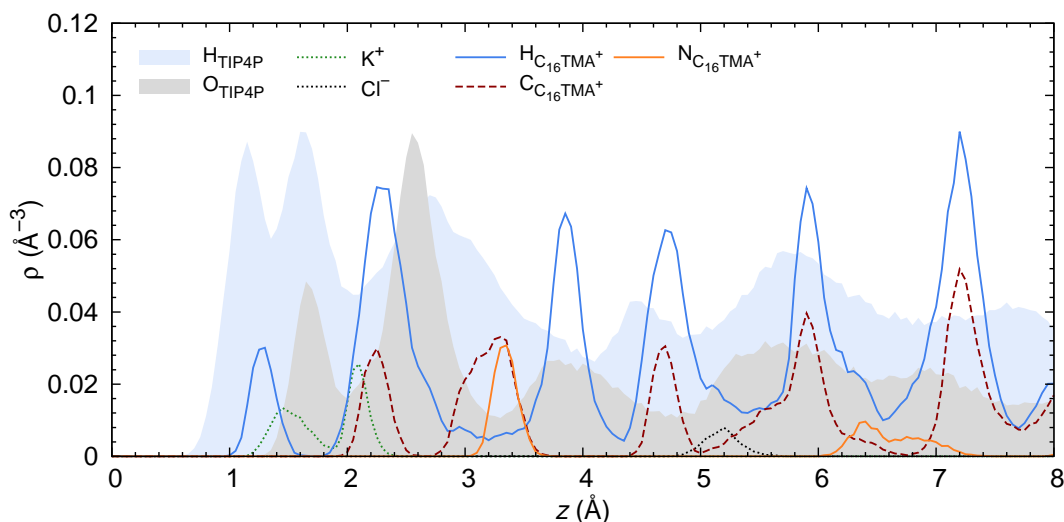


**Figure 4.4** – Vertical atomic density profiles for water,  $C_{16}\text{TMA}^+$ , potassium, and chloride as functions of the distance  $z$  from the muscovite surface for the monolayer arrangement at a coverage of  $1 C_{16}\text{TMA}^+ / A_{uc}$ .

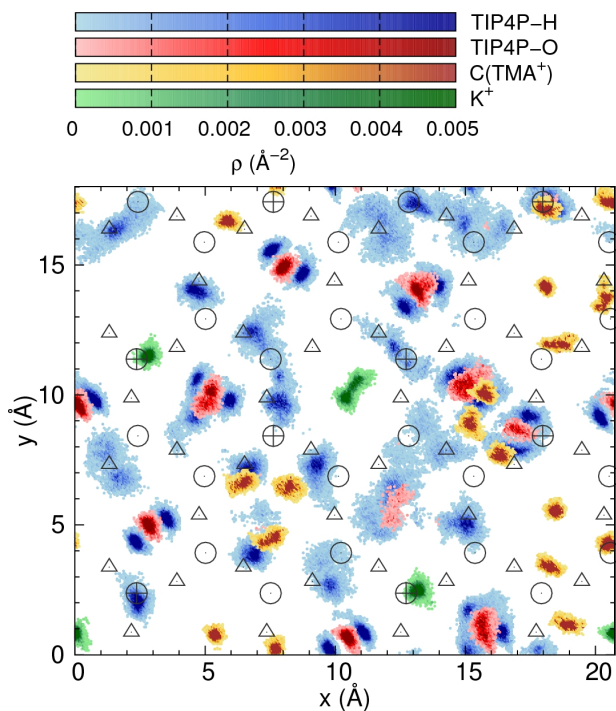


**Figure 4.5** – Lateral atomic density profiles for water,  $C_{16}\text{TMA}^+$  headgroup carbon and potassium at the muscovite–water interface for the monolayer arrangement at a coverage of  $1 C_{16}\text{TMA}^+ / A_{\text{uc}}$ . The oxygen and hydrogen densities were sampled within the first peaks of the corresponding atomic density profiles ( $z_{\text{water}} < 2.2 \text{ \AA}$ ). The headgroup carbon and potassium densities were sampled within  $8.4 \text{ \AA}$  and  $5.5 \text{ \AA}$  from the muscovite surface to ensure that all inner-sphere and outer-sphere adsorbed cations were taken into account. The circles, crossed circles, and triangles represent silicon, aluminum, and basal oxygen atoms of the tetrahedral sheet at the muscovite–water interface, respectively (cf. figure 3.2(b)).

The determined lateral adsorption position of  $C_n\text{TMA}^+$  agrees with that of  $C_{18}\text{TMA}^+$  on dehydrated muscovite as calculated in a molecular dynamics study by Heinz et al. [72]. However, the therein stated preference of cavities with more than one Al-defect could not be confirmed by this simulation study. At  $20^\circ\text{C}$ , Heinz et al. report an adsorption height for the nitrogen atoms of  $C_{18}\text{TMA}^+$  of  $3.8 \text{ \AA} \pm 0.1 \text{ \AA}$  above the plane of the tetrahedrally coordinated Si and Al atoms, corresponding to a height of  $3.15 \text{ \AA} \pm 0.1 \text{ \AA}$  above the basal plane of the muscovite surface. These values

are significantly lower than those calculated in this study. The height difference can be explained by the absence of water in the cited simulation study. Additionally performed simulation runs of systems devoid of water molecules with  $C_{16}\text{TMA}^+$  coverages ranging from  $0.25 C_{16}\text{TMA}^+ / A_{\text{uc}}$  to  $1.25 C_{16}\text{TMA}^+ / A_{\text{uc}}$  confirm this suggestion: On the dehydrated muscovite surface, the  $C_{16}\text{TMA}^+$  ions adsorb with their nitrogen atoms located at heights of  $z \in [3.05 \text{ \AA}, 3.3 \text{ \AA}]$  above the plane of basal oxygen atoms. These heights are in very good agreement with the values calculated by Heinz et al.

$C_n\text{TMA}^+$  ions whose nitrogen atoms are located at heights of  $z \in [5.5 \text{ \AA}, 8.4 \text{ \AA}]$  are adsorbed as *outer-sphere surface complexes* on muscovite. Their first hydration shells contain water molecules of the first water layer that is hydrogen-bonded to the muscovite surface, but no basal oxygen atoms of the muscovite surface. Accordingly, single water molecules that are interposed between them and the muscovite surface are not desorbed (see figure 4.2). The lateral atomic density profiles for  $C_{16}\text{TMA}^+$  headgroup carbon atoms indicate that for the monolayer arrangement at a coverage of  $1 C_{16}\text{TMA}^+ / A_{\text{uc}}$ , outer-sphere complexes are adsorbed at  $(x, y) \sim (7 \text{ \AA}, 5.5 \text{ \AA}), (16 \text{ \AA}, 8.5 \text{ \AA}),$  and  $(19 \text{ \AA}, 0 \text{ \AA})$  (see figure 4.5). Other than inner-sphere adsorbed  $C_n\text{TMA}^+$  ions, the outer-sphere adsorbed ones do not show specific lateral adsorption positions.

$C_n\text{TMA}^+$  ions that are characterized by larger  $z$ -values of the maxima of their nitrogen density distributions are separated from the mineral surface by at least two interposed water molecules and are thus not adsorbed as surface complexes on muscovite. In several systems, single  $C_{16}\text{TMA}^+$  ions are located as far as approximately  $16 \text{ \AA}$  away from the surface (see figure 4.1(a)). The observed maximum headgroup–surface separations increase further for  $C_{12}\text{TMA}^+$  and  $C_8\text{TMA}^+$  ions to approximately  $19 \text{ \AA}$  and  $21 \text{ \AA}$ , respectively (see figures 4.1(b) and 4.1(c)).

The amount of  $C_n\text{TMA}^+$  that is adsorbed on the muscovite surface can readily be estimated from cumulative density profiles for nitrogen (see figure 4.6). For the simulated monolayer arrangements of  $C_n\text{TMA}^+$  ions, the number of adsorption



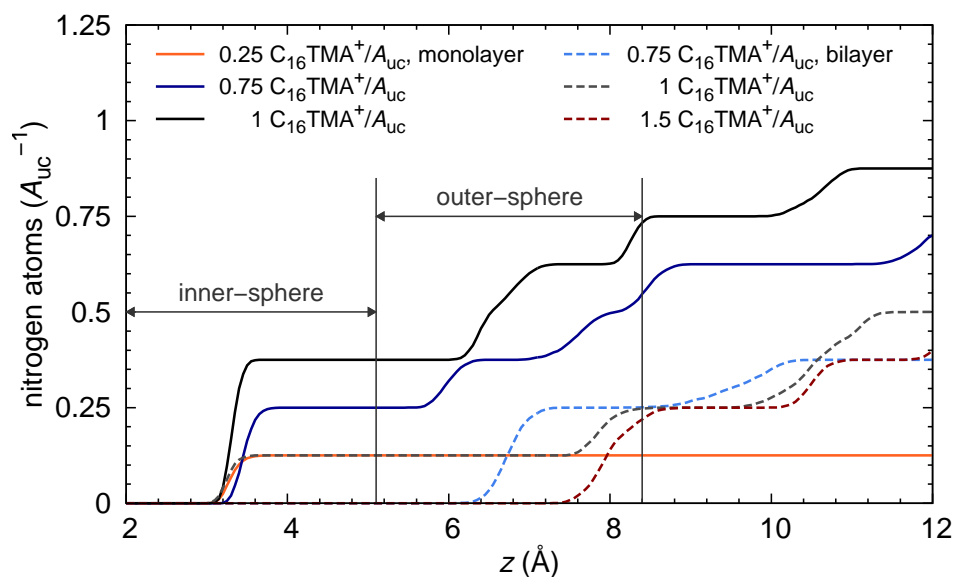


**Figure 4.6** – Cumulative contents of nitrogen atoms as functions of the distance  $z$  from the muscovite surface for monolayer and bilayer arrangements at different  $C_{16}\text{TMA}^+$  coverages. The vertical gray lines highlight the maximum  $z$ -values indicating the formation of inner-sphere and outer-sphere adsorption complexes.

complexes increases with increasing surface coverage. For instance, a total of 0.125, 0.55, and 0.75 adsorption complexes per  $A_{uc}$ , approximately half of them being inner-sphere ones, were observed at coverages of  $0.25 C_{16}\text{TMA}^+ / A_{uc}$ ,  $0.75 C_{16}\text{TMA}^+ / A_{uc}$ , and  $1 C_{16}\text{TMA}^+ / A_{uc}$  (see figure 4.6). For the bilayer arrangements, the amount of adsorbed  $C_n\text{TMA}^+$  is significantly smaller, and no distinct dependence on the surface coverage could be observed. For instance, for  $C_{16}\text{TMA}^+$ , approximately 0.25 adsorption complexes per  $A_{uc}$  were observed at all simulated coverages of  $0.5 C_{16}\text{TMA}^+ / A_{uc}$  to  $1.5 C_{16}\text{TMA}^+ / A_{uc}$ . Maximum values of 0.75 and 0.5  $C_n\text{TMA}^+$  adsorption complexes per  $A_{uc}$  were observed for the simulated monolayer and bilayer arrangements, respectively. These amounts of adsorbed  $C_n\text{TMA}^+$  are smaller than required to compensate the negative charge of the muscovite surface. In all simulated systems, a fraction of the  $C_n\text{TMA}^+$  ions was detached from the muscovite surface. This observation agrees with the results of a preceding simulation study by Meleshyn on the adsorption of  $\text{HDPy}^+$  on muscovite mica [29].

### 4.3 Positions of the Inorganic Ions

Even at simulated surfactant coverages exceeding  $1 C_n\text{TMA}^+ / A_{\text{uc}}$ , which equals the amount of  $C_n\text{TMA}^+$  that is required to compensate the negative charge of the muscovite surface, a fraction of the potassium ions remains adsorbed on the muscovite surface (see figure 4.7). For the monolayer arrangement at a coverage of  $1 C_n\text{TMA}^+ / A_{\text{uc}}$ , only half of the potassium ions are desorbed from muscovite. For bilayer arrangements, the fractions of desorbed potassium are even smaller and decrease with increasing alkyl chain length. The amounts of desorbed potassium do not exceed  $0.125 K^+ / A_{\text{uc}}$ ,  $0.25 K^+ / A_{\text{uc}}$ , and  $0.375 K^+ / A_{\text{uc}}$  for systems with  $C_{16}\text{TMA}^+$ ,  $C_{12}\text{TMA}^+$ , and  $C_8\text{TMA}^+$  bilayer aggregates, respectively (see figure 4.7).

The potassium ions that remain adsorbed on the surface form inner-sphere complexes above either Al-substitutions, which are the preferred adsorption position in the case of unmodified muscovite [33], or above ditrigonal cavity centers. For the monolayer arrangement at a coverage of  $1 C_{16}\text{TMA}^+ / A_{\text{uc}}$ , an amount of  $0.5 K^+ / A_{\text{uc}}$  is adsorbed above both tetrahedral substitutions at  $(x, y) \sim (3 \text{ \AA}, 11.5 \text{ \AA})$  and  $(13 \text{ \AA}, 2.5 \text{ \AA})$  and ditrigonal cavity centers at  $(x, y) \sim (0 \text{ \AA}, 1 \text{ \AA})$  and  $(10.5 \text{ \AA}, 10 \text{ \AA})$  (see figure 4.5).

The vast majority of the chloride ions are located in the vicinity of  $C_n\text{TMA}^+$  headgroups (cf. the  $z$ -values of headgroup carbon atoms and chloride in figures 4.1 and 4.8). For the bilayer arrangements, approximately half of the chloride ions are located around the headgroups of the outer layers of the aggregates. They form contact and solvent-separated ion pairs with  $C_n\text{TMA}^+$  headgroups as well as with potassium ions that are adsorbed on or desorbed from the muscovite surface. Particularly for the simulated bilayer arrangements, the vertical regions that are occupied by hydrophobic alkyl chains are characterized by small densities of inorganic ions.

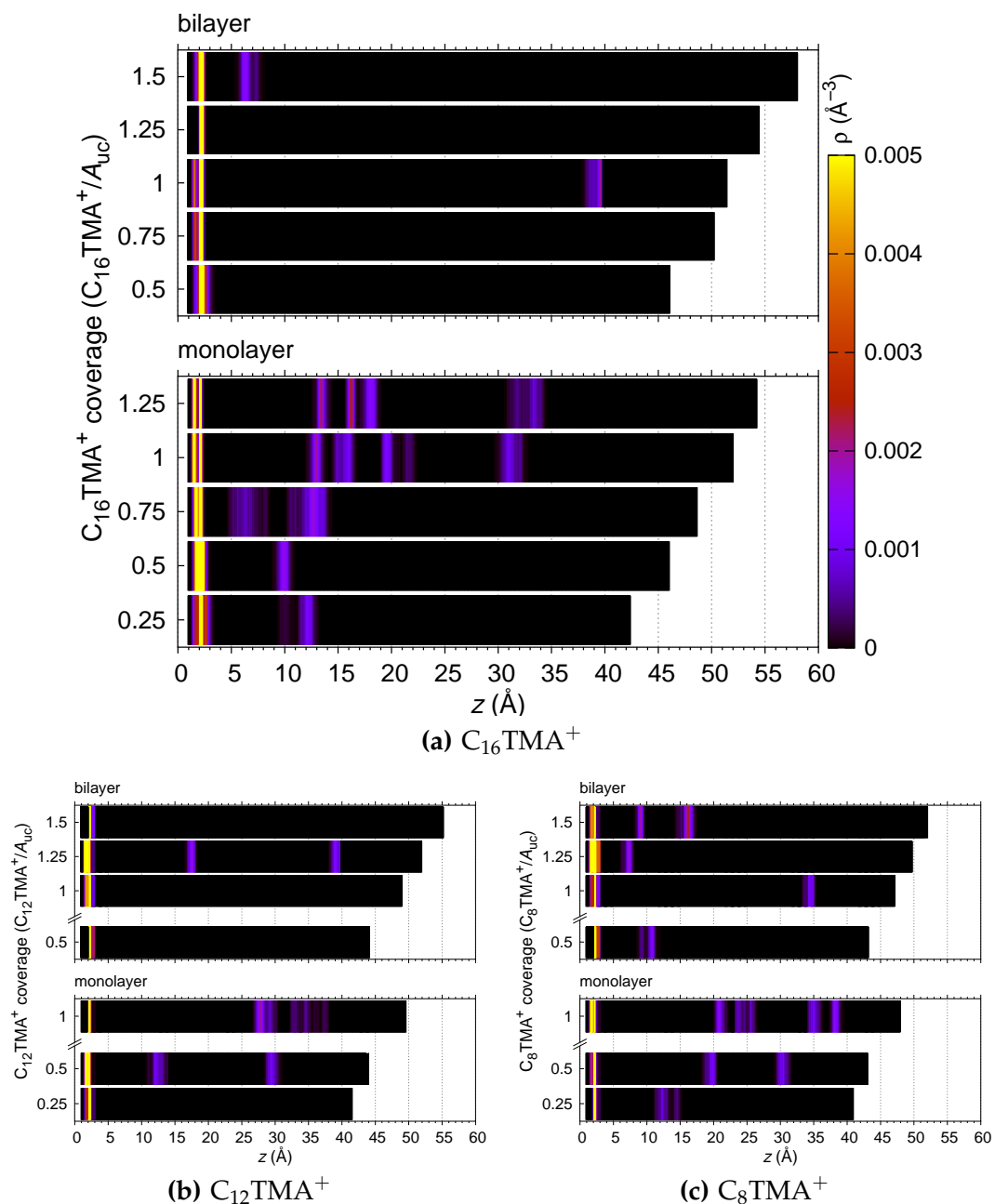


**Figure 4.7** – Vertical atomic density profiles for potassium in (a)  $C_{16}TMA^+$ , (b)  $C_{12}TMA^+$ , and (c)  $C_8TMA^+$  systems as functions of the distance  $z$  from the muscovite surface. Coverages ranging from  $0.25 C_nTMA^+/A_{uc}$  to  $1.25 C_nTMA^+/A_{uc}$  and from  $0.5 C_nTMA^+/A_{uc}$  to  $1.5 C_nTMA^+/A_{uc}$  are shown for monolayer and bilayer arrangements, respectively. For each simulated system, the extension of the water film between the muscovite–water interface ( $z = 0 \text{ \AA}$ ) and the water–vacuum interface is indicated by a black bar.

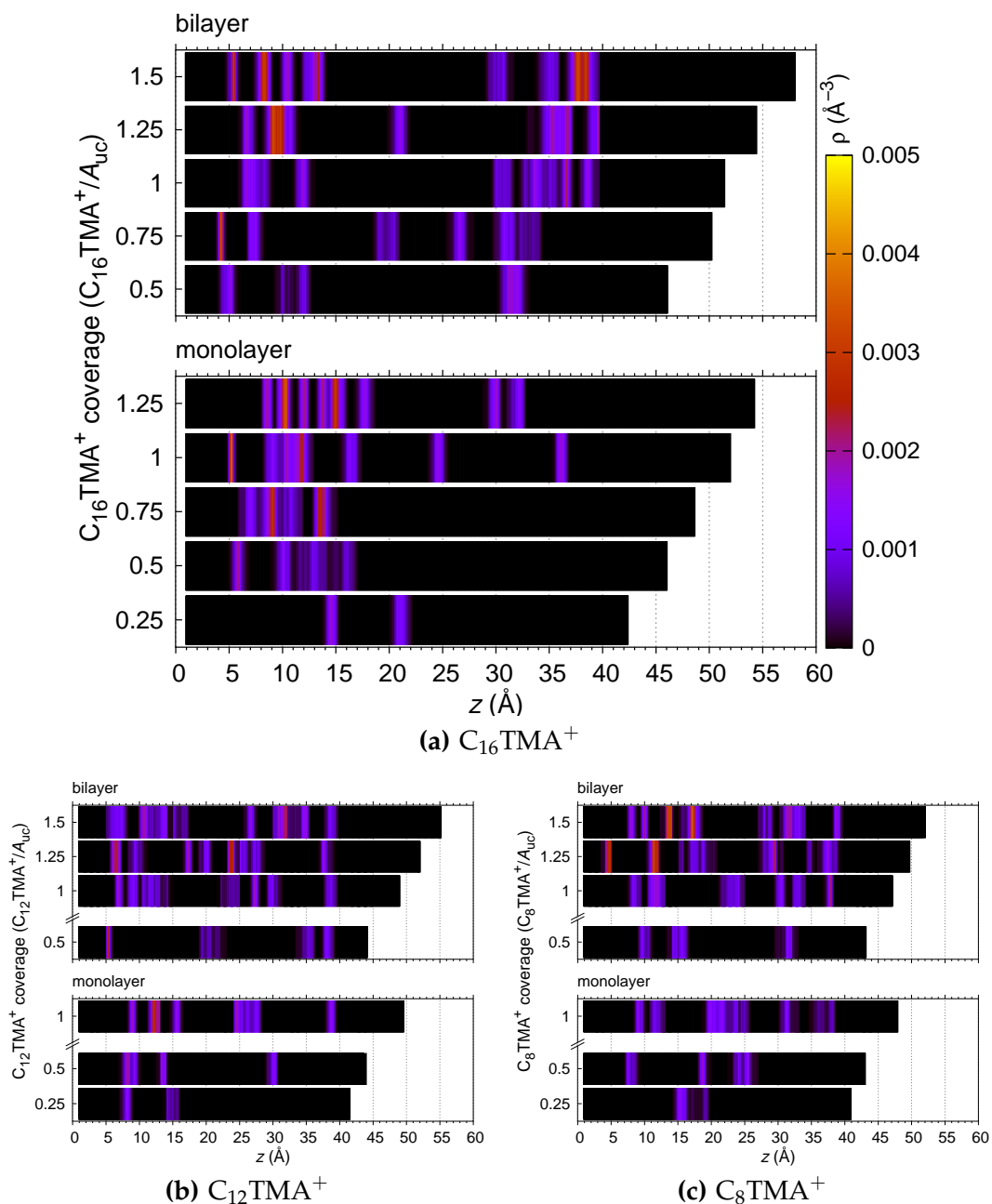


**Figure 4.8** – Vertical atomic density profiles for chloride in (a)  $C_{16}\text{TMA}^+$ , (b)  $C_{12}\text{TMA}^+$ , and (c)  $C_8\text{TMA}^+$  systems as functions of the distance  $z$  from the muscovite surface. Coverages ranging from  $0.25 C_n\text{TMA}^+ / A_{uc}$  to  $1.25 C_n\text{TMA}^+ / A_{uc}$  and from  $0.5 C_n\text{TMA}^+ / A_{uc}$  to  $1.5 C_n\text{TMA}^+ / A_{uc}$  are shown for monolayer and bilayer arrangements, respectively. For each simulated system, the extension of the water film between the muscovite–water interface ( $z = 0 \text{ \AA}$ ) and the water–vacuum interface is indicated by a black bar.

## 4.4 Structure of the Water Film

The presence of  $C_n\text{TMACl}$  changes the structure of the water film that is adsorbed on the muscovite surface. At a coverage of  $1 C_{16}\text{TMA}^+ / A_{\text{uc}}$ , the water density decreases by up to approximately 45% for the bilayer arrangement and by approximately 60% for the monolayer arrangement in the interfacial regions limited to  $z \in [7 \text{ \AA}, 35 \text{ \AA}]$  and  $z \in [7 \text{ \AA}, 30 \text{ \AA}]$ , respectively (see figure 4.9). The larger percentage decrease of the water density for the monolayer arrangement is consistent with the smaller vertical extension of the depleted region. In the simulated  $C_{12}\text{TMA}^+$  and  $C_8\text{TMA}^+$  systems, similar decreases were observed, which, however, are limited to smaller interfacial regions due to the shorter alkyl chains of the surfactant ions.

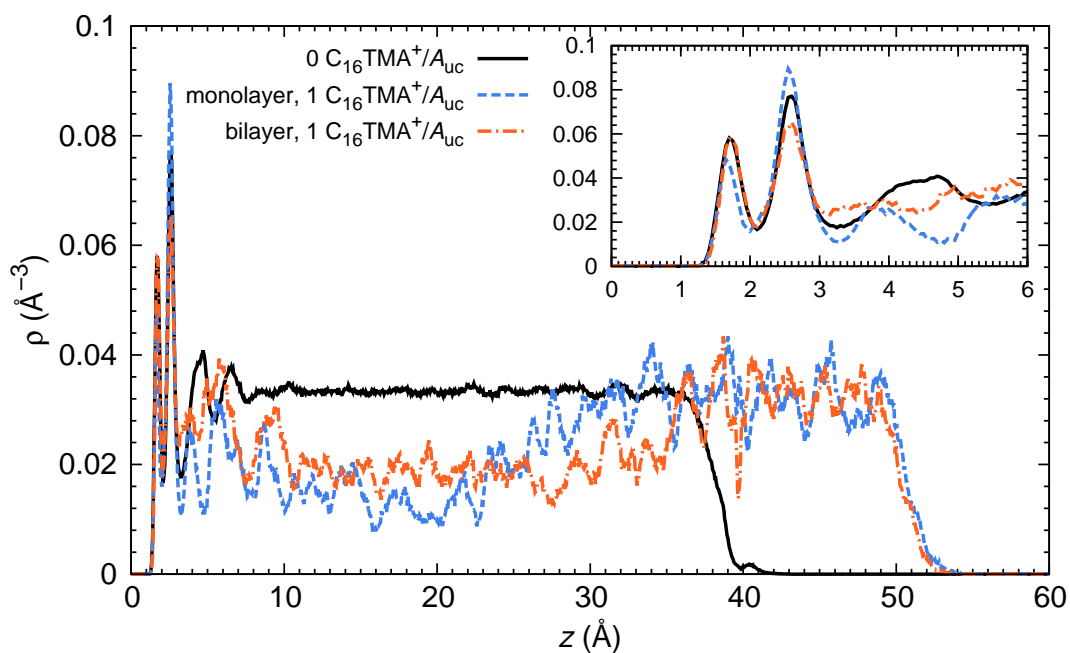


**Figure 4.9** – Vertical atomic density profiles for water oxygen as functions of the distance  $z$  from the muscovite surface for monolayer and bilayer arrangements at coverages of 0 and  $1 C_{16}\text{TMA}^+ / A_{\text{uc}}$ . Regard that the first two maxima of the water oxygen density profiles are due to sublayers of water molecules that are doubly and singly hydrogen-bonded to the muscovite surface.

Although the ratio between the numbers of water molecules that are doubly ( $z_{\text{oxygen}} \leq 2.2 \text{ \AA}$ ) and singly ( $2.2 \leq z_{\text{oxygen}} \leq 3.3 \text{ \AA}$ ) hydrogen bonded to the muscovite surface changes with increasing  $C_n\text{TMA}^+$  surface coverage, the average number of approximately 3.4 water molecules per  $A_{\text{uc}}$  that are either doubly or singly hydrogen-bonded to the muscovite surface is maintained (see inset in figure 4.9). This observation is in accordance with a preceding simulation study by Meleshyn of the adsorption of  $\text{HDPy}^+$  ions on muscovite [29]. At all simulated coverages, water molecules remain between the hydrophilic headgroups and in the regions of the hydrophobic alkyl chains. This is consistent with the findings of SFA studies by Chen et al. of the self-assembly of  $C_{16}\text{TMA}^+$  on mica [53, 129].

The displacement of water from the regions occupied by  $C_n\text{TMA}^+$  ions leads to an increase of the thickness of the water film with increasing  $C_n\text{TMA}^+$  coverage (see figure 4.10). For example, the thickness of the water film increases from approximately 38  $\text{\AA}$  for the unmodified muscovite to approximately 51  $\text{\AA}$  and 57  $\text{\AA}$  for the

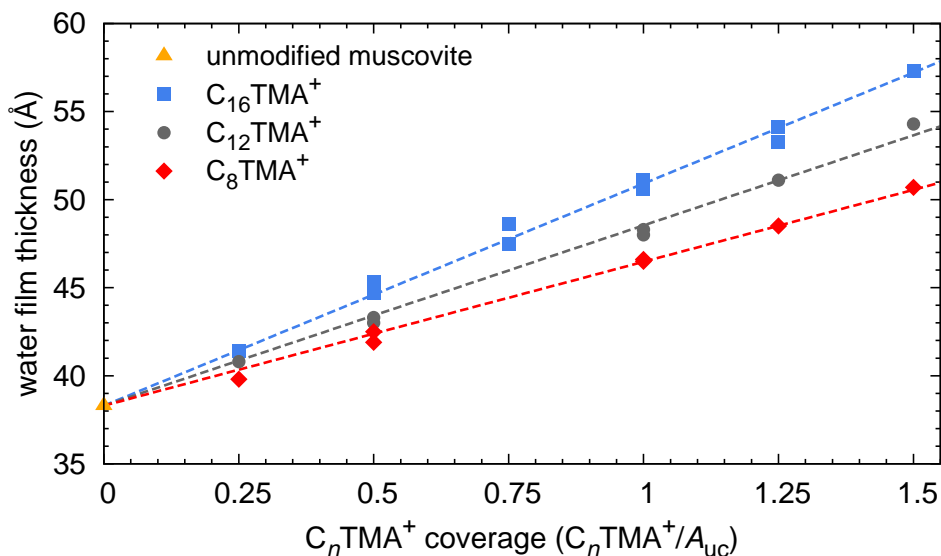


**Figure 4.10** – Water film thicknesses as functions of the  $C_n\text{TMA}^+$  coverage for  $n \in \{8, 12, 16\}$ . The slopes of the regression lines represent the increases of the water film thickness occurring upon the addition of  $1 C_n\text{TMA}^+/A_{\text{uc}}$ .

modified muscovite at coverages of 1 and 1.5  $C_{16}TMA^+ / A_{uc}$ , respectively. The increase of the water film thickness does not depend on the aggregate type (monolayer or bilayer) and is directly proportional to surface coverage with  $C_nTMA^+$  ions (see figures 4.9 and 4.10). This observation allows a calculation of the solvent volumes displaced by  $C_nTMA^+$ ,  $n \in \{8, 12, 16\}$ , at the muscovite–water interface:

For each system, the value  $z_0$ , after which the water oxygen density at the water–vacuum interface falls below the average density on unmodified muscovite ( $\rho_{bulk} = 0.033 \text{ \AA}^{-3}$ , see section 3.4), was determined. To correct for vapor-phase water molecules with  $z > z_0$  corresponding to approximately 2% – 8% of all water molecules, the thickness  $z_{corr}$  of a water film containing the respective number of water molecules at the density  $\rho_{bulk}$  was added:

$$z_{water} = z_0 + z_{corr}. \quad (4.1)$$

Because the increase of the water film thickness is directly proportional to the surface coverage with  $C_nTMA^+$  ions, the  $z_{water}$ -values were fitted by linear regression for each considered chain length  $n$  (see figure 4.10). The  $z$ -axis intercepts corresponding to coverages of 0  $C_nTMA^+ / A_{uc}$  were fixed to 38.3  $\text{\AA}$ , the thickness of the water film on the unmodified muscovite. The slopes of the regression lines (see table 4.1, second column) represent the increase of the water film thickness occurring upon the addition of 1  $C_nTMA^+ / A_{uc}$ . Multiplying these values with the area of a unit cell

**Table 4.1** – Calculated volumes displaced per  $C_nTMA^+$ , methyl(ene) or headgroup.

	Slope of the regression line ( $\text{\AA} / (C_nTMA^+ / A_{uc})$ )	Displaced volume ( $\text{\AA}^3$ )
$C_{16}TMA^+$	$12.610 \pm 0.156$	$589.2 \pm 7.3$
$C_{12}TMA^+$	$10.236 \pm 0.164$	$478.3 \pm 7.7$
$C_8TMA^+$	$8.172 \pm 0.131$	$381.8 \pm 6.1$
$CH_2/CH_3$		$25.9 \pm 1.0$
$N(CH_3)_3Cl$		$172 \pm 13$

( $A_{uc} = 46.72 \text{ \AA}$ ) yields the solvent volumes displaced per  $C_n\text{TMACl}$  (see table 4.1, third column).

In the next step, the water volumes displaced per methyl(ene) or headgroup of  $C_n\text{TMACl}$  were calculated. The volume displaced per  $C_n\text{TMACl}$  can be expressed by the following equation:

$$V = V_{\text{CH}_2} (n - 1) + V_{\text{CH}_3} + V_{\text{C}_3\text{H}_9\text{NCl}}, \quad (4.2)$$

with  $V_{\text{C}_3\text{H}_9\text{NCl}}$  denoting the volume displaced by the headgroup of the  $C_n\text{TMA}^+$  ion and the  $\text{Cl}^-$  counterion,  $V_{\text{CH}_2}$  denoting the volume displaced per methylene, and  $V_{\text{CH}_3}$  denoting the volume displaced per methyl group. Under the assumption that the volume displaced by methyl is comparable to that displaced by methylene, equation (4.2) merges to the following linear function for  $V$  in dependence on  $n$ :

$$V = V_{\text{CH}_2} n + V_{\text{C}_3\text{H}_9\text{NCl}}. \quad (4.3)$$

The three pairs  $(n, V(n))$ ,  $n \in \{8, 12, 16\}$ , were fitted by linear regression (see figure 4.11). The estimators for the slope and the  $V$ -axis intercept of the regression

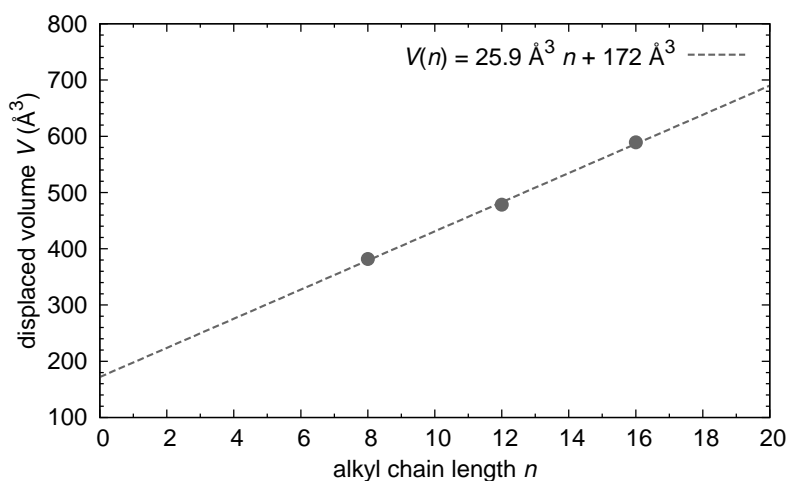


**Figure 4.11** – Relation between the alkyl chain length  $n$  and the volume  $V$  displaced per  $C_n\text{TMA}^+$  ion. The slope of the regression line represents the volume displaced per methyl(ene) group, the  $V$ -axis intercept represents the volume displaced per headgroup ( $\text{C}_3\text{H}_9\text{NCl}$ ).



line are  $V_{\text{CH}_2} = 25.9 \text{ \AA}^3 \pm 1.0 \text{ \AA}^3$  and  $V_{\text{C}_3\text{H}_9\text{NCl}} = 172 \text{ \AA}^3 \pm 13 \text{ \AA}^3$ . The differences between the volumes calculated based on equation (4.3) using the estimators for  $V_{\text{CH}_2}$  and  $V_{\text{C}_3\text{H}_9\text{NCl}}$  and the ones determined initially (see table 4.1, third column) are less than one percent and are within the ranges of the standard deviations of the latter.

## 4.5 Structure and Thickness of the Adsorbed Aggregates

Further analysis of the aggregate structures shows that up to simulated coverages of  $0.5 C_n\text{TMA}^+ / A_{\text{uc}}$ , the surfactant ions reside on the muscovite surface as monomers or dimers (see figure 4.12(a)). At higher coverages, patches of  $C_n\text{TMA}^+$  aggregates form, which cover only parts of the muscovite surface and are laterally separated

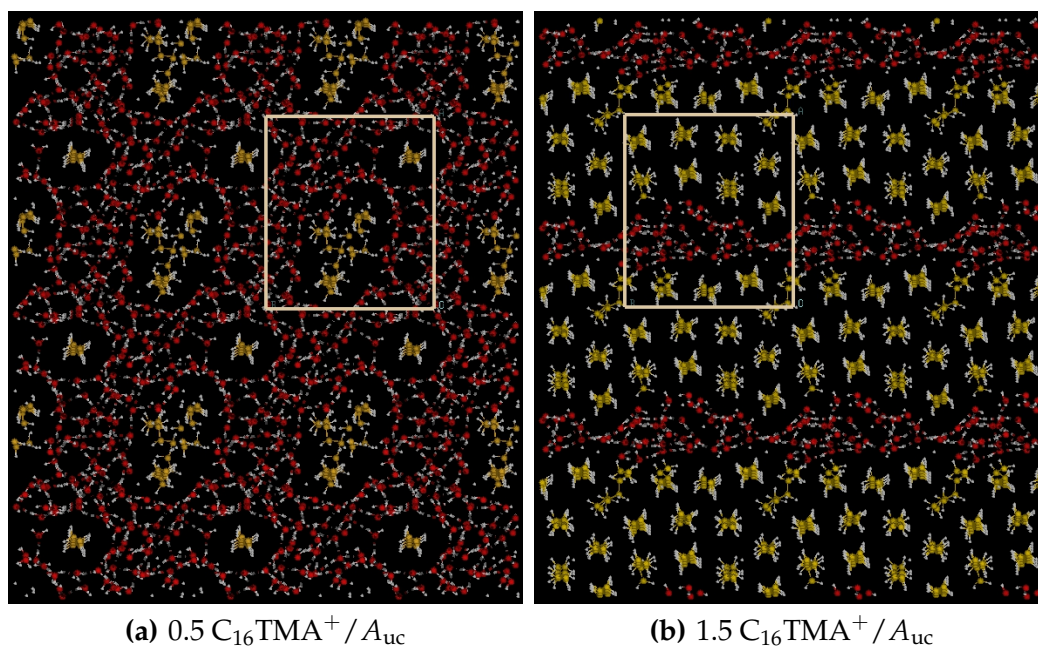


**Figure 4.12** – Snapshots of the simulated interfacial equilibrium structures in the regions  $15 \text{ \AA} < z < 26 \text{ \AA}$  for the  $C_{16}\text{TMA}^+$  bilayer arrangements at the coverages of (a)  $0.5 C_{16}\text{TMA}^+ / A_{\text{uc}}$  and (b)  $1.5 C_{16}\text{TMA}^+ / A_{\text{uc}}$ , viewed normal to the muscovite surface. Ball and stick colors: yellow (C), white (H), red (O). The fawn rectangles indicate the lateral extensions of the simulation cells.

from water at all simulated  $C_n\text{TMA}^+$  coverages (see figure 4.12(b)). Albeit on a different scale,<sup>3</sup> these patchy aggregate structures compare well to the experimental AFM observations of island-like  $C_{18}\text{TMA}^+$  aggregate growth on mica below the critical micelle concentration [78, 79].

The simulation results indicate that the area occupied per headgroup of the aggregated  $C_n\text{TMA}^+$  ions is smaller than the area of a unit cell of muscovite. At a monolayer coverage of  $1 C_n\text{TMA}^+/A_{\text{uc}}$ , approximately half of the inorganic muscovite cations ( $0.5 K^+/A_{\text{uc}}$  for the  $C_{16}\text{TMA}^+$  systems,  $0.625 K^+/A_{\text{uc}}$  for the  $C_{12}\text{TMA}^+$  systems, and  $0.5 K^+/A_{\text{uc}}$  for the  $C_8\text{TMA}^+$  systems) remain adsorbed on the muscovite surface in the regions devoid of organic aggregates. This observation is in agreement with the results of an AFM study by Fujii et al. estimating the surface area occupied by a  $C_n\text{TMA}^+$  ion to equal approximately half of the area of a unit cell ( $23 \text{ \AA}^2 - 24 \text{ \AA}^2$ ) [133].

For the bilayer aggregates of  $C_{16}\text{TMA}^+$  and  $C_{12}\text{TMA}^+$  ions, which remain as well incomplete at all simulated coverages, a pronounced interdigitation of the two layers composing them was observed (see figures 3.4 and 4.13(a)). On the contrary, for the short-chained  $C_8\text{TMA}^+$ , approximately half of the surfactant ions are characterized by large separations from the surface and do not participate in the aggregation at all simulated coverages. This is an indication of the comparatively weak interactions between the short hydrophobic alkyl chains of the  $C_8\text{TMA}^+$  ions. As a result, incomplete  $C_8\text{TMA}^+$  monolayer type aggregates with single headgroups facing the aggregate–solution interface are formed instead of bilayer aggregates (see figure 4.13(b)).

The apparent aggregate thicknesses, which describe the extensions of the surfactant aggregates in the  $z$ -direction, were estimated on the basis of the vertical atomic density profiles for the carbon atoms of alkyl chains (monolayer aggregates) and headgroups (bilayer aggregates) of the  $C_n\text{TMA}^+$  ions (see figure 4.1). The

---

<sup>3</sup>The island-like structures observed in the experiments exhibited diameters of some hundreds of nanometers, which cannot be represented by the simulation cells of this study having lateral extensions of only approximately 2 nm (cf. subsection 3.2.5).

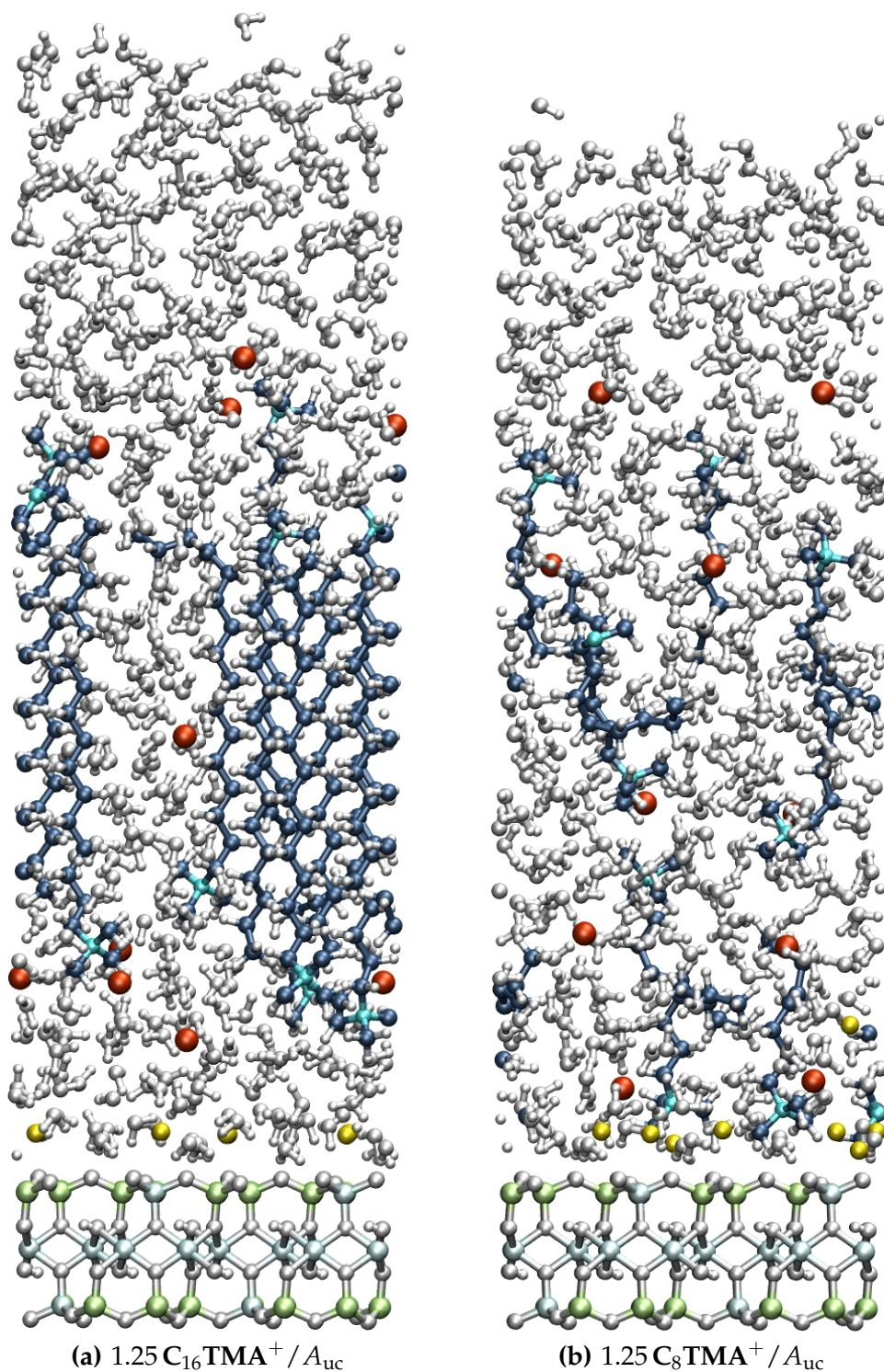


**Figure 4.13** – Snapshots of the simulated equilibrium configurations for the (a)  $\text{C}_{16}\text{TMA}^+$  and (b)  $\text{C}_8\text{TMA}^+$  bilayer arrangements at coverages of  $1.25 \text{ C}_n\text{TMA}^+ / A_{\text{uc}}$ , viewed parallel to the muscovite–water interface. Ball and stick colors: yellow ( $\text{K}^+$ ), light blue (Al), light green (Si), reddish gray (O), white (H), turquoise (N), dark blue (C), red ( $\text{Cl}^-$ ).

estimated thicknesses of the bilayer aggregates equal 30 Å – 35 Å for  $C_{12}\text{TMA}^+$  and 35 Å – 39 Å for  $C_{16}\text{TMA}^+$ . The thicknesses of the monolayer aggregates are in the ranges of approximately 18 Å for  $C_8\text{TMA}^+$ , 22 Å – 27 Å for  $C_{12}\text{TMA}^+$ , and 31 Å – 35 Å for  $C_{16}\text{TMA}^+$ .

Noteworthy, the thicknesses of the simulated  $C_{16}\text{TMA}^+$  monolayer aggregates are significantly larger than those of 15 Å to 18 Å determined by SFA by Israelachvili et al. and Kékicheff et al. [118, 119], being even smaller than the length of a fully extended  $C_{16}\text{TMA}^+$  ion ( $\sim 23.5$  Å). This difference can be understood considering that in the SFA, two distant mica surfaces with  $C_{16}\text{TMA}^+$  monolayer aggregates adsorbed on each of them are brought into contact. Afterwards, the thickness of the adsorbed aggregates is derived by halving the measured separation of 30 Å to 36 Å of the two surfaces.

However, this approach does not take into account that the hydrophobic alkyl chains of the surfactant ions adsorbed on the opposing surfaces interact during the measurement. After a complete exchange of the interfacial potassium ions by  $C_n\text{TMA}^+$  ions, the available surface area per  $C_n\text{TMA}^+$  headgroup is approximately 47 Å<sup>2</sup>, which is more than twice the cross-sectional area of approximately 20 Å<sup>2</sup> of hydrocarbon chains [134]. Thus, upon the approach of the two opposing mica surfaces, a close packing of the interacting hydrophobic alkyl chains can be assumed to occur and lead to the formation of interdigitated bilayer aggregates confined between the two mica surfaces. Indeed, the measured separations of the mica surfaces of 30 Å to 36 Å are comparable to the simulated thicknesses of the interdigitated  $C_{16}\text{TMA}^+$  bilayer aggregates formed on the cleaved muscovite surface ranging from 35 Å to 39 Å. For similar reasons, the thicknesses of  $C_n\text{TMA}^+$  aggregates intercalated between delaminated mica sheets [135] or into the interlayer spaces of vermiculites, which exhibit surface charge densities that are comparable to that of muscovite mica [136, 137], are significantly smaller than those of the unconstrained aggregates formed on the external surfaces of muscovite.

In contrast to SFA experiments, measuring aggregate thickness by AFM in soft-contact mode is a method that is comparable to the consideration of the cleaved

muscovite–water interface in this study. Indeed, with this method, thickness ranges between 30 Å and 45 Å, which agree well with the simulated ones, were measured for  $C_{16}TMA^+$  bilayer aggregates [122–124]. Unfortunately, no similar comparison can be made for monolayer aggregates, as aggregate headgroups facing the solution are required to exert a repulsive force on the AFM tip.

The degree of conformational order within the surfactant aggregates was analyzed with the help of the calculated gauche conformation fractions of the alkyl chains (see figure 4.14). With a maximum of 0.46, the short-chained  $C_8TMA^+$  ions show by far the highest values. The maximum observed fractions of gauche conformations within the simulated  $C_{12}TMA^+$  and  $C_{16}TMA^+$  aggregates amount to 0.19 and 0.12, respectively. This increasing degree of conformational order with

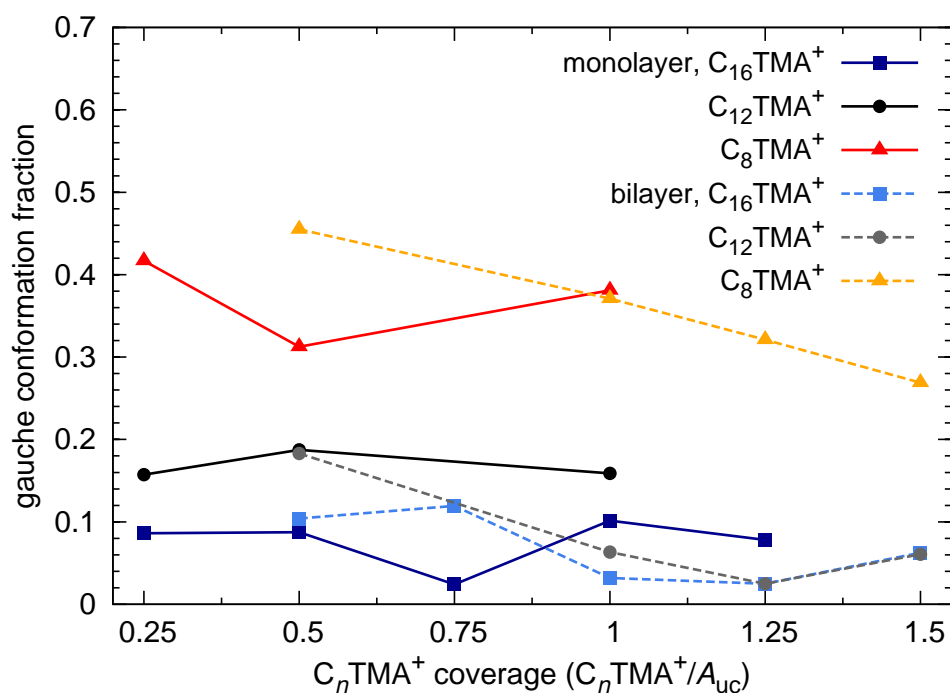


**Figure 4.14** – Fractions of gauche conformations of the alkyl chains for monolayer and bilayer arrangements as functions of the  $C_nTMA^+$  coverage,  $n \in \{8, 12, 16\}$ . Torsion angles of  $60^\circ \pm 60^\circ$  and  $300^\circ \pm 60^\circ$  were counted as gauche conformations. Lines were added as guides to the eye.

increasing alkyl chain length can be attributed to the increased hydrophobic interactions between the longer surfactant alkyl chains. The observations agree with *fourier transform infrared spectroscopy* (FTIR), *nuclear magnetic resonance spectroscopy* (NMR) and NEXAFS experiments of the self-assembly of dialkylammonium surfactants on mica [127, 128]. Furthermore, in agreement with IR measurements performed during the growth of  $C_{18}\text{TMA}^+$  aggregates [78, 79], a slight decrease of the calculated gauche conformation fractions with increasing surface coverage was observed for all studied chain lengths. This decrease might reflect a closer packing of the alkyl chains due to spatial limitations. No significant distinction could be observed between the conformational order of the alkyl chains within the simulated monolayer and bilayer aggregates. The calculated gauche conformation fractions exhibit comparatively high standard deviations of up to approximately 0.18, which manifest the coexistence of nearly fully extended chains and chains with high numbers of gauche conformations in the same systems. In comparison with the respective distances of surfactant ions with completely extended alkyl chains, the averaged end-to-end distances decrease by 5 % to 13 % for the aggregated  $C_{16}\text{TMA}^+$  ions and by 4 % to 21 % and 14 % to 23 % for the aggregated  $C_{12}\text{TMA}^+$  and  $C_8\text{TMA}^+$  ions, respectively.

The simulation results suggest a model of  $C_{16}\text{TMA}^+$  and  $C_{12}\text{TMA}^+$  bilayer aggregates consisting of two opposed monolayers with highly interdigitated alkyl chains, which exhibit a low fraction of gauche conformations. This model agrees well with those developed from *X-ray photoelectron spectroscopy* (XPS) and NR studies [53, 130] and explains the small differences of only a few angstroms between the thicknesses of the monolayer and bilayer aggregates.

## 4.6 Discussion on the Transferability of the Simulation

### Results to Real Systems

A thorough consideration should be given to the significantly lower fraction of adsorption complexes formed by the  $C_n\text{TMA}^+$  ions in the simulated bilayer systems as compared to the monolayer ones (see section 4.2). Simultaneously, the

potassium ions remain largely adsorbed on the muscovite surface in the bilayer systems ( $\geq 0.875 K^+ / A_{uc}$ ), and up to half of the chloride ions are located close to the surfactant headgroups facing the muscovite surface (see section 4.3).

A similar accumulation of inorganic ions at the mineral-aggregate interface was observed in experiments by Chen et al. [53]. The authors concluded that during the self-assembly of  $C_{16}TMA^+$  aggregates, a rapidly occurring initial adsorption phase is followed by an equilibration phase, which proceeds unexpectedly slowly at those surfactant concentrations leading to the formation of bilayer aggregates. During the initial phase, the  $C_{16}TMA^+$  ions adsorb on the muscovite surface accompanied by their counterions. During the second phase, organic cations can only displace potassium ions trapped between the bilayer aggregates and the mica surface in a slowly proceeding two-step process:

- (i) formation of inorganic ion pairs of potassium with counterions (as a rule,  $Cl^-$  or  $Br^-$ ) introduced into the system with the  $C_{16}TMA^+$  ions, and
- (ii) diffusion of these ion pairs through the hydrophobic regions of the bilayer aggregates.

This release of interfacial cations from the surface region eventually results in an increasingly stronger binding of the  $C_{16}TMA^+$  ions to the muscovite surface. Up to several weeks were reported to be necessary to accomplish this slowly proceeding second step of the adsorption process for experimental setups leading to the formation of  $C_{16}TMA^+$  bilayer aggregates. On the contrary, only one hour was needed for the equilibration of those setups leading to the formation of monolayer aggregates [53]. In terms of the simulated systems, to leave the muscovite surface, trapped potassium ions have to

- (i) overcome the Coulomb repulsion barrier of the  $C_nTMA^+$  headgroups that face the muscovite surface,
- (ii) diffuse through the hydrophobic regions of the bilayer aggregates, which become thicker with increasing alkyl chain length, and

- (iii) overcome a second Coulomb repulsion barrier of the  $C_n\text{TMA}^+$  head-groups that face the aggregate–solution interface.

Correspondingly, the fraction of desorbed potassium in the simulated bilayer systems decreases with increasing chain length. The determined values do not exceed  $0.375 K^+ / A_{uc}$  for the simulated  $C_8\text{TMA}^+$  bilayer systems and  $0.25 K^+ / A_{uc}$  and  $0.125 K^+ / A_{uc}$  for the simulated  $C_{12}\text{TMA}^+$  and  $C_{16}\text{TMA}^+$  systems, respectively. Particularly at high simulated  $C_{16}\text{TMA}^+$  surface coverages, the energy barriers appear too high to be overcome in reasonable computation times with the applied simulation method. The desorption of potassium ions from the muscovite surface and accordingly the achievement of the equilibrium state observed in experiments after times of hours up to several weeks [53, 122, 123] are impeded.

Therefore, the simulated structures rather correspond to the aggregate structures observed in experiments after the first step of the above-discussed process when inorganic ions (chloride and potassium) are still present at the mineral–aggregate interface. An increased speed of equilibration of the simulated systems can possibly be obtained by further optimization of the applied simulation algorithms, for example, by the implementation of cluster moves or the allowance of tunneling of inorganic ion pairs and water through the hydrophobic bilayer aggregate regions. An increased diffusion of K–Cl ion pairs out of the bilayer aggregates will presumably lead to greater numbers of  $C_n\text{TMA}^+$  inner-sphere and outer-sphere surface complexes and consequently to slight decreases of the apparent aggregate thicknesses with time.

## 4.7 Summary of the Simulation Results

The simulation results indicate that the structure of the water film adsorbed on the muscovite surface is considerably affected by the presence of  $C_n\text{TMA}^+$  ions at the muscovite–water interface. While the water density in the alkyl chain regions of the  $C_n\text{TMA}^+$  aggregates is decreased with increasing surfactant surface coverage, the average number of approximately 3.4 water molecules per  $A_{uc}$  that



are hydrogen-bonded to the mineral surface with  $z_{\text{oxygen}} \leq 3.3 \text{ \AA}$  is retained. The volumes of water displaced per  $C_n\text{TMA}^+ - \text{Cl}^-$  ion pair were estimated to  $\sim 590 \text{ \AA}^3$  for  $C_{16}\text{TMA}^+$ ,  $\sim 480 \text{ \AA}^3$  for  $C_{12}\text{TMA}^+$ , and  $\sim 380 \text{ \AA}^3$  for  $C_8\text{TMA}^+$ . At all simulated  $C_n\text{TMA}^+$  coverages, the assembled aggregates remain laterally incomplete, and water molecules are located between the headgroups and in the hydrophobic regions of the alkyl chains for both the monolayer and the bilayer arrangements of  $C_n\text{TMA}^+$  ions. This is consistent with the findings of SFA studies of the self-assembly of  $C_{16}\text{TMA}^+$  on muscovite mica (cf. [53, 129]).

$C_n\text{TMA}^+$  ions form inner-sphere and outer-sphere adsorption complexes on the muscovite surface. Inner-sphere adsorbed  $C_n\text{TMA}^+$  ions are arranged directly above the ditrigonal cavities of the muscovite surface, the adsorption sites occupied by water molecules on unmodified muscovite. The distances between their nitrogen atoms and the muscovite surface are in the range of  $3.3 \text{ \AA}$  to  $3.8 \text{ \AA}$ . These are  $0.4 \text{ \AA}$  more than in the case of dehydrated  $C_n\text{TMA}^+$ -muscovite. The vertical and lateral positions of outer-sphere adsorbed  $C_n\text{TMA}^+$  ions are less specified with distances between the nitrogen atoms and the muscovite surface of  $5.5 \text{ \AA}$  to  $8.4 \text{ \AA}$ .  $C_n\text{TMA}^+$  ions with larger  $z$ -values are separated from the basal surface by at least two water layers and thus desorbed from muscovite. A maximum value of  $0.75 C_n\text{TMA}^+$  adsorption complexes per  $A_{\text{uc}}$  was observed.

The thicknesses of the simulated monolayer aggregates are in the ranges of  $31 \text{ \AA}$  to  $35 \text{ \AA}$  for  $C_{16}\text{TMA}^+$ ,  $22 \text{ \AA}$  to  $27 \text{ \AA}$  for  $C_{12}\text{TMA}^+$ , and approximately  $18 \text{ \AA}$  for  $C_8\text{TMA}^+$ . The  $C_{16}\text{TMA}^+$  and  $C_{12}\text{TMA}^+$  bilayer aggregates exhibit thicknesses of  $35 \text{ \AA}$  to  $39 \text{ \AA}$  and  $30 \text{ \AA}$  to  $35 \text{ \AA}$ , respectively and show a strong interdigitation of the two opposing surfactant layers composing the aggregates. On the contrary, for the short-chained  $C_8\text{TMA}^+$ , approximately half of the surfactant ions are characterized by large separations from the surface and do not participate in the aggregation at all simulated coverages. In none of the simulated  $C_8\text{TMA}^+$  systems, bilayer aggregates could be observed. The thicknesses of the simulated  $C_{16}\text{TMA}^+$  bilayer aggregates are in excellent agreement with those of  $30 \text{ \AA} - 45 \text{ \AA}$  measured by AFM in soft-contact mode at twice the critical micelle concentration (cf. [122–124]).

In agreement with previous experimental studies (cf. [127, 128]), the alkyl chains of the aggregated  $C_n\text{TMA}^+$  ions show a high conformational order that considerably decreases with decreasing alkyl chain length. The maximum observed fractions of gauche conformation within the simulated  $C_{16}\text{TMA}^+$  and  $C_{12}\text{TMA}^+$  aggregates amount to 0.12 and 0.19, respectively, whereas, for the short chained  $C_8\text{TMA}^+$ , values of up to 46 % were observed.

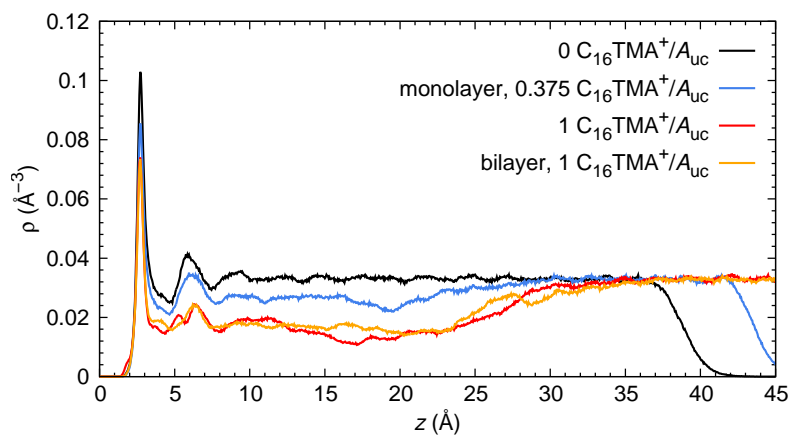
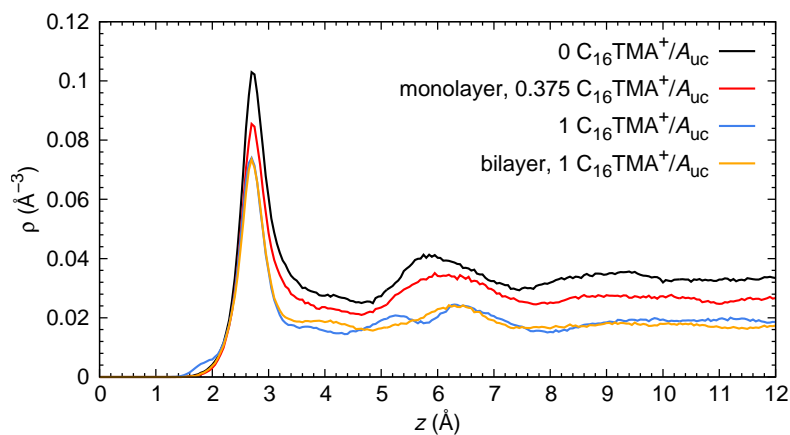
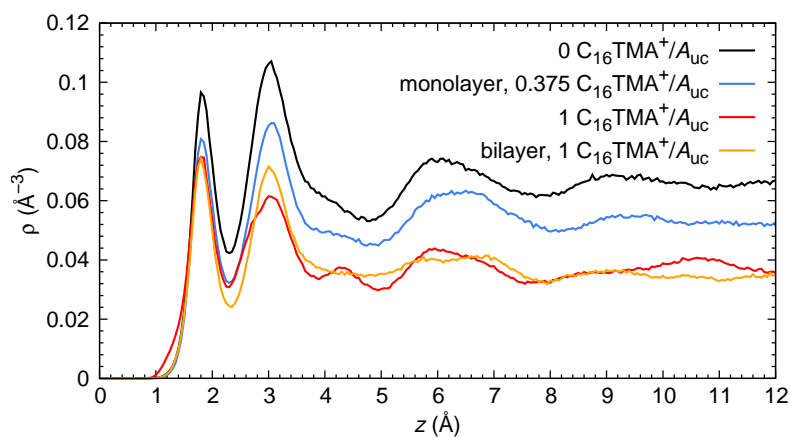
In the simulated bilayer systems, the majority of the potassium ions remain adsorbed on the muscovite surface, and up to half of the chloride ions are located in the regions occupied by the hydrophilic headgroups facing the muscovite surface. This high concentration of inorganic ions at the muscovite surface is accompanied by significantly smaller fractions of  $C_n\text{TMA}^+$  inner-sphere and outer-sphere surface complexes in the simulated bilayer systems as compared to the monolayer ones. Accordingly, this work suggests that the simulated bilayer structures represent those  $C_n\text{TMA}^+$  aggregate structures that are observed in experiments during the initial equilibration phases characterized by the presence of inorganic ions within the aggregates (cf. [53, 122, 123]).

---

## Aggregation of $C_nTMA^+$ Ions at the External Surface of Montmorillonite

### 5.1 Structure of the Water Film

The negatively charged montmorillonite surface induces a layering of the adsorbed water film, which is extended over several molecular layers. Of these layers, the first one, which has its maximum oxygen density at  $z = 2.7 \text{ \AA}$ , is particularly pronounced. The majority of the water molecules constituting this layer are oriented in such a way that one of their two hydrogen atoms points towards the montmorillonite surface and donates a hydrogen bond to one of the basal oxygen atoms (see figure 5.2(a)). Correspondingly, the hydrogen density profile exhibits two maxima at  $1.8 \text{ \AA}$  and at  $3.05 \text{ \AA}$  (see figure 5.1(c)). The first peak of the oxygen density profile and the second peak of the hydrogen density profile are notably broadened towards higher  $z$ -values. This broadening is a consequence of the location of some of the water molecules of the first water layer slightly farther away from the montmorillonite surface. These molecules are not hydrogen-bonded to the mineral surface, but donate at least one hydrogen bond to those water molecules that are singly hydrogen-bonded to the montmorillonite surface.

(a) Water oxygen,  $z \leq 45 \text{ \AA}$ (b) Water oxygen,  $z \leq 12 \text{ \AA}$ (c) Water hydrogen,  $z \leq 12 \text{ \AA}$ 

**Figure 5.1** – Vertical atomic density profiles for (a) and (b) water oxygen and (c) water hydrogen atoms as functions of the distance  $z$  from the montmorillonite surface for monolayer and bilayer arrangements at coverages of  $0 C_{16}\text{TMA}^+ / A_{uc}$ ,  $0.375 C_{16}\text{TMA}^+ / A_{uc}$ , and  $1 C_{16}\text{TMA}^+ / A_{uc}$ .

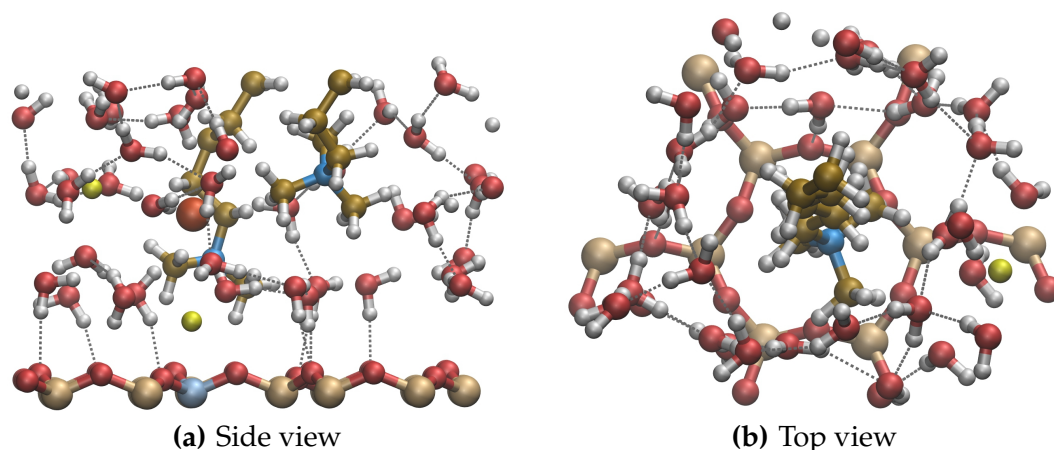


**Figure 5.2** – (a) Side view of  $C_{16}TMA^+$  ions adsorbed as inner-sphere (left ion) and outer-sphere (right ion) complexes on the montmorillonite surface for the bilayer arrangement at a coverage of  $0.75 C_{16}TMA^+ / A_{uc}$ . (b) Top view of a  $C_{16}TMA^+$  ion adsorbed as inner-sphere complex on the montmorillonite surface for the monolayer arrangement at a coverage of  $0.375 C_{16}TMA^+ / A_{uc}$ . (a) and (b) show snapshots of the simulated equilibrium configurations. Ball and stick colors: beige (Si), gray-blue (Al), red (O), white (H), blue (N), brown (C), yellow ( $Na^+$ ), red ( $Cl^-$ ).

In contrast to the water film adsorbed on muscovite (see section 3.4), the water film adsorbed on montmorillonite exhibits almost no water molecules that are doubly hydrogen-bonded to the mineral surface. The cumulative content of these water molecules with  $z_{\text{oxygen}} \leq 2.2 \text{ \AA}$  amounts to only 0.1 molecules per  $A_{uc}$  for the unmodified montmorillonite, whereas for muscovite, 1.3 water molecules per  $A_{uc}$  were observed. The absence of water molecules that are doubly hydrogen-bonded to the montmorillonite surface is also reflected by the lateral density profiles for water oxygen and hydrogen (see figure 5.3). For muscovite, the profiles show that the doubly hydrogen-bonded water molecules are adsorbed above the centers of ditrigonal cavities of the mineral surface (see, e. g., figure 5.3(b) at  $(x, y) \sim (5 \text{ \AA}, 9 \text{ \AA})$ ), whereas, for montmorillonite, no such strongly adsorbed water molecules exist (see figure 5.3(a)).

The analysis of the lateral atomic density profiles further shows that the location of the charge substitutions within the clay layer (tetrahedral or octahedral sheet)

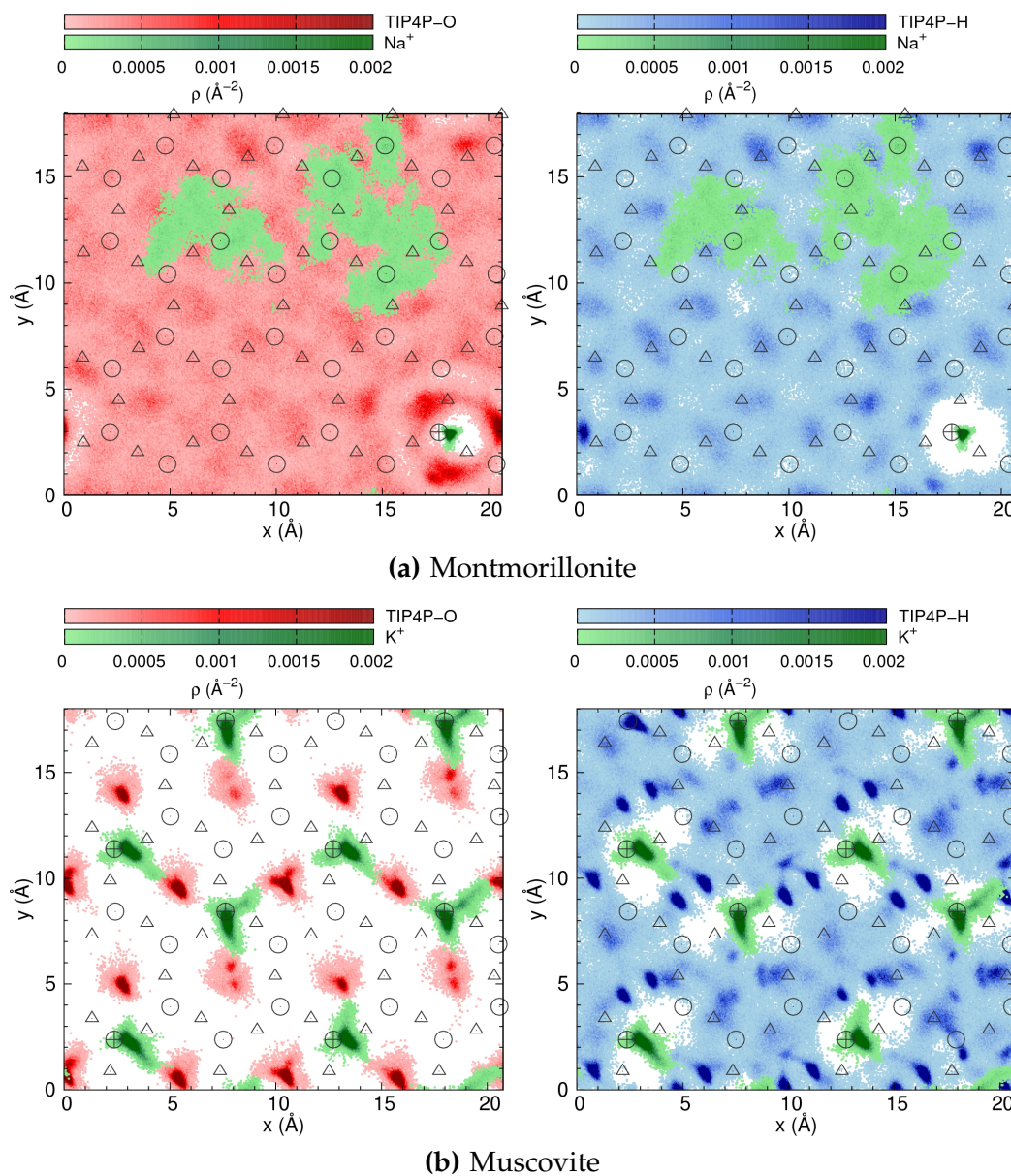


**Figure 5.3** – Lateral atomic density profiles for water and surface cations at the unmodified (a) montmorillonite-water and (b) muscovite-water interfaces. The oxygen and hydrogen densities were sampled within the first peaks of the corresponding atomic density profiles ( $z_{\text{oxygen}} < 3.6 \text{ \AA}$  and  $z_{\text{hydrogen}} < 2.3 \text{ \AA}$  for montmorillonite,  $z < 2.2 \text{ \AA}$  for muscovite for both oxygen and hydrogen atoms). The  $\text{Na}^+$  and  $\text{K}^+$  densities were sampled within  $5.5 \text{ \AA}$  from the mineral surfaces. The circles, crossed circles, and triangles represent silicon, aluminum, and basal oxygen atoms of the tetrahedral sheet at the mineral-water interfaces, respectively (cf. figures 3.1(b) and 3.2(b)).

strongly affects the structure of the interfacial water films. The water density at the montmorillonite surface is considerably increased in the regions around the tetrahedral charge substitution at  $(x, y) \sim (18 \text{ \AA}, 3 \text{ \AA})$ , and pronounced adsorption positions for three water oxygen atoms are located at  $(x, y) \sim (17 \text{ \AA}, 4 \text{ \AA})$ ,  $(18 \text{ \AA}, 1 \text{ \AA})$ , and  $(20.5 \text{ \AA}, 3 \text{ \AA})$  (see figure 5.3(a)). These water molecules belong to the hydration shell of sodium adsorbed directly above the tetrahedral charge substitution. For muscovite, the adsorption of water molecules above those ditrigonal cavities of the surface featuring more than one aluminum substitution is notably stronger (cf. figure 5.3(b) at  $(x, y) \sim (5 \text{ \AA}, 9 \text{ \AA})$  and at  $(x, y) \sim (7.5 \text{ \AA}, 5 \text{ \AA})$ ). Other than the charge substitutions of the tetrahedral sheets, charge substitutions of the octahedral sheets are located farther away from the mineral-water interface and are additionally shielded by a tetrahedral sheet. As a result, the effect of octahedral charge substitutions on the arrangement of water dipoles at the mineral surfaces and thus on the structure of adsorbed water films is significantly smaller than that of tetrahedral substitutions.

The first maximum of the density distribution of water oxygen on the montmorillonite surface is located at  $z$ -values comparable to those of the second sub-layer of water molecules adsorbed on the muscovite surface, which has its maximum oxygen density at  $z = 2.6 \text{ \AA}$  and its minimum at  $z = 3.3 \text{ \AA}$  (cf. figures 4.9 and 5.1(b)). The water layers adsorbed on both montmorillonite and muscovite contain water molecules that are singly hydrogen-bonded to the mineral surfaces with  $2.2 \text{ \AA} \leq z_{\text{oxygen}} \leq 3.3 \text{ \AA}$ . The amounts of water in these vertical regions amount to 3.0 and 2.1 molecules per  $A_{\text{uc}}$  for montmorillonite and muscovite, respectively.

Accordingly, both the type (tetrahedral or octahedral) and the density of the charge substitutions in the clay layers are parameters that determine the structure of the interfacial water films. These effects lead to a significantly stronger binding of water molecules to the muscovite surface, which exclusively exhibits tetrahedral charge substitutions and a 2.7 times greater layer charge than the modeled montmorillonite surface. The observed water layering on montmorillonite is in agreement

with previous molecular dynamics studies by Greathouse and Cygan, Marry et al., and Rotenberg et al. [68, 69, 138].

The presence of  $C_n\text{TMACl}$  at the montmorillonite–water interface changes the structure of the adsorbed water film. The relative decrease of the water density in the aggregate regions is comparable to that observed for the water film adsorbed on muscovite (see section 4.4), and at all simulated surfactant coverages, water molecules remain between the hydrophilic headgroups and in the regions of the hydrophobic alkyl chains. For the monolayer arrangement at a coverage of  $0.375 C_{16}\text{TMA}^+ / A_{\text{uc}}$ , the average water density in the interfacial region that is limited to  $z \in [8 \text{ \AA}, 23 \text{ \AA}]$  decreases by 21 %. At a coverage of  $1 C_{16}\text{TMA}^+ / A_{\text{uc}}$ , the average water density in the same region decreases by 54 % for the monolayer arrangement and by 50 % for the bilayer arrangement (cf. figure 5.1(a)). For systems containing  $C_{12}\text{TMA}^+$  and  $C_8\text{TMA}^+$  ions, similar decreases were observed. However, due to the shorter alkyl chains, the decreases of the water densities are limited to smaller interfacial regions. The volumes displaced by the  $C_{16}\text{TMA}^+ - \text{Cl}^-$  ( $597.8 \text{ \AA}^3 \pm 3.3 \text{ \AA}^3$ ),  $C_{12}\text{TMA}^+ - \text{Cl}^-$  ( $478.0 \text{ \AA}^3 \pm 3.9 \text{ \AA}^3$ ), and  $C_8\text{TMA}^+ - \text{Cl}^-$  ( $372.9 \text{ \AA}^3 \pm 3.6 \text{ \AA}^3$ ) ion pairs equal those calculated for the muscovite-water-organics systems within their standard deviations (cf. table 4.1). In contrast to the adsorption of  $C_n\text{TMA}^+$  ions on muscovite, their adsorption on montmorillonite leads to a significant decrease of the density of the first water layers in the interfacial regions limited to  $z_{\text{oxygen}} \leq 7.45 \text{ \AA}$  (see figure 5.1(b) and section 5.3).

## 5.2 Adsorption Positions of the $C_n\text{TMA}^+$ Ions

The atomic density profiles for  $C_n\text{TMA}^+$  head group carbon atoms (see figure 5.4) indicate that  $C_n\text{TMA}^+$  ions approach the montmorillonite surface to distances of approximately  $2 \text{ \AA}$ . The headgroup methyls of these inner-sphere adsorbed  $C_n\text{TMA}^+$  ions penetrate the first water layer adsorbed on the montmorillonite surface (see figure 5.2). The first maxima of the respective atomic density profiles correspond to



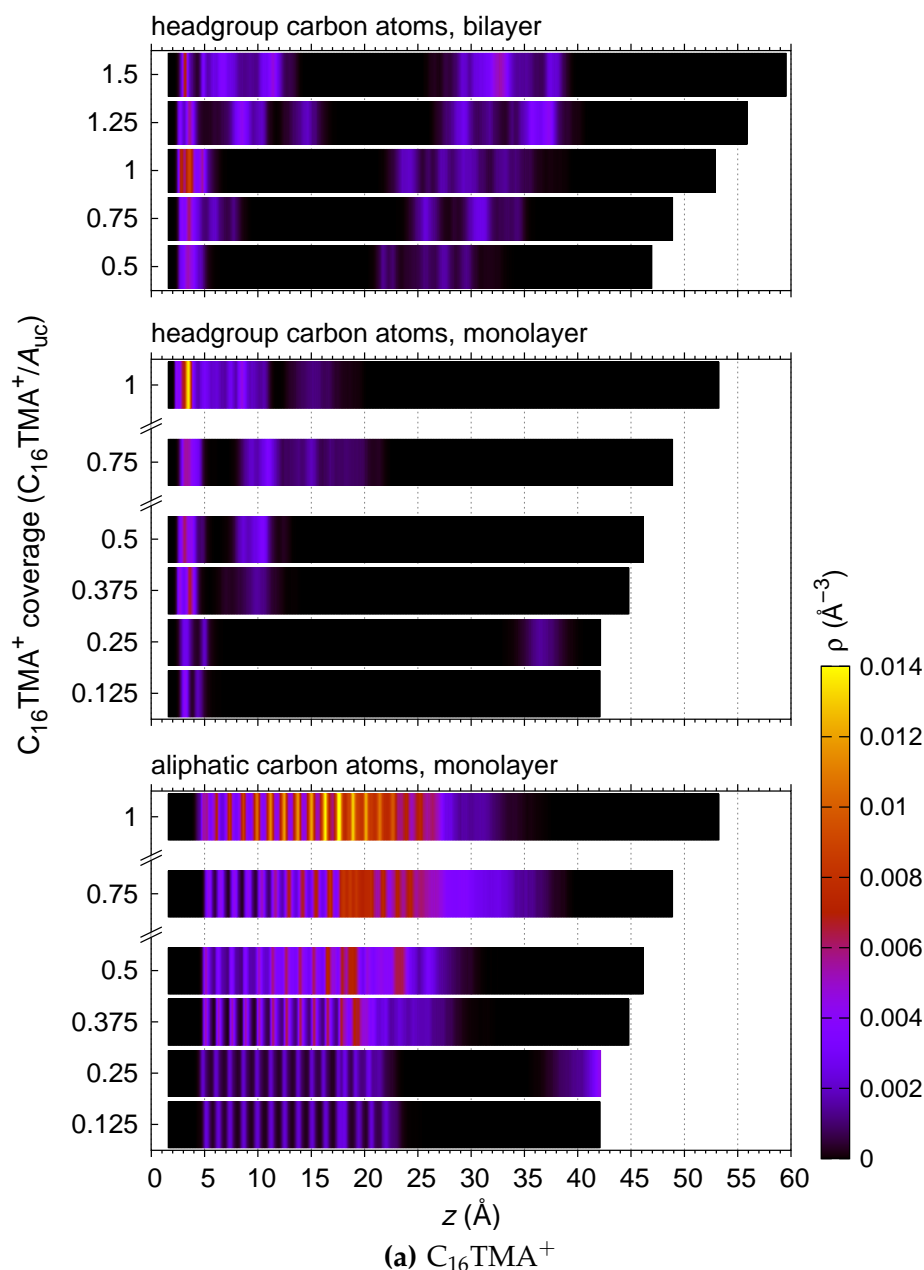


**Figure 5.4** – (a) Vertical atomic density profiles for carbon atoms of  $C_{16}\text{TMA}^+$  headgroups and alkyl chains as functions of the distance  $z$  from the montmorillonite surface. Coverages ranging from  $0.125 C_{16}\text{TMA}^+/A_{uc}$  to  $1 C_{16}\text{TMA}^+/A_{uc}$  and from  $0.5 C_{16}\text{TMA}^+/A_{uc}$  to  $1.5 C_{16}\text{TMA}^+/A_{uc}$  are shown for monolayer and bilayer arrangements, respectively. For each simulated system, the extension of the water film between the montmorillonite–water interface ( $z = 0 \text{ \AA}$ ) and the water–vacuum interface is indicated by a black bar.

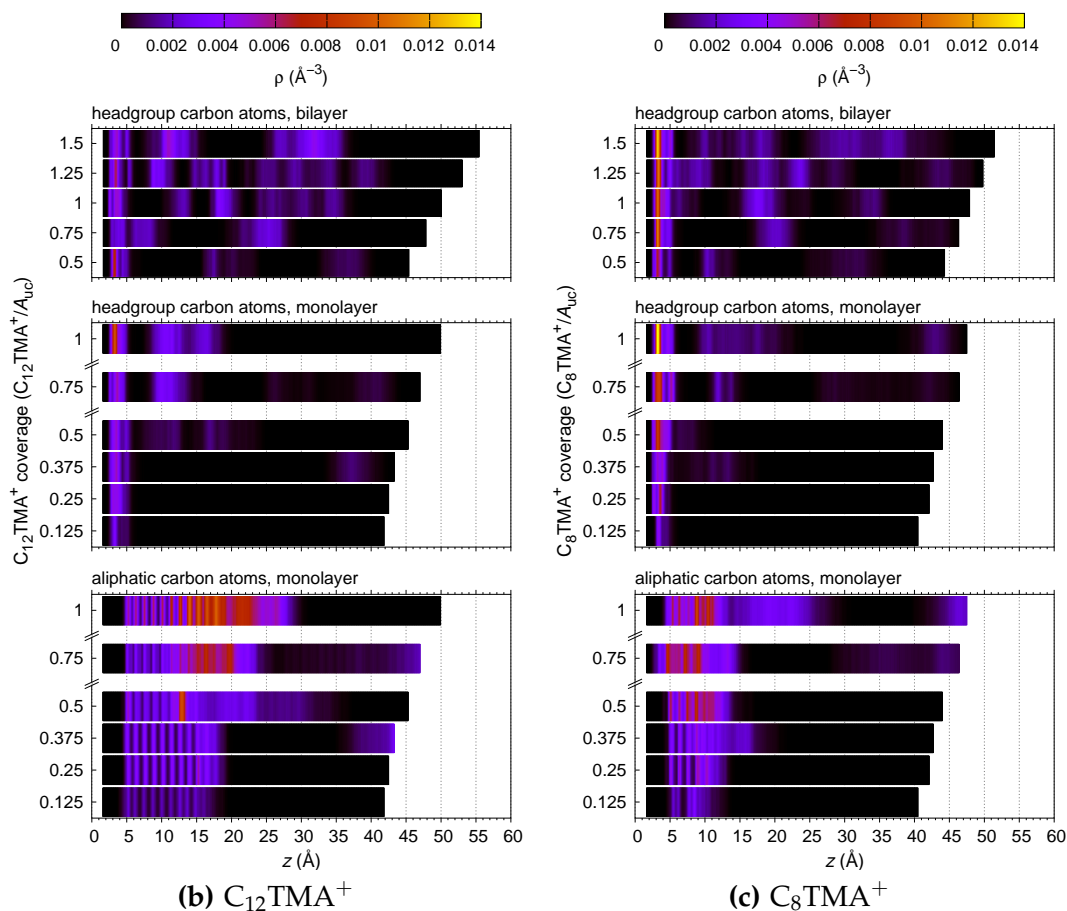


**Figure 5.4 – continued.** Vertical atomic density profiles for carbon atoms of (b)  $C_{12}\text{TMA}^+$  and (c)  $C_8\text{TMA}^+$  headgroups and alkyl chains as functions of the distance  $z$  from the montmorillonite surface.

the most frequently occurring vertical distances between the atoms of inner-sphere adsorbed  $C_n\text{TMA}^+$  ions and the montmorillonite surface. The calculated values are in the ranges of  $z \in [1.5 \text{ \AA}, 2.95 \text{ \AA}]$  for hydrogen,  $z \in [2.35 \text{ \AA}, 3.45 \text{ \AA}]$  for carbon, and  $z \in [3.65 \text{ \AA}, 4.25 \text{ \AA}]$  for nitrogen atoms of  $C_n\text{TMA}^+$  headgroups. The comparison of the atomic density profiles for the hydrogen atoms of  $C_n\text{TMA}^+$  ions and water (see figure 5.5) further indicates that their distributions start at very similar  $z$ -values.

The most frequently occurring distances between inner-sphere adsorbed  $C_n\text{TMA}^+$  ions and the basal oxygen atoms of the montmorillonite surface are represented by the first maxima of the radial distribution functions  $g(r)$  of basal oxygen around the

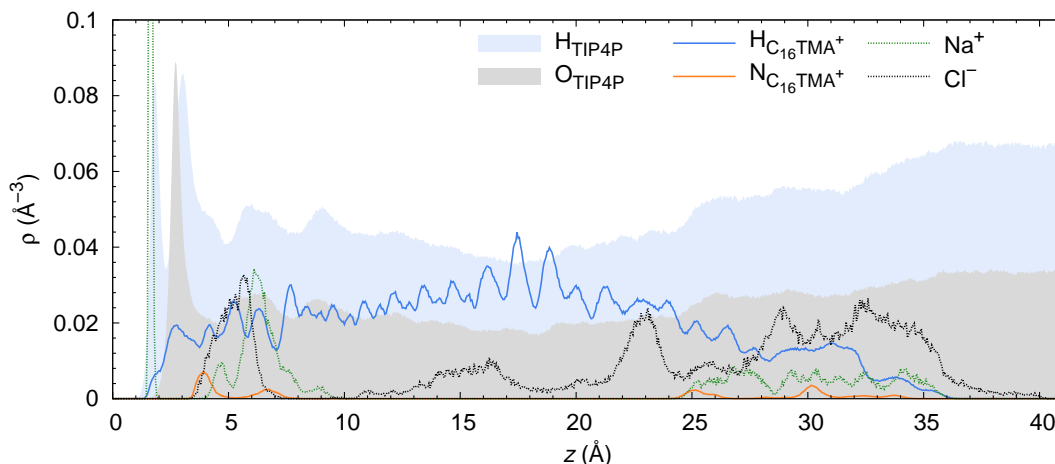


**Figure 5.5** – Vertical atomic density profiles for water,  $C_{16}\text{TMA}^+$ , sodium, and chloride as functions of the distance  $z$  from the montmorillonite surface for the bilayer arrangement at a coverage of  $0.75 C_{16}\text{TMA}^+ / A_{uc}$ . The density profiles for  $\text{Na}^+$  and  $\text{Cl}^-$  are scaled by a factor of 4.

surfactant headgroups. Representative radial distribution functions are shown in figure 5.6 for the monolayer arrangement at a coverage of  $0.375 C_{16}\text{TMA}^+ / A_{uc}$ . The calculated separations are in the ranges of  $2.7 \text{ \AA}$  to  $3.2 \text{ \AA}$  for headgroup hydrogen,  $3.5 \text{ \AA}$  to  $3.8 \text{ \AA}$  for headgroup carbon, and  $4.1 \text{ \AA}$  to  $4.8 \text{ \AA}$  for headgroup nitrogen atoms. These values agree well with the calculated distances between headgroup atoms of  $C_n\text{TMA}^+$  ions and the oxygen atoms of hydrating water molecules, which amount to  $2.9 \text{ \AA}$  for hydrogen,  $3.5 \text{ \AA}$  for carbon, and  $4.6 \text{ \AA}$  for nitrogen (see figure 4.3). This observation confirms that some of the water molecules of the first hydration shells of inner-sphere adsorbed  $C_n\text{TMA}^+$  ions are replaced by basal oxygen atoms of the montmorillonite surface (cf. figure 5.2).

In the lateral direction, the vast majority of the  $C_n\text{TMA}^+$  ions adsorb with their headgroups positioned above the centers of ditrigonal cavities of the montmorillonite surface (see figure 5.2). In contrast to their adsorption on muscovite (see section 4.2), in single systems,  $C_n\text{TMA}^+$  ions were found to be adsorbed above structural Si atoms of the montmorillonite surface as well. For instance, for the monolayer arrangement at a coverage of  $0.5 C_{12}\text{TMA}^+ / A_{uc}$ , surfactant ions are adsorbed above

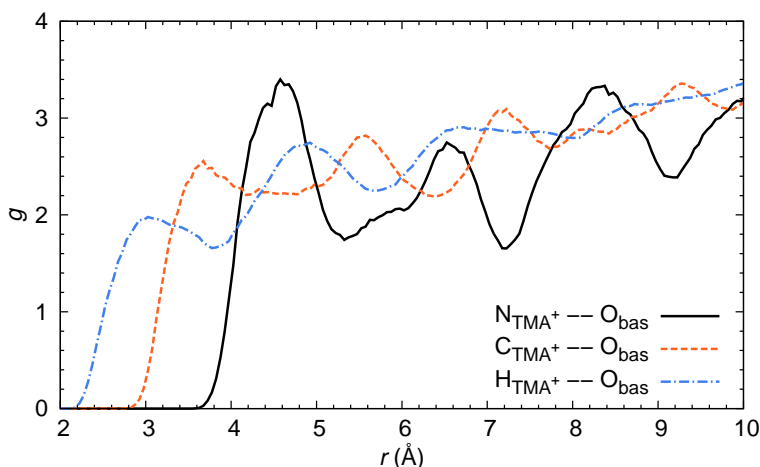


**Figure 5.6** – Radial distribution functions of basal oxygen atoms of the montmorillonite surface around  $C_{16}\text{TMA}^+$  headgroup atoms for the monolayer arrangement at a coverage of  $0.375 C_{16}\text{TMA}^+ / A_{uc}$ .

both centers of ditrigonal cavities (at  $(x, y) \sim (2.5 \text{ \AA}, 17.5 \text{ \AA})$ , figure 5.7) and structural Si atoms of the montmorillonite surface (at  $(x, y) \sim (5 \text{ \AA}, 10.5 \text{ \AA})$ , figure 5.7). However, in none of the simulated systems, surfactant ions were observed to be adsorbed above aluminum substitutions of the tetrahedral sheet.

$C_n\text{TMA}^+$  ions whose nitrogen density distributions exhibit maxima in the ranges of  $z \in [6.4 \text{ \AA}, 8 \text{ \AA}]$  are adsorbed as outer-sphere complexes on the montmorillonite surface. They retain their complete first hydration shells (see figure 5.2(a) and figure 5.7 at  $(x, y) \sim (18 \text{ \AA}, 10 \text{ \AA})$ ). In contrast to inner-sphere adsorbed  $C_n\text{TMA}^+$  ions, the outer-sphere adsorbed ones do not show specific lateral adsorption positions. A characteristic property of the majority of the simulated systems is that some of the  $C_n\text{TMA}^+$  ions possess  $z$ -values of their nitrogen atoms that are higher than  $8 \text{ \AA}$ . Even though most of these ions are still part of the aggregates, they are detached from the montmorillonite surface. In some of the systems, single  $C_n\text{TMA}^+$  ions are desorbed from the aggregates and reside in the solution or are located at the water–vacuum interface (see figure 5.4, e. g., at coverages of  $0.75$  and  $1 C_8\text{TMA}^+ / A_{uc}$ ).

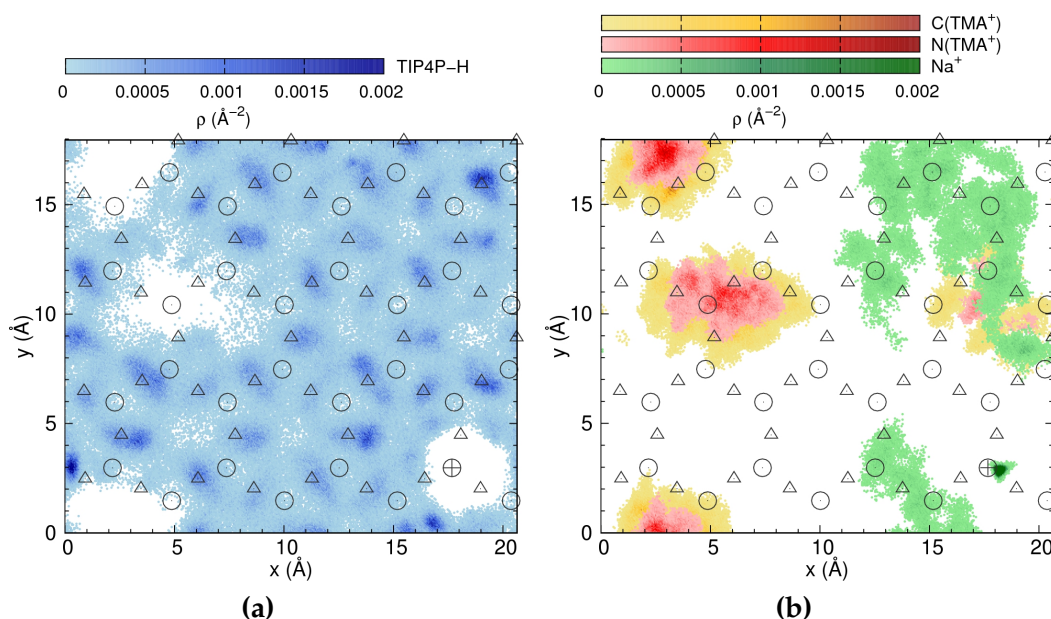


**Figure 5.7** – Lateral atomic density profiles for (a) water hydrogen and (b)  $C_{12}TMA^+$  headgroup carbon, nitrogen, and potassium atoms at the montmorillonite–water interface for the monolayer arrangement at a coverage of  $0.5 C_{12}TMA^+ / A_{uc}$ . The hydrogen density was sampled within the first peak of the corresponding atomic density profile ( $z_{\text{hydrogen}} < 2.3 \text{ \AA}$ ). The headgroup carbon, nitrogen, and sodium densities were sampled within  $8.5 \text{ \AA}$ ,  $8.5 \text{ \AA}$ , and  $5.5 \text{ \AA}$  from the montmorillonite surface to ensure that all inner-sphere and outer-sphere adsorbed cations were taken into account. The circles, crossed circles, and triangles represent silicon, aluminum, and basal oxygen atoms of the tetrahedral sheet at the mineral–water interface, respectively (cf. figure 3.1(b)).

### 5.3 Amount of $C_nTMA^+$ Adsorbed on the External Surface of Montmorillonite

The amounts of  $C_nTMA^+$  that are adsorbed on the montmorillonite surface were estimated from the cumulative density profiles for their nitrogen atoms (see figure 5.8). In all simulated systems, at least  $0.125 C_nTMA^+$  ions per  $A_{uc}$ , corresponding to the lowest simulated  $C_nTMA^+$  coverage, are adsorbed as inner-sphere surface complexes on the montmorillonite surface. In several systems with coverages of at

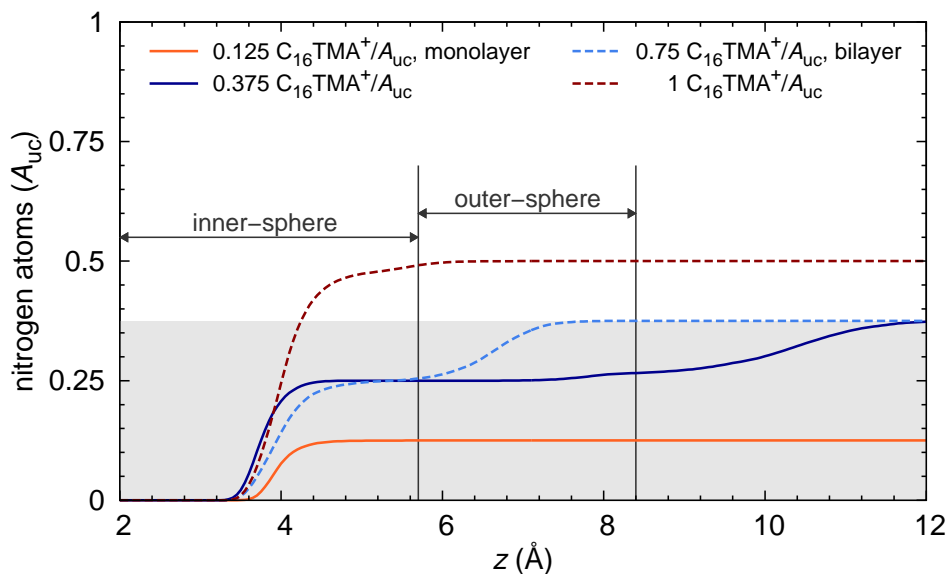


**Figure 5.8** – Cumulative contents of nitrogen atoms as functions of the distance  $z$  from the montmorillonite surface for monolayer and bilayer arrangements at different  $C_{16}\text{TMA}^+$  coverages. The vertical gray lines highlight the maximum  $z$ -values indicating the formation of inner-sphere and outer-sphere adsorption complexes. The gray shade marks those amounts of  $C_n\text{TMA}^+$  that are smaller than required to compensate the charge of the clay surface of  $-0.375 e/A_{uc}$ .

least  $0.75 C_n\text{TMA}^+/A_{uc}$ ,  $C_n\text{TMA}^+$  inner-sphere complexes were observed in excess of the amount required to compensate the charge of the montmorillonite surface of  $-0.375 e/A_{uc}$  (see, e.g., the cumulative nitrogen density profile for the bilayer arrangement at a coverage of  $1 C_{16}\text{TMA}^+/A_{uc}$  in figure 5.8).

Contrary to the formation of inner-sphere surface complexes, the formation of outer-sphere complexes was found to occur only in one fifth of the simulated systems. In general, significantly more inner-sphere than outer-sphere complexes are formed on the montmorillonite surface: On average, only 10% of all adsorption complexes in the simulated systems are outer-sphere ones. This is in contrast to the simulation results for the adsorption of  $C_n\text{TMA}^+$  ions on the cleaved muscovite surface (see section 4.2), in which case more than 50% of all adsorption complexes were found to be outer-sphere ones. The significantly higher fraction of outer-sphere

complexes on the muscovite surface can be attributed to the stronger binding of water molecules to muscovite as compared to montmorillonite (see section 5.1). Other than on montmorillonite, adsorbing  $C_n\text{TMA}^+$  ions have to overcome comparatively high energy barriers to desorb the doubly hydrogen-bonded water molecules from the muscovite surface. As a consequence of this, on muscovite, the formation of  $C_n\text{TMA}^+$  inner-sphere surface complexes is impeded.

An overview of the total amounts of  $C_n\text{TMA}^+$  adsorbed on the montmorillonite surface with respect to the  $C_n\text{TMA}^+$  coverage is given in figure 5.9. The number of  $C_n\text{TMA}^+$  surface complexes generally increases with increasing surface coverage. At the lowest simulated coverages corresponding to  $0.125 C_n\text{TMA}^+ / A_{\text{uc}}$  for the monolayer arrangements and  $0.25 C_n\text{TMA}^+ / A_{\text{uc}}$  for the bilayer arrangements, all available  $C_n\text{TMA}^+$  ions are adsorbed on the montmorillonite surface (see figure 5.9). With increasing  $C_n\text{TMA}^+$  coverage, the surfactant ions are only partially adsorbed. With regard to the amount of  $C_n\text{TMA}^+$  facing the surface, which is half of the surfactant surface coverage in the simulated bilayer systems, the fraction of the  $C_n\text{TMA}^+$  ions forming surface complexes is notably bigger in the bilayer systems than in the corresponding monolayer ones (see figure 5.9). This effect is particularly pronounced for the long chained  $C_{16}\text{TMA}^+$  ions.

Figure 5.9 further indicates that, at a given  $C_n\text{TMA}^+$  coverage, the fraction of the  $C_n\text{TMA}^+$  ions that forms surface complexes is independent of the alkyl chain length. The highest value of  $0.66 C_{16}\text{TMA}^+$  adsorption complexes per  $A_{\text{uc}}$ , corresponding to approximately 1.8 times the negative charge of the montmorillonite surface, was observed at the monolayer coverage of  $1 C_{16}\text{TMA}^+ / A_{\text{uc}}$ . For the bilayer arrangements, the highest value of  $0.5 C_n\text{TMA}^+$  adsorption complexes per  $A_{\text{uc}}$  was observed at the coverages of  $1 C_{16}\text{TMA}^+ / A_{\text{uc}}$  and  $1.5 C_8\text{TMA}^+ / A_{\text{uc}}$ .

The simulation results indicate that montmorillonite can adsorb significantly more  $C_n\text{TMA}^+$  cations on its external surfaces than are required to compensate its negative surface charge. Albeit previous experiments lacked the feature to distinguish between the amounts of organic cations adsorbed in the interlayer spaces

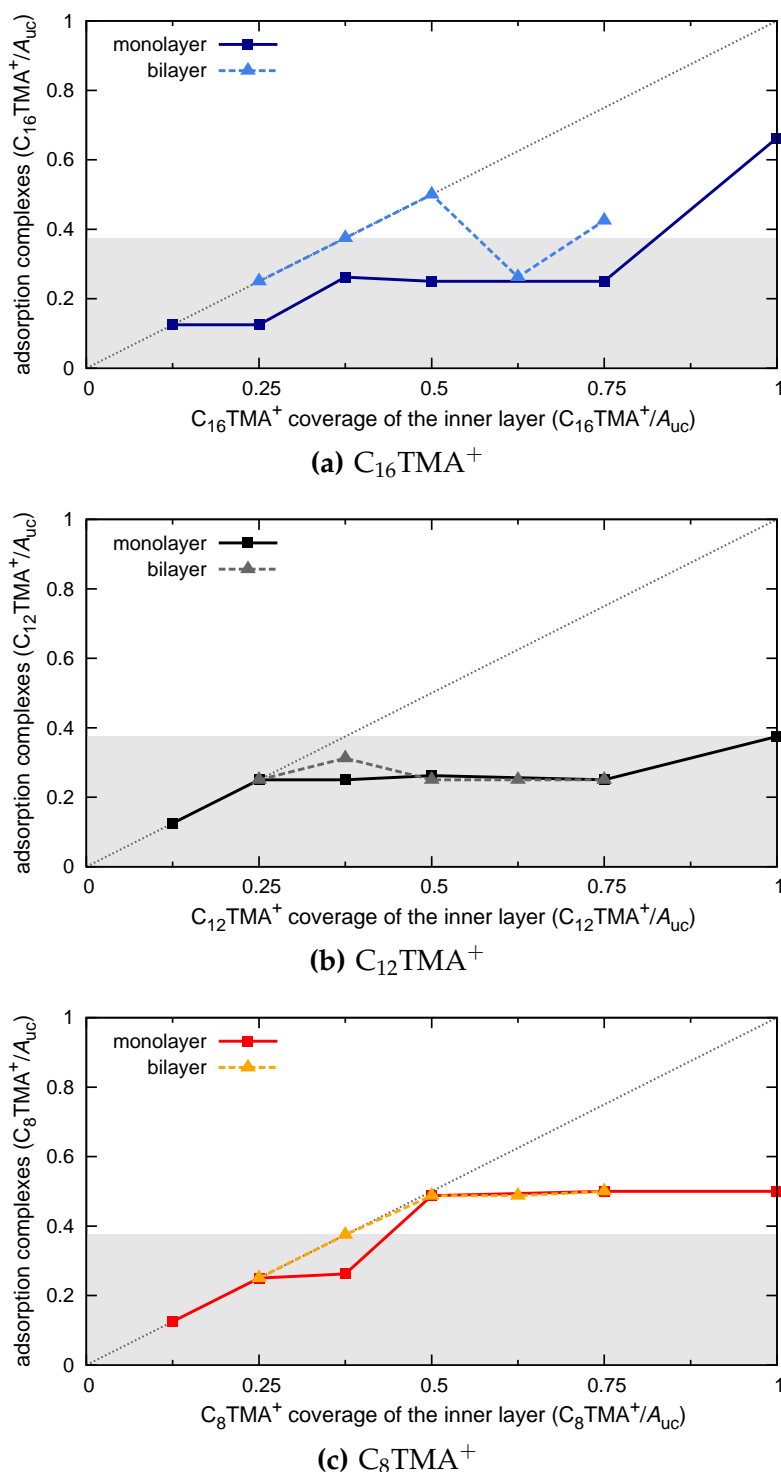


**Figure 5.9** – Amounts of  $C_n\text{TMA}^+$  adsorbed on the montmorillonite surface for (a)  $C_{16}\text{TMA}^+$ , (b)  $C_{12}\text{TMA}^+$ , and (c)  $C_8\text{TMA}^+$  monolayer and bilayer arrangements as functions of the  $C_n\text{TMA}^+$  coverage of the surfactant layers facing the montmorillonite surface. The dotted gray lines mark those amounts of  $C_n\text{TMA}^+$  that correspond to the adsorption of all surfactant ions at a given  $C_n\text{TMA}^+$  coverage. The gray shades mark those amounts of  $C_n\text{TMA}^+$  that are smaller than required to compensate the charge of the clay surface of  $-0.375 e/A_{uc}$ .



and on the external surfaces of clay particles, their results showed corresponding trends [8, 15, 99, 139]. Lee and Kim [139] and Zhu et al. [99] observed that an increased concentration of  $C_n\text{TMA}^+$  ions in the solution leads to an increased amount of  $C_n\text{TMA}^+$  adsorbed by the montmorillonite. The maximum uptake of  $C_n\text{TMA}^+$  ions by montmorillonite was determined to equal approximately 2.5 times its CEC. Schampera and Dultz [15] observed that the organic cations  $\text{BE}^+$ ,  $\text{TPP}^+$ , and  $\text{HDPy}^+$  are completely adsorbed by Wyoming montmorillonite up to offered amounts corresponding to approximately 80% of the CEC of the clay. At greater offers, the organic cations are only partially adsorbed [8, 15].

In contrast to their adsorption on muscovite, the adsorption of  $C_n\text{TMA}^+$  ions on the external surface of montmorillonite leads to a significant decrease of the density of the first water layers (see figure 5.1(b)). For each simulated system, the number of  $C_n\text{TMA}^+$  inner-sphere surface complexes was plotted against the number of water molecules in the first water layer with  $z_{\text{oxygen}} \leq 4.7 \text{ \AA}$  (see figure 5.10). The plot illustrates the approximately linear relationship between the two parameters. The data points were fitted by a linear least squares fit.<sup>1</sup> The intercept of the axis, which describes the number of molecules in the first water layer per  $A_{\text{uc}}$ , was not fixed.

The regression line indicates that with each adsorbed  $C_n\text{TMA}^+$  inner-sphere complex per  $A_{\text{uc}}$ , the density of the first water layer is decreased by approximately 4.2 water molecules per  $A_{\text{uc}}$ , corresponding to approximately 70%. The plotted data points exhibit a standard deviation of 0.18 molecules per  $A_{\text{uc}}$  from the values estimated by the regression line. For the inorganic reference system, the regression line predicts a number of 6.15 molecules per  $A_{\text{uc}}$  that are adsorbed in the first water layer. This value deviates by only 2% from the result of the MC simulation of 6.27 molecules per  $A_{\text{uc}}$ . Accordingly, the amounts of water in the first water layers predicted by the regression line show an excellent agreement with the results of

<sup>1</sup>An outlier, which was not taken into account for the regression, was observed for the monolayer arrangement at a coverage of  $0.57 C_8\text{TMA}^+ / A_{\text{uc}}$ . In this system, only 2.9 water molecules per  $A_{\text{uc}}$  are adsorbed in the first water layer. This is due to  $0.125 C_8\text{TMA}^+ / A_{\text{uc}}$  that are adsorbed with their alkyl chains arranged parallel to the montmorillonite surface (see figure A.1). The increased density of methyl(ene) groups at the montmorillonite–water interface leads to an increased desorption of water molecules and thus to a strong decrease of the density of the first water layer.

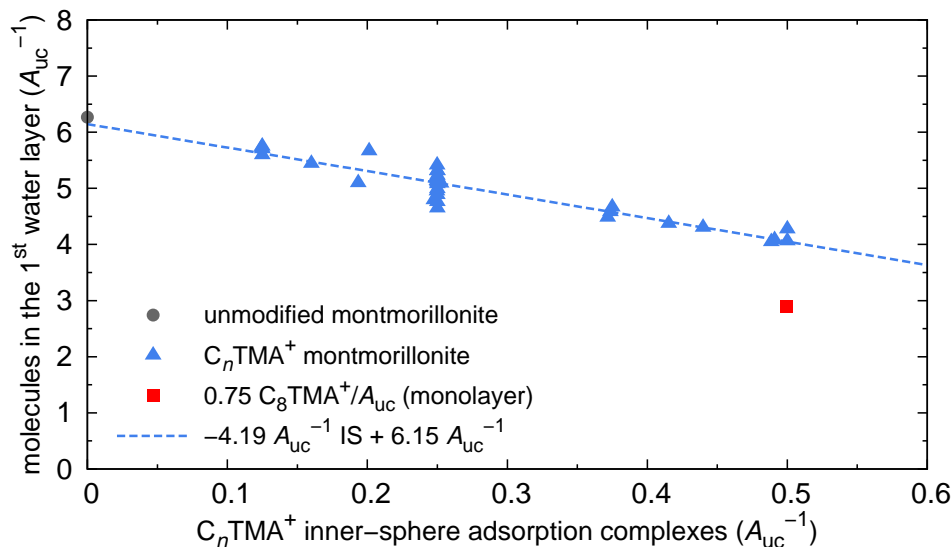


**Figure 5.10** – Number of molecules in the first water layer adsorbed on the montmorillonite surface with  $z_{\text{oxygen}} \leq 4.7 \text{ \AA}$  as a function of the number of  $C_n\text{TMA}^+$  inner-sphere surface complexes. The data point for the monolayer arrangement at a coverage of  $0.75 C_8\text{TMA}^+/A_{uc}$  (marked in red) was not taken into account for the regression. In this system,  $0.125 C_8\text{TMA}^+/A_{uc}$  are adsorbed parallel to the montmorillonite surface and the alkyl chains displace water in excess of the amount expected to be displaced otherwise (cf. figure A.1).

the MC simulations, even though, e. g., outer-sphere adsorbed  $C_n\text{TMA}^+$  ions and inorganic ions present at the montmorillonite–aggregate interfaces are not included into this simple linear model.

## 5.4 Positions of the Inorganic Ions

On unmodified montmorillonite,  $0.125 \text{ Na}^+/A_{uc}$  are adsorbed as inner-sphere complexes above the tetrahedral charge substitutions of the basal surface (see figure 5.3(a)). This amount of adsorbed sodium equals the density of the tetrahedral substitutions of the basal surface. The remaining sodium ions are adsorbed as outer-sphere complexes ( $0.125 \text{ Na}^+/A_{uc}$ ) or are located in a diffuse layer above the mineral surface with  $z < 12 \text{ \AA}$  ( $0.125 \text{ Na}^+/A_{uc}$ ). The sodium ions that are adsorbed as outer-sphere complexes do not exhibit specific lateral adsorption positions and

show a considerably higher lateral mobility than the inner-sphere adsorbed ions (see figure 5.3(a)).

In the mineral-water-organics systems with surfactant coverages smaller than  $0.75 C_n\text{TMA}^+ / A_{\text{uc}}$ , the inner-sphere adsorbed sodium ions remain adsorbed on the montmorillonite surface (see figure 5.11). In single systems with higher  $C_n\text{TMA}^+$  coverages, the desorption of sodium ions from their positions above the tetrahedral substitutions was observed (see, e. g., the systems with monolayer coverages of  $1 C_{16}\text{TMA}^+ / A_{\text{uc}}$ ,  $0.75 C_{12}\text{TMA}^+ / A_{\text{uc}}$ , and  $1 C_8\text{TMA}^+ / A_{\text{uc}}$  in figure 5.11). The vertical and lateral adsorption positions of inner-sphere adsorbed sodium ions are the same as on the unmodified montmorillonite surface. The maxima of their vertical density distributions are in the ranges of  $z \in [1.6 \text{ \AA}, 1.65 \text{ \AA}]$  (see figures 5.5 and 5.11). This shows that the inner-sphere adsorbed sodium ions are located even closer to the montmorillonite surface than the water molecules of the first water layer hydrating the clay surface (see figure 5.5). Sodium ions residing at distances of  $z \in [4.1 \text{ \AA}, 4.7 \text{ \AA}]$  away from the montmorillonite surface are adsorbed as outer-sphere complexes. Their vertical position coincides with the first minimum of the water oxygen density distribution (cf. figures 5.1(b) and 5.11).

A maximum of 0.71 cation surface complexes per  $A_{\text{uc}}$ , comprising all inner-sphere and outer-sphere surface complexes of sodium and  $C_n\text{TMA}^+$  ions, was observed for the bilayer arrangement at a coverage of  $1.5 C_{16}\text{TMA}^+ / A_{\text{uc}}$ . This amount corresponds to approximately twice the charge required to compensate the negative charge of the clay surface. The excess positive charge is counterbalanced by chloride anions residing close to the montmorillonite surface. A comparison of the vertical atomic density profiles for headgroup carbon atoms and chloride (cf. figures 5.4 and 5.12) indicates that the vast majority of the chloride ions assemble in the vicinity of  $C_n\text{TMA}^+$  headgroups at the montmorillonite–aggregate interface and, for bilayer aggregates, likewise at the aggregate–water interface. For example, for the bilayer arrangement at a coverage of  $1.5 C_{16}\text{TMA}^+ / A_{\text{uc}}$ , half of the chloride ions are located in the vertical regions that are occupied by the headgroup atoms

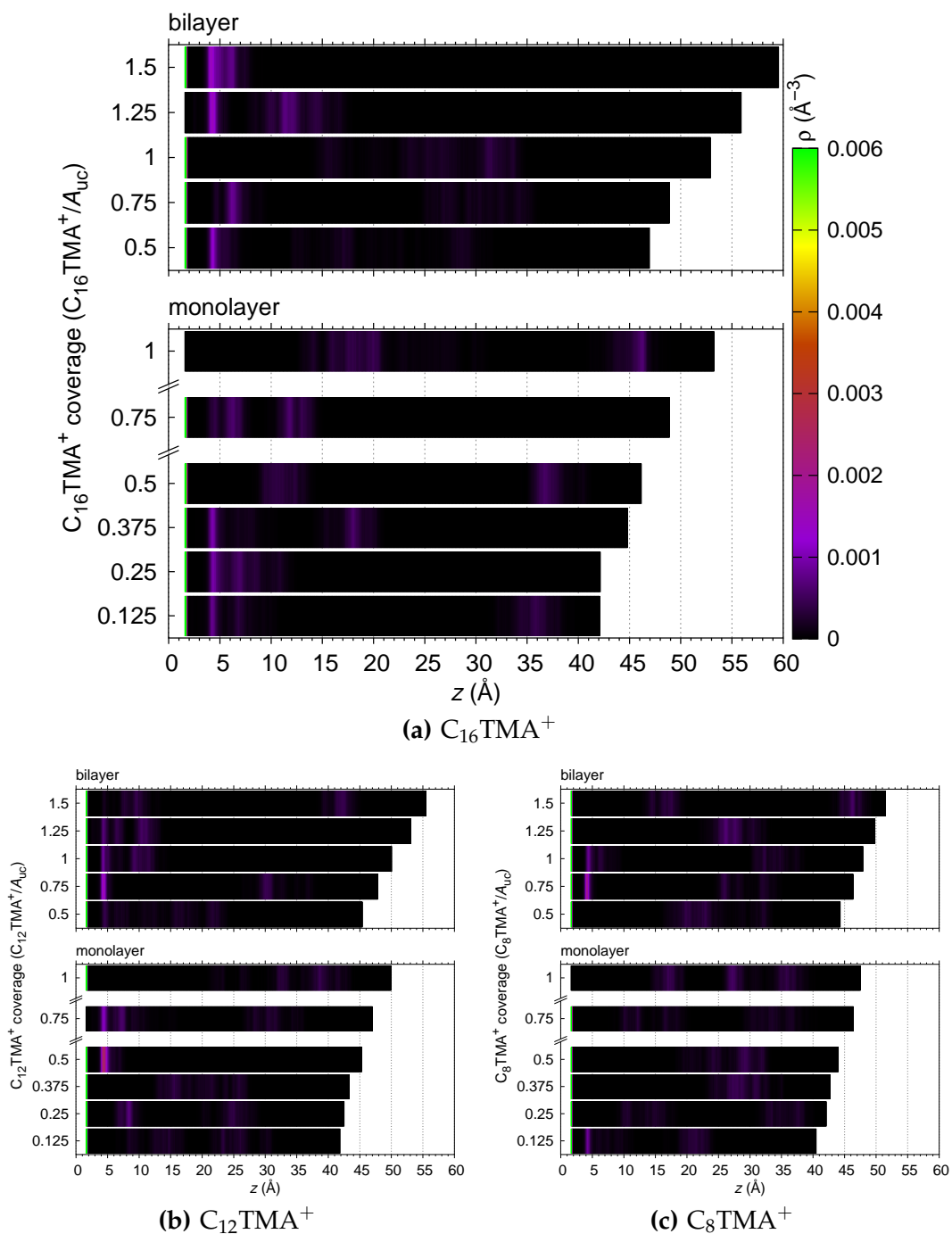


**Figure 5.11** – Vertical atomic density profiles for sodium in (a)  $C_{16}\text{TMA}^+$ , (b)  $C_{12}\text{TMA}^+$ , and (c)  $C_8\text{TMA}^+$  systems as functions of the distance  $z$  from the montmorillonite surface. Coverages ranging from  $0.125 C_n\text{TMA}^+/A_{uc}$  to  $1 C_n\text{TMA}^+/A_{uc}$  and from  $0.5 C_n\text{TMA}^+/A_{uc}$  to  $1.5 C_n\text{TMA}^+/A_{uc}$  are shown for monolayer and bilayer arrangements, respectively. For each simulated system, the extension of the water film between the montmorillonite–water interface ( $z = 0 \text{\AA}$ ) and the water–vacuum interface is indicated by a black bar.

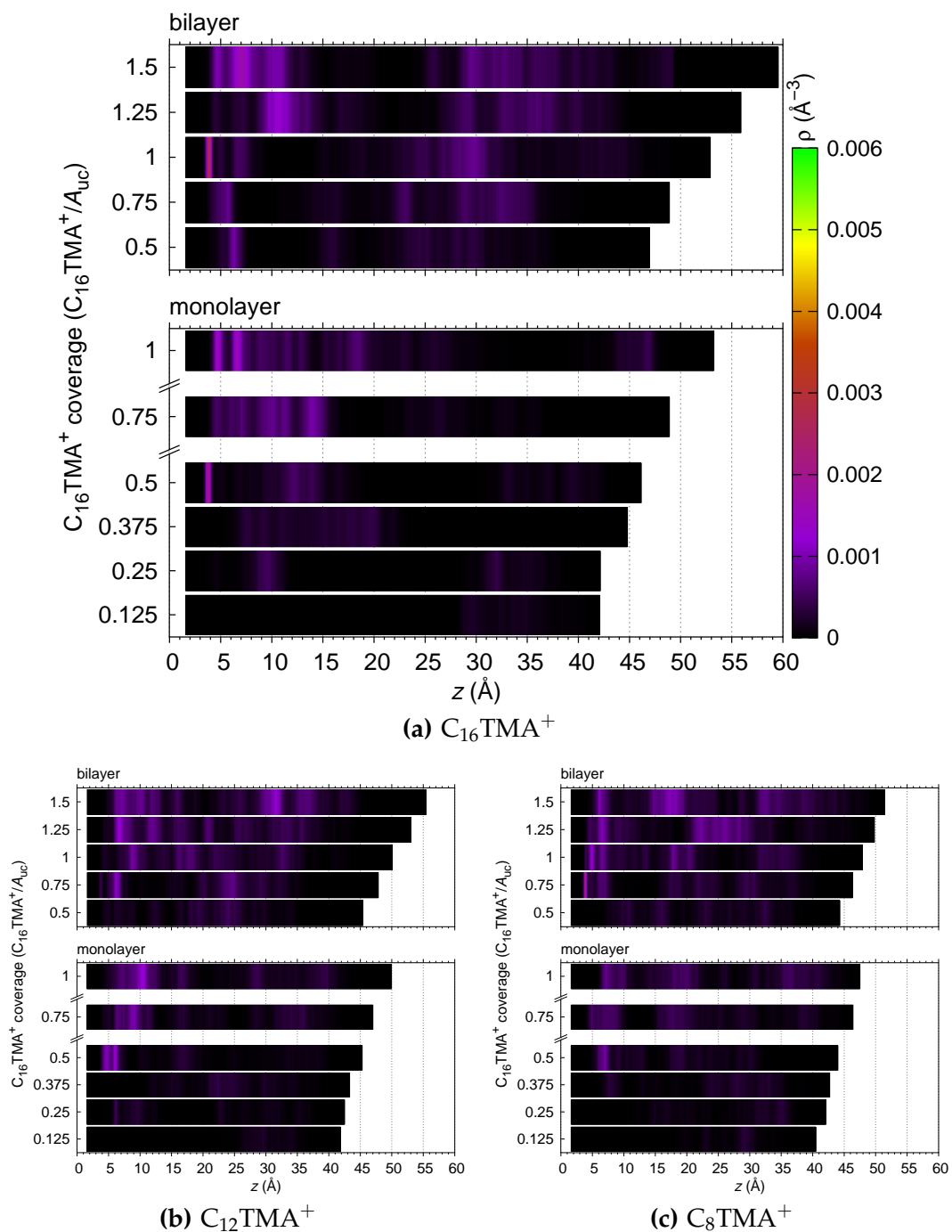


**Figure 5.12** – Vertical atomic density profiles for chloride in (a)  $C_{16}TMA^+$ , (b)  $C_{12}TMA^+$ , and (c)  $C_8TMA^+$  systems as functions of the distance  $z$  from the montmorillonite surface. Coverages ranging from  $0.125 C_nTMA^+/A_{uc}$  to  $1 C_nTMA^+/A_{uc}$  and from  $0.5 C_nTMA^+/A_{uc}$  to  $1.5 C_nTMA^+/A_{uc}$  are shown for monolayer and bilayer arrangements, respectively. For each simulated system, the extension of the water film between the montmorillonite–water interface ( $z = 0 \text{ \AA}$ ) and the water–vacuum interface is indicated by a black bar.

of the inner  $C_{16}\text{TMA}^+$  layer at the mineral–aggregate interface (see figures 5.12 and 5.13(b)).

The analysis of the radial distribution functions of chloride around sodium ions and  $C_n\text{TMA}^+$  headgroups confirms that both contact and solvent-separated ion pairs of chloride are formed with sodium and  $C_n\text{TMA}^+$  ions adsorbed on or desorbed from the montmorillonite surface. The observed co-adsorption of chloride on the montmorillonite surface strongly supports the theory derived from experimental observations that the adsorption capacities of organoclays for anions originate from the uptake of counterions together with the organic cations [17, 52, 53]. In most of the simulated systems, fractions of the sodium ions remain adsorbed on the montmorillonite surface. This explains the experimental observation that even those organoclays possess adsorption capacities for cations, which exhibit uptakes of organic cations exceeding their cation exchange capacities [12, 17].

## 5.5 Structure and Thickness of the Adsorbed Aggregates

The analysis of the aggregate structures of the simulated systems shows that up to coverages of  $0.375 C_n\text{TMA}^+ / A_{\text{UC}}$ , the surfactant ions are adsorbed on the montmorillonite surface as monomers or dimers. At higher coverages, the  $C_n\text{TMA}^+$  ions form aggregates, which partially cover the montmorillonite surface and are laterally separated from water. This aggregation behavior is in close analogy to the assembly of  $C_n\text{TMA}^+$  ions on muscovite (see section 4.5).

The two layers composing the  $C_n\text{TMA}^+$  bilayer aggregates at the montmorillonite surface are interdigitated for all three studied chain lengths (see figures 5.13(b) and 5.14(b)). This interdigitation is less pronounced for the aggregates formed by the short-chained  $C_8\text{TMA}^+$  ions. Furthermore, with decreasing chain length, increasing amounts of  $C_n\text{TMA}^+$  are desorbed from the aggregates. These desorbed surfactant ions reside as monomers in the solution or are located at the water–vacuum interface (see figure 5.14). Thus, even though the total number of adsorbed  $C_n\text{TMA}^+$  ions

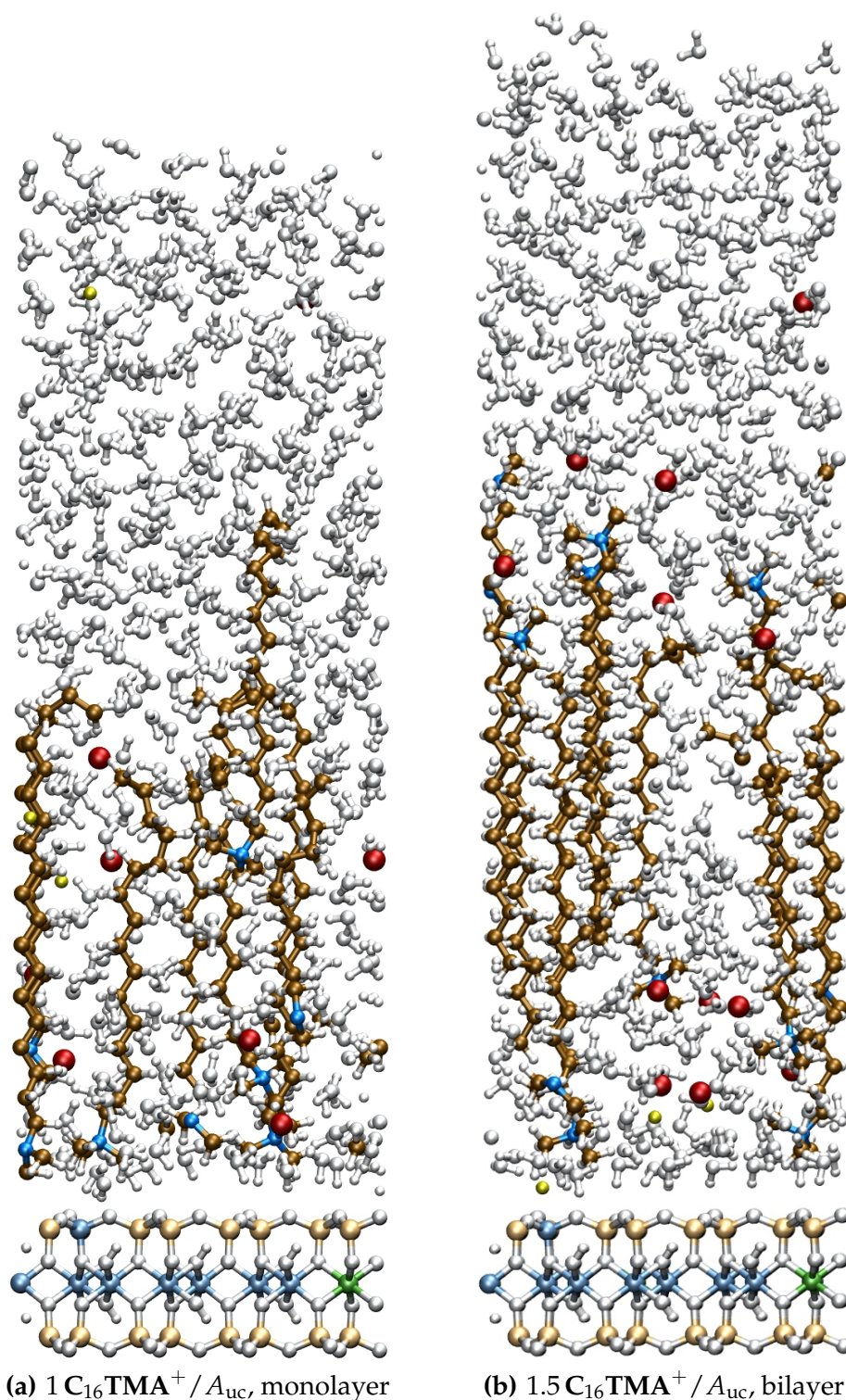


**Figure 5.13** – Snapshots of the simulated equilibrium configurations for (a) the monolayer arrangement at a coverage of  $1 C_{16}TMA^+ / A_{uc}$  and (b) the bilayer arrangement at a coverage of  $1.5 C_{16}TMA^+ / A_{uc}$ , viewed parallel to the montmorillonite–water interface. Ball and stick colors: yellow ( $Na^+$ ), red ( $Cl^-$ ), brown (C), blue (N), white (H), light gray (O), beige (Si), light blue (Al), green (Mg).

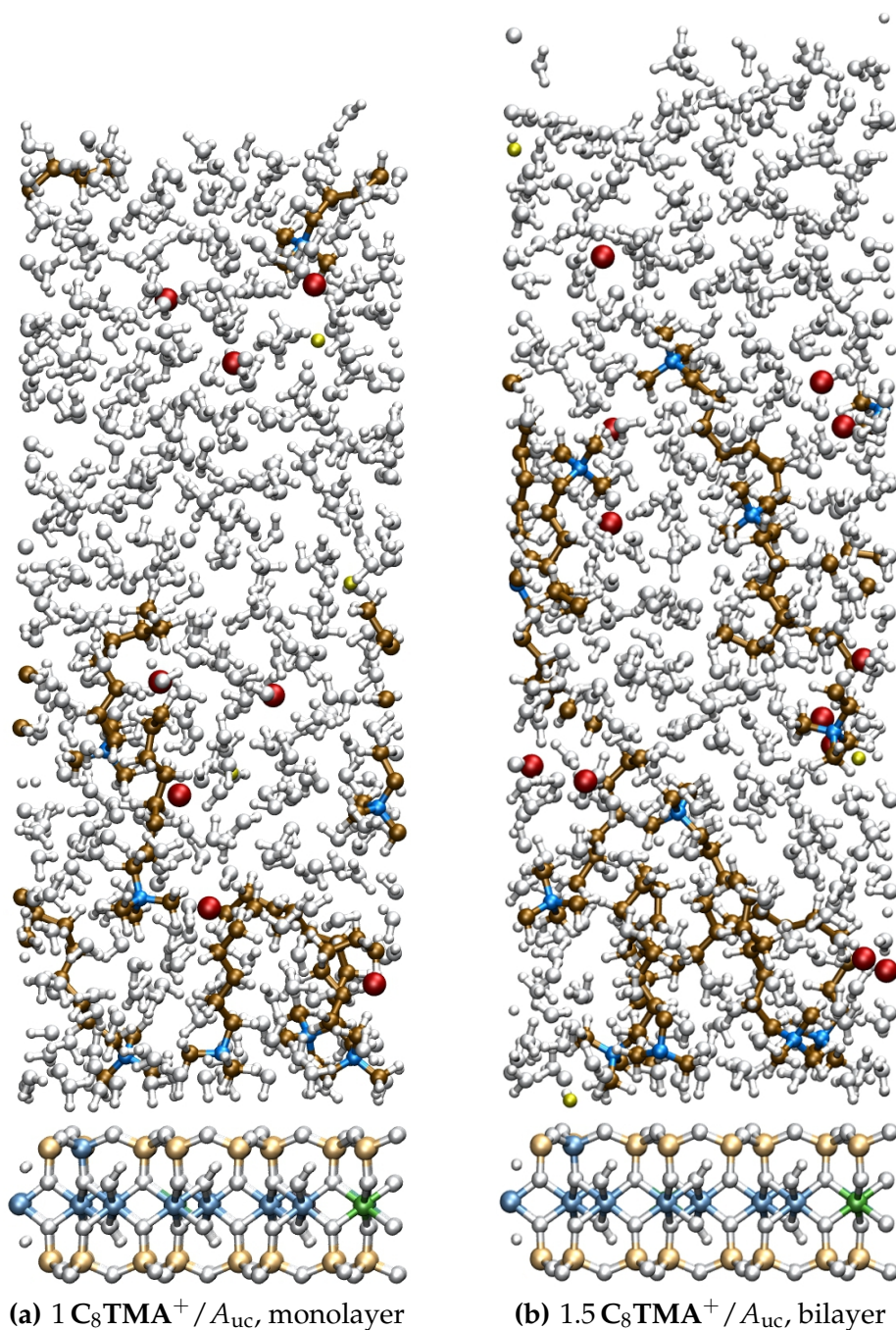


**Figure 5.14** – Snapshots of the simulated equilibrium configurations for (a) the monolayer arrangement at a coverage of  $1 C_8\text{TMA}^+ / A_{uc}$  and (b) the bilayer arrangement at a coverage of  $1.5 C_8\text{TMA}^+ / A_{uc}$ , viewed parallel to the montmorillonite–water interface. Ball and stick colors: yellow ( $\text{Na}^+$ ), red ( $\text{Cl}^-$ ), brown (C), blue (N), white (H), light gray (O), beige (Si), light blue (Al), green (Mg).



is independent of the alkyl chain length (see section 5.3), the amount of  $C_n\text{TMA}^+$  aggregated at the montmorillonite surface increases with increasing surfactant alkyl chain length (cf. figures 5.13 and 5.14). This observation can be attributed to increased hydrophobic interactions between the longer surfactant alkyl chains. The increase of the amount of aggregated  $C_n\text{TMA}^+$  with increasing alkyl chain length is in good agreement with the experimental results by Atkin et al., which indicate that the surface excess of  $C_n\text{TMA}^+$  ions on silica at a given concentration increases with the surfactant alkyl chain length [140].

The degree of conformational order within the surfactant aggregates was analyzed with the help of the calculated gauche conformation fractions of the alkyl chains (see figure 5.15). A trend of decreasing conformational order with decreasing alkyl chain length was observed. Furthermore, for all three considered chain lengths, at a given surfactant surface coverage, the bilayer aggregates exhibit higher conformational order than the monolayer ones. This effect can be attributed to increased hydrophobic interactions between the alkyl chains of the opposed layers composing the interdigitated bilayer aggregates. The calculated gauche conformation fractions of the alkyl chains vary in the ranges of 10% – 33% for  $C_{16}\text{TMA}^+$ , 8% – 26% for  $C_{12}\text{TMA}^+$ , and 25% – 38% for  $C_8\text{TMA}^+$  monolayer aggregates. For bilayer aggregates, the calculated gauche conformation fractions are in the ranges of 6% – 15% for  $C_{16}\text{TMA}^+$ , 9% – 16% for  $C_{12}\text{TMA}^+$ , and 23% – 34% for  $C_8\text{TMA}^+$ . With increasing surface coverage, a slight increase of conformational order was observed to occur within the monolayer aggregates of the long-chained  $C_{16}\text{TMA}^+$  ions. This trend could not be observed for the aggregates formed by the shorter-chained  $C_{12}\text{TMA}^+$  and  $C_8\text{TMA}^+$  ions.

In analogy to the simulation results for muscovite (see section 4.5), the calculated gauche conformation fractions exhibit comparatively high standard deviations of up to 19%. This manifests the coexistence of nearly fully extended chains and chains with high numbers of gauche conformations in the same systems. Furthermore, the  $C_{16}\text{TMA}^+$  and  $C_{12}\text{TMA}^+$  aggregates assembled on the external surface of mont-

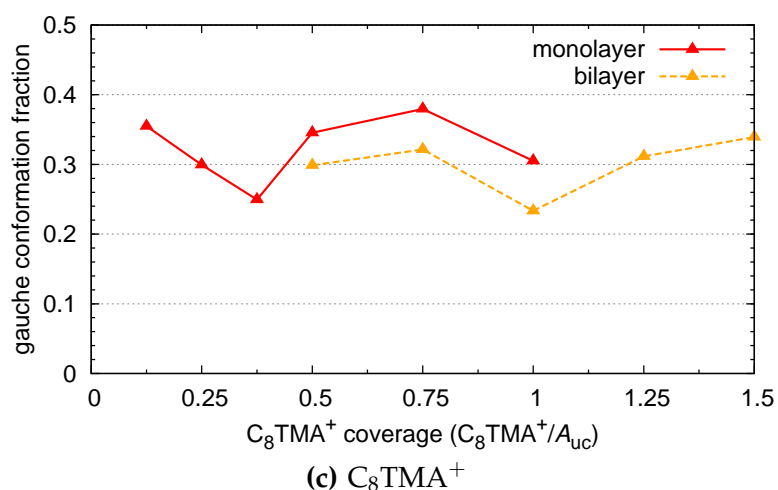
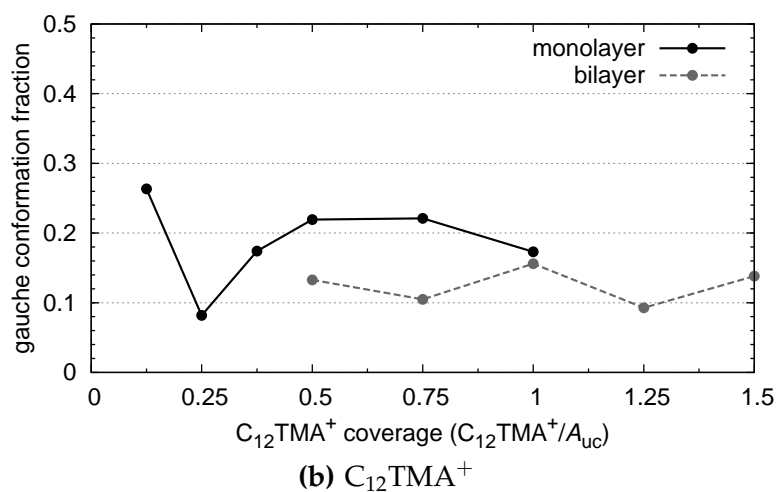
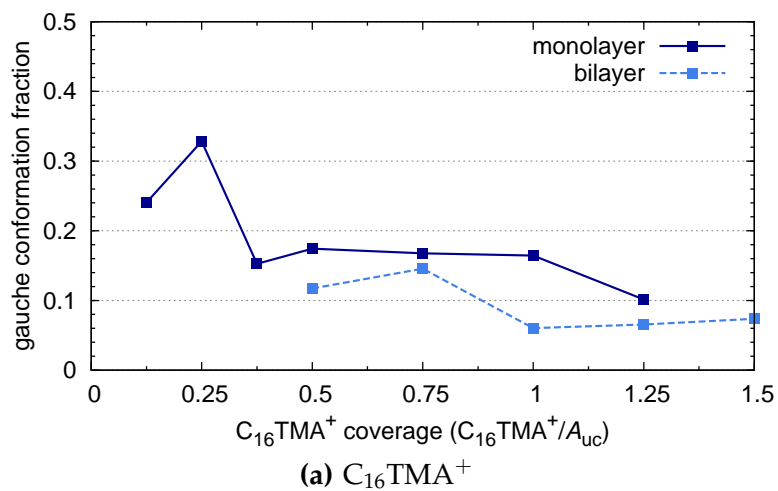


**Figure 5.15** – Fractions of gauche conformations of the alkyl chains as functions of the (a)  $C_{16}\text{TMA}^+$ , (b)  $C_{12}\text{TMA}^+$ , and (c)  $C_8\text{TMA}^+$  coverage for monolayer and bilayer arrangements. Torsion angles of  $60^\circ \pm 60^\circ$  and  $300^\circ \pm 60^\circ$  were counted as gauche conformations. Lines were added as guides to the eye.

morillonite exhibit greater fractions of gauche conformations than the aggregates assembled on cleaved muscovite at the same coverages (cf. figures 4.14 and 5.15).

The apparent aggregate thicknesses were estimated on the basis of the vertical atomic density profiles for the carbon atoms of  $C_n\text{TMA}^+$  alkyl chains (monolayer aggregates) and headgroups (bilayer aggregates) (see figure 5.4). The  $C_{16}\text{TMA}^+$  monolayer aggregates exhibit thicknesses of approximately 23 Å at the coverages of  $0.125 C_{16}\text{TMA}^+ / A_{\text{uc}}$  and  $0.25 C_{16}\text{TMA}^+ / A_{\text{uc}}$  (see figure 5.4(a)). With increasing surface coverage, the apparent aggregate thickness increases to up to 35 Å and 32 Å at coverages of  $0.75 C_{16}\text{TMA}^+ / A_{\text{uc}}$  and  $1 C_{16}\text{TMA}^+ / A_{\text{uc}}$ , respectively. This increase of aggregate thickness is due to  $C_{16}\text{TMA}^+$  ions that are located with their headgroup atoms at  $z$ -values of approximately 15 Å. They are not adsorbed on the montmorillonite surface but nevertheless take part in the aggregation through hydrophobic interactions of their alkyl chains (see figure 5.13(a)). These detached but yet aggregated  $C_n\text{TMA}^+$  ions have higher  $z$ -values of the carbon atoms of their alkyl chains than the ions that are adsorbed on montmorillonite as inner-sphere or outer-sphere surface complexes. As a result, the thickness of the aggregate is increased.

For the monolayer aggregates formed by  $C_{12}\text{TMA}^+$  and  $C_8\text{TMA}^+$  ions, a similar behavior was observed. The determined aggregate thicknesses are in the ranges of 18 Å to 25 Å and 13 Å to 17 Å, respectively. In single systems, carbon atoms of the alkyl chains are located at  $z$ -values of up to 32 Å for  $C_{12}\text{TMA}^+$  aggregates and up to 27 Å for  $C_8\text{TMA}^+$  aggregates (see, e. g., figures 5.4(b) and 5.4(c) at coverages of  $0.5 C_{12}\text{TMA}^+ / A_{\text{uc}}$ ,  $1 C_{12}\text{TMA}^+ / A_{\text{uc}}$ , and  $1 C_8\text{TMA}^+ / A_{\text{uc}}$ ). These ions are detached from the surfactant aggregates and are located at the aggregate-solution interface (see figure 5.14(a)).

Similarly, the thicknesses of the  $C_n\text{TMA}^+$  bilayer aggregates slightly increase with the surfactant surface coverage. The calculated thicknesses are in the ranges of 30 Å to 39 Å for  $C_{16}\text{TMA}^+$  and 23 Å to 36 Å for  $C_{12}\text{TMA}^+$ . The simulated  $C_8\text{TMA}^+$  bilayer aggregates exhibit thicknesses of 23 Å and 20 Å at coverages of  $0.75 C_8\text{TMA}^+ / A_{\text{uc}}$  and  $1 C_8\text{TMA}^+ / A_{\text{uc}}$ , respectively. At all other simulated

coverages, significant fractions of the surfactant ions are characterized by large separations from the surface and are desorbed from the aggregates. For these systems, the aggregate thicknesses could not be determined unambiguously.

The determined aggregate thicknesses are consistent with the thicknesses of the  $C_n\text{TMA}^+$  aggregates assembled on muscovite (cf. section 4.5). In general, slightly smaller extensions in the  $z$ -direction were observed for the aggregates formed on the external surface of montmorillonite. This effect can be attributed to the significantly greater fraction of inner-sphere surface complexes formed on montmorillonite as compared to muscovite, resulting in a closer approach of the surfactant ions to the mineral surface.

## 5.6 Summary of the Simulation Results

The simulation results indicate that approximately 90 % of the adsorbed  $C_n\text{TMA}^+$  ions form inner-sphere complexes on the montmorillonite surface. In the lateral direction, they are mainly adsorbed above ditrigonal cavities of the clay surface. The distances between their nitrogen atoms and the clay surface are in the range of 3.65 Å to 4.25 Å. The inner-sphere adsorbed  $C_n\text{TMA}^+$  ions penetrate the first water layer adsorbed on the montmorillonite surface and displace water molecules from their adsorption positions. On average, with each adsorbed  $C_n\text{TMA}^+$  inner-sphere complex per  $A_{uc}$ , the density of the first water layer is decreased by approximately 70 %.

Those 10 % of the  $C_n\text{TMA}^+$  ions that form outer-sphere complexes on the montmorillonite surface are characterized by  $z$ -values of their nitrogen atoms varying between 6.4 Å and 8 Å. In contrast to the inner-sphere adsorbed  $C_n\text{TMA}^+$  ions, they do not show specific lateral adsorption positions. In agreement with experiments (cf. [8, 15, 99, 139]), the amount of adsorbed  $C_n\text{TMA}^+$  increases with the  $C_n\text{TMA}^+$  surface coverage. At the lowest simulated coverages, for both the monolayer and the bilayer arrangements, all available  $C_n\text{TMA}^+$  ions are adsorbed on the montmorillonite surface. At higher coverages, only parts of the aggregated surfactant ions form

adsorption complexes. The highest observed value of  $0.66 C_n\text{TMA}^+$  adsorption complexes per  $A_{\text{uc}}$  considerably exceeds that amount required to compensate the negative charge of the montmorillonite surface of  $-0.375 e/A_{\text{uc}}$ .

Even at these high  $C_n\text{TMA}^+$  adsorption rates, a fraction of the sodium ions remains adsorbed above the tetrahedral substitutions of the montmorillonite surface in most of the simulated systems. This explains the experimental observation (cf. [12, 17]) that even those organoclays possess adsorption capacities for cations, which exhibit uptakes of organic cations exceeding their cation exchange capacities. The positive charge at the montmorillonite surface is counterbalanced by chloride anions, which are located in the regions around the hydrophilic  $C_n\text{TMA}^+$  headgroups and form ion pairs with both  $C_n\text{TMA}^+$  and sodium ions. The observed co-adsorption of chloride on the montmorillonite surface strongly supports the theory derived from experiments that the adsorption capacities of organoclays for anions originate from the uptake of counterions together with the organic cations (cf. [17, 52, 53]).

Up to simulated coverages of  $0.375 C_n\text{TMA}^+ / A_{\text{uc}}$ , the surfactant ions are adsorbed on the montmorillonite surface as monomers or dimers. At higher coverages, the  $C_n\text{TMA}^+$  ions form aggregates that are laterally separated from water and partially cover the montmorillonite surface. The amount of water in the alkyl chain regions decreases by approximately 50% upon the addition of  $1 C_n\text{TMA}^+ / A_{\text{uc}}$ .

The alkyl chain length  $n$  of the  $C_n\text{TMA}^+$  ions considerably influences the structure of the assembled surfactant aggregates. As expected, the extension of the aggregates in the vertical direction increases with the alkyl chain length. The simulated monolayer aggregates exhibit thicknesses of 23 Å to 35 Å for  $C_{16}\text{TMA}^+$ , 18 Å to 25 Å for  $C_{12}\text{TMA}^+$ , and 13 Å to 17 Å for  $C_8\text{TMA}^+$ . Because the bilayer aggregates show a strong interdigitation, their thicknesses of 30 Å to 39 Å for  $C_{16}\text{TMA}^+$ , 23 Å to 36 Å for  $C_{12}\text{TMA}^+$ , and 20 Å to 23 Å for  $C_8\text{TMA}^+$  are only slightly increased. The fractions of gauche conformations of the alkyl chains of the aggregated  $C_n\text{TMA}^+$  ions increase with decreasing alkyl chain length. Furthermore, with decreasing chain length, increasing amounts of  $C_n\text{TMA}^+$  are desorbed from the aggregates. These desorbed surfactant ions reside as monomers in the solution or are located

at the water–vacuum interface. Thus, even though the number of adsorption complexes is independent of the alkyl chain length, the number of  $C_nTMA^+$  ions that are aggregated at the clay surface increases with increasing alkyl chain length. This observation is in excellent agreement with previous experiments (cf. [140]).

---

## Summary and Outlook

In this thesis, the molecular-scale structures of  $C_nTMA^+$  monolayer and bilayer aggregates assembled on Muscovite- and Montmorillonite-Water interfaces were characterized by means of classical Monte Carlo simulations.

### Structure of the Water Films

The simulation results for the inorganic montmorillonite- and muscovite-water systems indicate that the negatively charged phyllosilicate surfaces induce a layering of the adsorbed water films, which is extended over several molecular layers. This observation is in excellent agreement with previous experiments and simulation studies.

The structures of the adsorbed water films strongly depend on both the charge density of the mineral layers and the location of the charge substitutions within these layers. Other than charge substitutions of the tetrahedral sheets, charge substitutions of the octahedral sheets are located farther away from the mineral-water interface and are additionally shielded by a tetrahedral sheet. As a result, the effect of octahedral charge substitutions on the arrangement of water dipoles at the mineral surfaces and thus on the structures of the adsorbed water films is significantly smaller than that of tetrahedral substitutions.

In montmorillonite particles, the majority of the charge substitutions are located in the octahedral sheets, whereas the charge substitutions of muscovite are located exclusively in the tetrahedral sheets. Furthermore, muscovite exhibits an approximately 2.7-fold higher charge density of its mineral layers than montmorillonite. As a result, the binding of water molecules to the muscovite surface is considerably stronger. On muscovite, 1.3 water molecules per  $A_{uc}^1$  are doubly hydrogen-bonded to the mineral surface with  $z_{oxygen} \leq 2.2 \text{ \AA}$ . In contrast to this, only 0.1 such water molecules per  $A_{uc}$  were observed for montmorillonite.

### Adsorption of $C_nTMA^+$ Ions on Montmorillonite and Muscovite

The almost complete absence of water molecules that are doubly hydrogen-bonded to the montmorillonite surface leads to a considerably different adsorption behavior of  $C_nTMA^+$  ions on montmorillonite as compared to their adsorption on muscovite.

The simulation results indicate that on montmorillonite, approximately 90 % of the adsorbed  $C_nTMA^+$  ions form inner-sphere surface complexes, which displace water molecules from their adsorption positions on the mineral surface. In the lateral direction, the vast majority of these  $C_nTMA^+$  ions are adsorbed above the centers of ditrigonal cavities of the montmorillonite surface. Only a small fraction of approximately 10 % of the adsorbed  $C_nTMA^+$  ions forms outer-sphere complexes. The outer-sphere adsorbed ions show a comparatively high lateral mobility and do not exhibit specific lateral adsorption positions. The displacement of water molecules from their adsorption positions on the montmorillonite surface by the inner-sphere adsorption of  $C_nTMA^+$  ions results in a decrease of the density of the first water layer, which is characterized by  $z_{oxygen} \leq 4.7 \text{ \AA}$ , by approximately 70 % per  $C_nTMA^+ / A_{uc}$  added.

Those water molecules that are doubly hydrogen-bonded to muscovite are located above the ditrigonal cavities of the mineral surface. Thus, other than on montmorillonite, adsorbing  $C_nTMA^+$  ions have to overcome comparatively high

---

<sup>1</sup> $A_{uc}$  represents the area of a mineral surface that corresponds to the area of one unit cell in the crystallographic  $a$ - $b$  plane. Correspondingly,  $A_{uc} = 46.36 \text{ \AA}^2$  for montmorillonite and  $A_{uc} = 46.72 \text{ \AA}^2$  for muscovite (cf. section 3.2).



energy barriers to desorb these doubly hydrogen-bonded water molecules from the muscovite surface. As a consequence of this, the formation of  $C_nTMA^+$  inner-sphere surface complexes is impeded. Accordingly, more than 50 % of all  $C_nTMA^+$  adsorption complexes on muscovite were found to be outer-sphere ones. Furthermore, the structure of the first water layer adsorbed on the muscovite surface is notably less influenced by the adsorption of  $C_nTMA^+$  than that of the first water layer adsorbed on montmorillonite. The simulation results for the organically modified muscovite surface indicate that the ratio between the numbers of water molecules that are doubly ( $z_{\text{oxygen}} \leq 2.2 \text{ \AA}$ ) and singly ( $2.2 \leq z_{\text{oxygen}} \leq 3.3 \text{ \AA}$ ) hydrogen bonded to the mineral surface changes with increasing  $C_nTMA^+$  surface coverage. However, the average number of approximately 3.4 water molecules per  $A_{\text{uc}}$  that are either doubly or singly hydrogen-bonded to the muscovite surface is maintained.

### Structure of the $C_nTMA^+$ Aggregates

Up to simulated coverages of  $0.375 C_nTMA^+ / A_{\text{uc}}$ , the surfactant ions reside on the montmorillonite and the muscovite surfaces as monomers or dimers. At higher coverages, the surfactant ions form aggregates, which partially cover the mineral surfaces. The regions of hydrophobic alkyl chains and water are laterally separated from each other. The simulated bilayer aggregates show a strong interdigitation of the two opposing surfactant layers composing the aggregates. The densities of the interfacial water films in the vertical regions of the alkyl chains are decreased by approximately 50 % per  $C_nTMA^+ / A_{\text{uc}}$  added.

In the majority of the simulated systems, several  $C_nTMA^+$  ions are separated from the mineral surfaces by at least two interposed water layers. Even though being detached from the surfaces, most of these ions are yet part of the interfacial surfactant aggregates and bonded to them through hydrophobic interactions. At a given surfactant coverage, with increasing alkyl chain length, increasing amounts of  $C_nTMA^+$  are desorbed from the aggregates and reside in solution or at the water–vacuum interface. Accordingly, even though the numbers of formed adsorption complexes were found to be independent of the alkyl chain length, the amounts of  $C_nTMA^+$

that are aggregated at the mineral–water interfaces at given  $C_n\text{TMA}^+$  coverages increase with increasing alkyl chain length. The weaker hydrophobic interactions between short-chained  $C_n\text{TMA}^+$  ions are likewise reflected by the calculated gauche conformation fractions of the alkyl chains. In agreement with experiments of the self-assembly of dialkylammonium surfactants on mica, the conformational order of the alkyl chains of the aggregated  $C_n\text{TMA}^+$  ions considerably decreases with decreasing alkyl chain length.

The calculated aggregate thicknesses are in excellent agreement with available experimental data of  $C_n\text{TMA}^+$  aggregates formed on the cleaved muscovite surface. In general, the extensions in the  $z$ -direction of the monolayer and bilayer aggregates assembled on the external surface of montmorillonite are slightly smaller than those of the aggregates assembled on muscovite. This effect can be attributed to the significantly greater fraction of  $C_n\text{TMA}^+$  inner-sphere surface complexes formed on montmorillonite as compared to muscovite, resulting in a closer approach of the surfactant ions to the mineral surface.

### **Positions of the Inorganic Ions,**

#### **Adsorption of Cationic and Anionic Pollutants by Organoclays**

The simulation results indicate that the fractions of sodium and potassium cations that remain adsorbed on montmorillonite and muscovite, respectively, decrease with increasing amounts of adsorbed  $C_n\text{TMA}^+$ . However, in the vast majority of the simulated systems that show amounts of adsorbed  $C_n\text{TMA}^+$  exceeding the amount necessary to compensate the negative charge of the mineral surfaces, fractions of the inorganic surface cations remain adsorbed as inner-sphere surface complexes.

This incomplete desorption of inorganic surface cations agrees with the experimental observation that even those organoclays possess adsorption capacities for cationic pollutants, which exhibit uptakes of organic cations in excess of their cation exchange capacities. Cationic pollutants can hence be adsorbed by organically modified clay surfaces through their exchange with inorganic surface cations.

The excess positive charge at the mineral–aggregate interfaces is counterbalanced by chloride anions, which are mostly located in the regions around the hydrophilic  $C_n\text{TMA}^+$  headgroups and form ion pairs with both  $C_n\text{TMA}^+$  and inorganic surface cations. The adsorption of anionic pollutants on the external surfaces of organoclay particles can thus be attributed to their exchange with inorganic counterions (in the case of this study  $\text{Cl}^-$ ), which were co-adsorbed on the clay surfaces during the production of the organoclays.

### Outlook

With the MC simulation studies of this thesis, a significantly improved understanding of the molecular-scale structures of  $C_n\text{TMA}^+$  aggregates assembled on montmorillonite– and muscovite–water interfaces could be gained. Previous experiments revealed that  $C_{16}\text{TMA}^+$ ,  $\text{HDPy}^+$ , and  $\text{BE}^+$  modified bentonites show a pronounced anion selectivity with the affinity sequence being  $\text{ReO}_4^- > \text{I}^- > \text{Br}^- > \text{Cl}^- > \text{SO}_4^{2-} > \text{SeO}_3^{2-}$  (cf. [7]). This thesis may serve as a basis for future simulation studies investigating this still not well understood anion selectivity of organoclays.

Furthermore, for future simulation studies, the increase of the lateral dimensions of the simulation cells is desirable. Larger simulation cells will allow a better testing of the simulation results on the basis of experimental measurements. For example, the lateral structures of  $C_n\text{TMA}^+$  aggregates on a nanometer scale, which were observed in AFM experiments, cannot be represented by simulation cells having such small lateral extensions as used in this MC simulation study. Because the feasible system size is limited by current computer power, it is required to improve the employed Monte Carlo algorithms to increase the speed of system equilibration. This can for example be achieved by the implementation of cluster moves or the allowance of tunneling of inorganic ion pairs and water through hydrophobic aggregate regions.



# Bibliography

- [1] OECD/NEA. *Engineered barrier systems and the safety of deep geological repositories: State-of-the-art report EUR 19964 EN*. OECD Publications, Paris, 2003. ISBN 92-64-18498-8.
- [2] T. Brasser, H. J. Herbert, R. Mieke, and G. Schmidt. Anhang Wirtsgesteine: Potenzielle Wirtsgesteine und ihre Eigenschaften. In I. Müller-Lyda and M. Sailer, editors, *Endlagerung wärmeentwickelnder radioaktiver Abfälle in Deutschland*. GRS mbH and Öko-Institut e. V., 2008. ISBN 978-3-939355-22-9.
- [3] I. Müller-Lyda and M. Sailer, editors. *Endlagerung wärmeentwickelnder radioaktiver Abfälle in Deutschland*. GRS mbH and Öko-Institut e. V., 2008. ISBN 978-3-939355-22-9.
- [4] J. Bors, A. Gorny, and S. Dultz. Iodide, caesium and strontium adsorption by organophilic vermiculite. *Clay Miner.*, 32:21–28, 1997.
- [5] S. Dultz and J. Bors. Organophilic bentonites as adsorbents for radionuclides: II. Chemical and mineralogical properties of HDPy-montmorillonite. *Appl. Clay Sci.*, 16:15–29, 2000.
- [6] B. Riebe, J. Bors, and S. Dultz. Retardation capacity of organophilic bentonite for anionic fission products. *J. Contam. Hydrol.*, 47:255–264, 2001.
- [7] J. Behnsen and B. Riebe. Anion selectivity of organobentonites. *Appl. Geochem.*, 23:2746–2752, 2008.
- [8] B. Riebe, A. Meleshyn, S. Dultz, and B. Schampera. *Stabilität von Organotonen als Anionenadsorber unter Endlagerbedingungen – Experiment und Modellierung: Abschlussbericht zum BMWA-Projekt 02 E 10025*. Zentrum für Strahlenschutz und Radioökologie, Gottfried Wilhelm Leibniz Universität Hannover, 2009.
- [9] J. Bors. Sorption of radioiodine in organo-clays and soils. *Radiochim. Acta*, 51: 139–143, 1990.
- [10] J. Bors. Sorption and desorption of radioiodine on organo-clays. *Radiochim. Acta*, 58:235–235, 1992.
- [11] J. Bors and A. Gorny. Studies on the interactions of HDPY-vermiculite with radioiodine. *Appl. Clay Sci.*, 7:245–250, 1992.

- [12] J. Bors, S. Dultz, and B. Riebe. Retention of radionuclides by organophilic bentonite. *Eng. geol.*, 54:195–206, 1999.
- [13] J. Bors, S. Dultz, and B. Riebe. Organophilic bentonites as adsorbents for radionuclides: I. Adsorption of ionic fission products. *Appl. Clay Sci.*, 16:1–13, 2000.
- [14] J. Behnsen. *Anionenkonkurrenz und Anionenselektivität bei der Sorption von Radionukliden durch Organotone*. PhD thesis, Gottfried Wilhelm Leibniz Universität Hannover, 2007.
- [15] B. Schampera and S. Dultz. The effect of surface charge and wettability on H<sub>2</sub>O self diffusion in compacted clays. *Clays Clay Miner.*, 59:42–57, 2011.
- [16] B. Riebe, C. Bunnenberg, S. Dultz, and S. Gehrt. *Einsatz von Organotonen als Adsorber für problematische Anionen in geotechnischen Barrieren: Abschlussbericht zum BMWA-Projekt 02 E 9481*. Zentrum für Strahlenschutz und Radioökologie, Universität Hannover, 2005.
- [17] S. Dultz, B. Riebe, and C. Bunnenberg. Temperature effects on iodine adsorption on organo-clay minerals: II. Structural effects. *Appl. Clay Sci.*, 28:17–30, 2005.
- [18] B. Riebe, S. Dultz, and C. Bunnenberg. Temperature effects on iodine adsorption on organo-clay minerals: I. Influence of pretreatment and adsorption temperature. *Appl. Clay Sci.*, 28:9–16, 2005.
- [19] B. Riebe and C. Bunnenberg. Influence of temperature pre-treatment and high-molar saline solutions on the adsorption capacity of organo-clay minerals. *Phys. Chem. Earth*, 32:581–587, 2007.
- [20] A. Meleshyn and B. Riebe. Thermal stability of organoclays: Effects of duration and atmosphere of isothermal heating on iodide sorption. *Environ. Sci. Technol.*, 44:9311–9317, 2010.
- [21] F. Jeschke. *Einfluss von Gamma-Strahlung auf die Sorptionsfähigkeit von Organotonen für Iod*. Diploma Thesis, Zentrum für Strahlenschutz und Radioökologie, Leibniz Universität Hannover, 2007.
- [22] A. Meleshyn. *Monte Carlo Simulationen zur Untersuchung von Quell- und Sorptionsprozessen in Wyoming-Montmorillonit im Hinblick auf seine Verwendung als Barrierematerial in Endlagern für radioaktive Abfälle*. PhD thesis, Universität Hannover, 2005.
- [23] A. Meleshyn and C. Bunnenberg. Swelling of Na/Mg-montmorillonites and hydration of interlayer cations: A Monte Carlo study. *J. Chem. Phys.*, 123:074706, 2005.

- [24] A. Meleshyn and C. Bunnenberg. The gap between crystalline and osmotic swelling of Na-montmorillonite: A Monte Carlo study. *J. Chem. Phys.*, 122:034705, 2005.
- [25] A. Meleshyn and C. Bunnenberg. Interlayer expansion and mechanisms of anion sorption of Na-montmorillonite modified by cetylpyridinium chloride: A Monte Carlo study. *J. Phys. Chem. B*, 110:2271–2277, 2006.
- [26] A. Meleshyn. Aqueous solution structure at the cleaved mica surface: Influence of  $K^+$ ,  $H_3O^+$ , and  $Cs^+$  adsorption. *J. Phys. Chem. C*, 112:20018–20026, 2008.
- [27] A. Meleshyn. Two-dimensional ordering of water adsorbed on a mica surface at room temperature. *J. Phys. Chem. C*, 112:14495–14500, 2008.
- [28] A. Meleshyn. Cetylpyridinium aggregates at the montmorillonite– and muscovite–water interfaces: a Monte Carlo study of surface charge effect. *Langmuir*, 25:6250–6259, 2009.
- [29] A. Meleshyn. Cetylpyridinium chloride at the mica–water interface: incomplete monolayer and bilayer structures. *Langmuir*, 25:881–890, 2009.
- [30] A. Meleshyn. Potential of mean force for  $Mg^{2+}$  at the cleaved mica–water interface. *J. Phys. Chem. C*, 113:12946–12949, 2009.
- [31] A. Meleshyn. Potential of mean force for  $Ca^{2+}$  at the cleaved mica–water interface. *J. Phys. Chem. C*, 113:17604–17607, 2009.
- [32] A. Meleshyn. Adsorption of  $Sr^{2+}$  and  $Ba^{2+}$  at the cleaved mica–water interface: Free energy profiles and interfacial structure. *Geochim. Cosmochim. Acta*, 74:1485–1497, 2010.
- [33] A. Meleshyn. Potential of mean force for  $K^+$  in thin water films on cleaved mica. *Langmuir*, 26:13081–13085, 2010.
- [34] A. Meleshyn and D. Tunega. Adsorption of phenanthrene on Na-montmorillonite: A model study. *Geoderma*, In Press, Corrected Proof, 2010.
- [35] F. Jeschke and A. Meleshyn. A Monte Carlo study of interlayer and surface structures of tetraphenylphosphonium-modified Na-montmorillonite. *Geoderma*, In Press, Corrected Proof, 2010.
- [36] H. Wicke and A. Meleshyn. Microhydration of the Selenite Dianion: A Theoretical Study of Structures, Hydration Energies, and Electronic Stabilities of  $SeO_3^{2-}(H_2O)_n$  ( $n = 0-6, 9$ ) Clusters. *J. Phys. Chem. A*, 114:8948–8960, 2010.
- [37] H. Wicke. *Quantum chemical and classical molecular dynamics studies of molecular ions relevant for final nuclear waste disposal*. PhD thesis, Gottfried Wilhelm Leibniz Universität Hannover, 2011.

- [38] Bundesministerium für Umwelt, Naturschutz und Reaktorsicherheit. *Sicherheitsanforderungen an die Endlagerung wärmeentwickelnder radioaktiver Abfälle*. BMU, Stand 30. September 2010.
- [39] International Atomic Energy Agency. *Classification of radioactive waste: A safety guide*. International Atomic Energy Agency, Vienna, 1994. ISBN 92-0-101194-6.
- [40] *Gesetz über die friedliche Verwendung der Kernenergie und den Schutz gegen ihre Gefahren (Atomgesetz - AtG) vom 23. Dezember 1959, Neufassung vom 15. Juli 1985 (BGBl.I 1985, Nr. 41, S. 1565), zuletzt geändert durch Artikel 4 des Gesetzes vom 8. November 2011 (BGBl.I 2011, Nr. 57, S. 2198)*.
- [41] Bundesamt für Strahlenschutz (BfS). *Safety codes and guides-translations – Edition 08/11: Act on the Peaceful Utilisation of Atomic Energy and the Protection against its Hazards (Atomic Energy Act)*. last amendment by the Act of 31 July 2011.
- [42] Bundesministerium für Umwelt, Naturschutz und Reaktorsicherheit. *Safety Requirements Governing the Final Disposal of Heat-Generating Radioactive Waste*. BMU, Stand 30. September 2010.
- [43] Reaktor-Sicherheitskommission and Strahlenschutzkommission. *Gemeinsame Stellungnahme der RSK und der SSK zum GRS-Bericht "Sicherheitsanforderungen an die Endlagerung hochradioaktiver Abfälle in tiefen geologischen Formationen": Stellungnahme der Strahlenschutzkommission und der Reaktor-Sicherheitskommission*. verabschiedet von der RSK auf ihrer 408. Sitzung am 09.05.2008, verabschiedet von der SSK auf ihrer 224. Sitzung am 03.07.2008.
- [44] Entsorgungskommission (ESK). *Stellungnahme zum Entwurf des BMU "Sicherheitsanforderungen an die Endlagerung wärmeentwickelnder radioaktiver Abfälle"*. 29.01.2009.
- [45] F. T. Madsen. Clay mineralogical investigations related to nuclear waste disposal. *Clay Miner.*, 33:109–129, 1998.
- [46] A. Meunier. Why are clay minerals small? *Clay Miner.*, 41:551–566, 2006.
- [47] E. S. Boek, P. V. Coveney, and N. T. Skipper. Monte Carlo molecular modeling studies of hydrated Li-, Na-, and K-smectites: Understanding the role of potassium as a clay swelling inhibitor. *J. Am. Chem. Soc.*, 117:12608–12617, 1995.
- [48] G. Jörg, R. Bühnemann, S. Hollas, N. Kivel, K. Kossert, S. van Winckel, and C. L. v. Gostomski. Preparation of radiochemically pure  $^{79}\text{Se}$  and highly precise determination of its half-life. *Applied Radiation and Isotopes*, 68:2339–2351, 2010.
- [49] P. Bienvenu, P. Cassete, G. Andreoletti, M. Be, J. Compte, and M. Lepy. A new determination of  $^{79}\text{Se}$  half-life. *Applied Radiation and Isotopes*, 65:355–364, 2007.



- [50] Nagra. *Technical report 02-05: Project Opalinus clay, safety report, demonstration of disposal feasibility for spent fuel, vitrified high-level waste and long-lived intermediate-level waste (Entsorgungsnachweis)*. Nagra, Wettingen (Switzerland), 2002.
- [51] S. Kaufhold, M. Pohlmann-Lortz, R. Dohrmann, and R. Nüesch. About the possible upgrade of bentonite with respect to iodide retention capacity. *Appl. Clay Sci.*, 35:39–46, 2007.
- [52] S. Xu and S. A. Boyd. Cationic surfactant sorption to a vermiculitic subsoil via hydrophobic bonding. *Environ. Sci. Technol.*, 29:312–320, 1995.
- [53] Y. L. Chen, S. Chen, C. Frank, and J. N. Israelachvili. Molecular mechanisms and kinetics during the self-assembly of surfactant layers. *J. Colloid Interface Sci.*, 153:244–265, 1992.
- [54] L. B. de Paiva, A. R. Morales, and F. R. Valenzuela Díaz. Organoclays: Properties, preparation and applications. *Appl. Clay Sci.*, 42:8–24, 2008.
- [55] S. A. Boyd, M. M. Mortland, and C. T. Chiou. Sorption characteristics of organic compounds on hexadecyltrimethylammonium-smectite. *Soil Sci. Soc. Am. J.*, 52:652–657, 1988.
- [56] M. J. Carrizosa, W. C. Koskinen, and M. C. Hermosín. Interactions of acidic herbicides bentazon and dicamba with organoclays. *Soil Sci. Soc. Am. J.*, 68:1863–1866, 2004.
- [57] J. L. Suter, P. V. Coveney, H. C Greenwell, and M. A. Thyveetil. Large-scale molecular dynamics study of montmorillonite clay: Emergence of undulatory fluctuations and determination of material properties. *J. Phys. Chem. C*, 111:8248–8259, 2007.
- [58] E. S. Boek, P. V. Coveney, and N. T. Skipper. Molecular modeling of clay hydration: A study of hysteresis loops in the swelling curves of sodium montmorillonites. *Langmuir*, 11:4629–4631, 1995.
- [59] N. T. Skipper, G. Sposito, and F. R. C. Chang. Monte Carlo simulation of inter-layer molecular structure in swelling clay minerals; 2, Monolayer hydrates. *Clays Clay Miner.*, 43:294–303, 1995.
- [60] G. Kosakowski, S. V. Churakov, and T. Thoenen. Diffusion of Na and Cs in montmorillonite. *Clays Clay Miner.*, 56:190–206, 2008.
- [61] J. O. Titiloye and N. T. Skipper. Computer simulation of the structure and dynamics of methane in hydrated Na-smectite clay. *Chem. Phys. Lett.*, 329:23–28, 2000.
- [62] G. D. Williams, A. K. Soper, N. T. Skipper, and M. V. Smalley. High-resolution structural study of an electrical double layer by neutron diffraction. *J. Phys. Chem. B*, 102:8945–8949, 1998.

- [63] Q. H. Zeng, A. B. Yu, G. Q. Lu, and R. K. Standish. Molecular dynamics simulation of the structural and dynamic properties of dioctadecyldimethyl ammoniums in organoclays. *J. Phys. Chem. B*, 108:10025–10033, 2004.
- [64] H. He, J. Galy, and J. F. Gérard. Molecular simulation of the interlayer structure and the mobility of alkyl chains in HDTMA<sup>+</sup>/montmorillonite hybrids. *J. Phys. Chem. B*, 109:13301–13306, 2005.
- [65] T. J. Tambach, E. S. Boek, and B. Smit. Molecular order and disorder of surfactants in clay nanocomposites. *Phys. Chem. Chem. Phys.*, 8:2700–2702, 2006.
- [66] S. H. Park and G. Sposito. Structure of water adsorbed on a mica surface. *Phys. Rev. Lett.*, 89:085501, 2002.
- [67] J. Wang, A. G. Kalinichev, R. J. Kirkpatrick, and R. T. Cygan. Structure, energetics, and dynamics of water adsorbed on the muscovite (001) surface: A molecular dynamics simulation. *J. Phys. Chem. B*, 109:15893–15905, 2005.
- [68] J. A. Greathouse and R. T. Cygan. Water structure and aqueous uranyl(VI) adsorption equilibria onto external surfaces of beidellite, montmorillonite, and pyrophyllite: Results from molecular simulations. *Environ. Sci. Technol.*, 40:3865–3871, 2006.
- [69] V. Marry, B. Rotenberg, and P. Turq. Structure and dynamics of water at a clay surface from molecular dynamics simulation. *Phys. Chem. Chem. Phys.*, 10:4802–4813, 2008.
- [70] S. S. Lee, P. A. Fenter, C. Park, N. C. Sturchio, and K. L. Nagy. Hydrated cation speciation at the muscovite (001) – water interface. *Langmuir*, 26:16647–16651, 2010.
- [71] S. Bandyopadhyay, J. C. Shelley, M. Tarek, P. B. Moore, and M. L. Klein. Surfactant aggregation at a hydrophobic surface. *J. Phys. Chem. B*, 102:6318–6322, 1998.
- [72] H. Heinz, H. J. Castelijns, and U. W. Suter. Structure and phase transitions of alkyl chains on mica. *J. Am. Chem. Soc.*, 125:9500–9510, 2003.
- [73] N. Metropolis, A. W. Rosenbluth, M. N. Rosenbluth, A. H. Teller, and E. Teller. Equation of state calculations by fast computing machines. *J. Chem. Phys.*, 21:1087, 1953.
- [74] T. J. H. Vlugt, M. G. Martin, B. Smit, J. I. Siepmann, and R. Krishna. Improving the efficiency of the configurational-bias Monte Carlo algorithm. *Mol. Phys.*, 94:727–733, 1998.
- [75] D. Frenkel and B. Smit. *Understanding molecular simulation: From algorithms to applications*. Acad. Press, San Diego (CA), 2nd edition, 2002. ISBN 0-12-267351-4.

- [76] N. T. Skipper. Monte Carlo and molecular dynamics computer simulation of aqueous interlayer fluids in clays. In J. D. Kubicki and W. F. Bleam, editors, *Molecular modeling of clays and mineral surfaces*, volume 12, pages 101–142. Clay Minerals Society, Aurora and Colo, 2003. ISBN 1-881208-11-7.
- [77] M. P. Allen and D. J. Tildesley. *Computer Simulation of Liquids*. Oxford University Press, New York, 1989. ISBN 0-19-855645-4.
- [78] W. A. Hayes and D. K. Schwartz. Two-stage growth of octadecyltrimethylammonium bromide monolayers at mica from aqueous solution below the Krafft point. *Langmuir*, 14:5913–5917, 1998.
- [79] J. M. Mellott, W. A. Hayes, and D. K. Schwartz. Kinetics of octadecyltrimethylammonium bromide self-assembled monolayer growth at mica from an aqueous solution. *Langmuir*, 20:2341–2348, 2004.
- [80] N. Metropolis and S. Ulam. The Monte Carlo method. *Journal of the American Statistical Association*, 44:335–341, 1949.
- [81] S. Ulam, R. D. Richtmyer, and J. Neumann. Statistical methods in neutron diffusion. *Los Alamos Scientific Laboratory Report LAMS-551*, pages 1–22, 1947.
- [82] N. Metropolis. The beginning of the Monte Carlo method. *Los Alamos Science*, 15:125–130, 1987.
- [83] V. I. Manousiouthakis and M. W. Deem. Strict detailed balance is unnecessary in Monte Carlo simulation. *J. Chem. Phys.*, 110:2753, 1999.
- [84] M. N. Rosenbluth and A. W. Rosenbluth. Monte Carlo calculation of the average extension of molecular chains. *J. Chem. Phys.*, 23:356, 1955.
- [85] W. L. Jorgensen, D. S. Maxwell, and J. Tirado-Rives. Development and testing of the OPLS All-Atom force field on conformational energetics and properties of organic liquids. *J. Am. Chem. Soc.*, 118:11225–11236, 1996.
- [86] W. L. Jorgensen, J. Chandrasekhar, J. D. Madura, R. W. Impey, and M. L. Klein. Comparison of simple potential functions for simulating liquid water. *J. Chem. Phys.*, 79:926–935, 1983.
- [87] J. Chandrasekhar, D. C. Spellmeyer, and W. L. Jorgensen. Energy component analysis for dilute aqueous solutions of  $\text{Li}^+$ ,  $\text{Na}^+$ ,  $\text{F}^-$ , and  $\text{Cl}^-$  ions. *J. Am. Chem. Soc.*, 106:903–910, 1984.
- [88] W. L. Jorgensen and J. Gao. Monte Carlo simulations of the hydration of ammonium and carboxylate ions. *J. Phys. Chem.*, 90:2174–2182, 1986.
- [89] J. Aqvist. Ion-water interaction potentials derived from free energy perturbation simulations. *J. Phys. Chem.*, 94:8021–8024, 1990.

- [90] R. C. Rizzo and W. L. Jorgensen. OPLS All-Atom model for amines: Resolution of the amine hydration problem. *J. Am. Chem. Soc.*, 121:4827–4836, 1999.
- [91] M. L. P. Price, D. Ostrovsky, and W. L. Jorgensen. Gas-phase and liquid-state properties of esters, nitriles, and nitro compounds with the OPLS-AA force field. *J. Comput. Chem.*, 22:1340–1352, 2001.
- [92] N. T. Skipper, F. R. C. Chang, and G. Sposito. Monte Carlo simulation of interlayer molecular structure in swelling clay minerals; 1. Methodology. *Clays Clay Miner.*, 43:285–293, 1995.
- [93] P. P. Ewald. Die Berechnung optischer und elektrostatischer Gitterpotentiale. *Ann. Phys.*, 369:253–287, 1921.
- [94] I. C. Yeh and M. L. Berkowitz. Ewald summation for systems with slab geometry. *J. Chem. Phys.*, 111:3155–3162, 1999.
- [95] S. I. Tsipursky and V. A. Drits. The distribution of octahedral cations in the 2:1 layers of dioctahedral smectites studied by oblique-texture electron diffraction. *Clay Miner.*, 19:177–193, 1984.
- [96] A. C. D. Newman. *Chemistry of clays and clay minerals*. Longman Scientific & Technical, Harlow, 1990. ISBN 0-582-30114-9.
- [97] M. Müller-Vonmoos and G. Kahr. *Mineralogische Untersuchungen von Wyoming-Bentonit MX-80 und Montigel*. Technischer Bericht. Nagra, 1983.
- [98] B. B. Smoliar-Zviagina. Relationships between structural parameters and chemical composition of micas. *Clay Miner.*, 28:603–624, 1993.
- [99] J. Zhu, L. Zhu, R. Zhu, S. Tian, and J. Li. Surface microtopography of surfactant modified montmorillonite. *Appl. Clay Sci.*, 45:70–75, 2009.
- [100] W. Loewenstein. The distribution of aluminum in the tetrahedra of silicates and aluminates. *Am. Mineral.*, 39:92–96, 1954.
- [101] M. L. Schlegel, K. L. Nagy, P. A. Fenter, L. Cheng, N. C. Sturchio, and S. D. Jacobsen. Cation sorption on the muscovite (001) surface in chloride solutions using high-resolution X-ray reflectivity. *Geochim. Cosmochim. Acta*, 70:3549–3565, 2006.
- [102] A. R. Campanelli and L. Scaramuzza. Hexadecyltrimethylammonium bromide. *Acta Crystallogr., Sect. C*, 42:1380–1383, 1986.
- [103] H. Wicke. Private Communication. 2009.
- [104] M. W. Schmidt, K. K. Baldridge, J. A. Boatz, S. T. Elbert, M. S. Gordon, J. H. Jensen, S. Koseki, N. Matsunaga, K. A. Nguyen, S. Su, T. L. Windus, M. Dupuis, and J. A. Montgomery. General atomic and molecular electronic structure system. *J. Comput. Chem.*, 14:1347–1363, 1993.

- [105] M. S. Gordon and M. W. Schmidt. Advances in electronic structure theory: GAMESS a decade later. In *Theory and Applications of Computational Chemistry*, pages 1167–1189. Elsevier, Amsterdam and Boston, 2005. ISBN 0444517197.
- [106] A. D. Becke. Density-functional thermochemistry. III. The role of exact exchange. *J. Chem. Phys.*, 98:5648–5652, 1993.
- [107] P. J. Stephens, F. J. Devlin, C. F. Chabalowski, and M. J. Frisch. Ab initio calculation of vibrational absorption and circular dichroism spectra using density functional force fields. *J. Phys. Chem.*, 98:11623–11627, 1994.
- [108] R. H. Hertwig and W. Koch. On the parameterization of the local correlation functional. What is Becke-3-LYP? *Chem. Phys. Lett.*, 268:345–351, 1997.
- [109] S.H Vosko, L. Wilk, and M. Nusair. Accurate spin-dependent electron liquid correlation energies for local spin density calculations: a critical analysis. *Can. J. Phys.*, 58:1200–1211, 1980.
- [110] F. Weigend and R. Ahlrichs. Balanced basis sets of split valence, triple zeta valence and quadruple zeta valence quality for H to Rn: Design and assessment of accuracy. *Phys. Chem. Chem. Phys.*, 7:3297–3305, 2005.
- [111] R. S. Mulliken. Electronic Population Analysis on LCAO-MO Molecular Wave Functions. I. *J. Chem. Phys.*, 23:1833, 1955.
- [112] R. S. Mulliken. Electronic Population Analysis on LCAO-MO Molecular Wave Functions. II. Overlap Populations, Bond Orders, and Covalent Bond Energies. *J. Chem. Phys.*, 23:1841, 1955.
- [113] R. S. Mulliken. Electronic Population Analysis on LCAO-MO Molecular Wave Functions. III. Effects of Hybridization on Overlap and Gross AO Populations. *J. Chem. Phys.*, 23:2338, 1955.
- [114] R. S. Mulliken. Electronic Population Analysis on LCAO-MO Molecular Wave Functions. IV. Bonding and Antibonding in LCAO and Valence-Bond Theories. *J. Chem. Phys.*, 23:2343, 1955.
- [115] P. D. T. Huibers. Quantum-chemical calculations of the charge distribution in ionic surfactants. *Langmuir*, 15:7546–7550, 1999.
- [116] B. Minisini, S. Chavand, R. Barthelery, and F. Tsobnang. Calculations of the charge distribution in dodecyltrimethylammonium: a quantum chemical investigation. *J. Mol. Model.*, 16:1085–1092, 2010.
- [117] L. Cheng, P. A. Fenter, K. L. Nagy, M. L. Schlegel, and N. C. Sturchio. Molecular-scale density oscillations in water adjacent to a mica surface. *Phys. Rev. Lett.*, 87:156103, 2001.

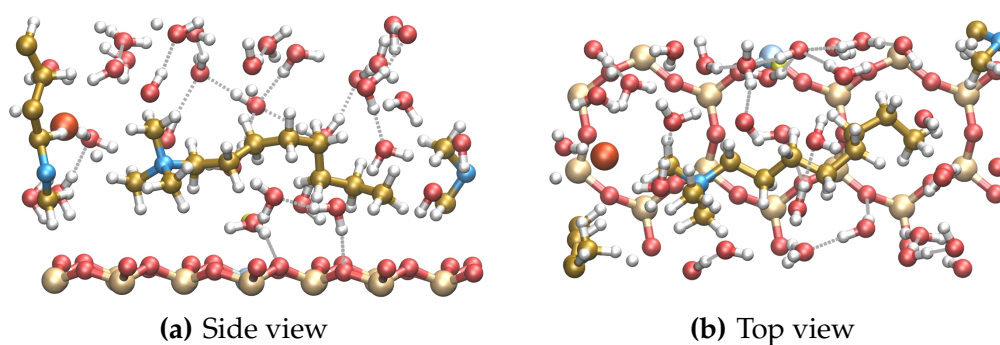
- [118] J. N. Israelachvili, R. M. Pashley, E. Perez, and R. K. Tandon. Forces between hydrophobic surfaces in aqueous electrolyte and surfactant solutions containing common air-borne impurities. *Colloids Surf.*, 2:277–285, 1981.
- [119] P. Kékicheff, H. K. Christenson, and B. W. Ninham. Adsorption of cetyltrimethylammonium bromide to mica surfaces below the critical micellar concentration. *Colloids Surf.*, 40:31–41, 1989.
- [120] D. Brovelli, W. R. Caseri, and G. Hähner. Self-assembled monolayers of alkylammonium ions on mica: Direct determination of the orientation of the alkyl chains. *J. Colloid Interface Sci.*, 216:418–423, 1999.
- [121] S. Manne and H. E. Gaub. Molecular organization of surfactants at solid-liquid interfaces. *Science*, 270:1480–1482, 1995.
- [122] R. E. Lamont and W. A. Ducker. Surface-induced transformations for surfactant aggregates. *J. Am. Chem. Soc.*, 120:7602–7607, 1998.
- [123] W. A. Ducker and E. J. Wanless. Adsorption of hexadecyltrimethylammonium bromide to mica: nanometer-scale study of binding-site competition effects. *Langmuir*, 15:160–168, 1999.
- [124] J. F. Liu and W. A. Ducker. Surface-induced phase behavior of alkyltrimethylammonium bromide surfactants adsorbed to mica, silica, and graphite. *J. Phys. Chem. B*, 103:8558–8567, 1999.
- [125] G. G. Warr. Surfactant adsorbed layer structure at solid/solution interfaces: impact and implications of AFM imaging studies. *Curr. Opin. Colloid Interface Sci.*, 5:88–94, 2000.
- [126] R. Atkin. Mechanism of cationic surfactant adsorption at the solid–aqueous interface. *Adv. Colloid Interface Sci.*, 103:219–304, 2003.
- [127] M. A. Osman, M. Ernst, B. H. Meier, and U. W. Suter. Structure and molecular dynamics of alkane monolayers self-assembled on mica platelets. *J. Phys. Chem. B*, 106:653–662, 2002.
- [128] G. Hähner, M. Zwahlen, and W. R. Caseri. Chain-length dependence of the conformational order in self-assembled dialkylammonium monolayers on mica studied with soft X-ray absorption. *Langmuir*, 21:1424–1427, 2005.
- [129] Y. L. E. Chen, M. L. Gee, C. A. Helm, J. N. Israelachvili, and P. M. McGuiggan. Effects of humidity on the structure and adhesion of amphiphilic monolayers on mica. *J. Phys. Chem.*, 93:7057–7059, 1989.
- [130] G. Fragneto, R. K. Thomas, A. R. Rennie, and J. Penfold. Neutron reflection from hexadecyltrimethylammonium bromide adsorbed on smooth and rough silicon surfaces. *Langmuir*, 12:6036–6043, 1996.

- [131] G. Sposito, N. T. Skipper, R. Sutton, S. H. Park, A. K. Soper, and J. A. Greathouse. Surface geochemistry of the clay minerals. *Proc. Natl. Acad. Sci. U. S. A.*, 96:3358–3364, 1999.
- [132] Z. Wang and R G. Larson. Molecular dynamics simulations of threadlike cetyltrimethylammonium chloride micelles: effects of sodium chloride and sodium salicylate salts. *J. Phys. Chem. B*, 113:13697–13710, 2009.
- [133] M. Fujii, B. Li, K. Fukada, T. Kato, and T. Seimiya. Two-dimensional arrangements of adsorbed alkylammonium halides on cleaved mica surface. *Langmuir*, 17:1138–1142, 2001.
- [134] A. E. Smith. The crystal structure of the normal paraffin hydrocarbons. *J. Chem. Phys.*, 21:2229, 1953.
- [135] M. A. Osman, G. Seyfang, and U. W. Suter. Two-dimensional melting of alkane monolayers ionically bonded to mica. *J. Phys. Chem. B*, 104:4433–4439, 2000.
- [136] P. G. Slade and W. P. Gates. The swelling of HDTMA smectites as influenced by their preparation and layer charges. *Appl. Clay Sci.*, 25:93–101, 2004.
- [137] P. G. Slade and W. P. Gates. HDTMA in the interlayers of high-charged Llano vermiculite. *Clays Clay Miner.*, 55:131–139, 2007.
- [138] B. Rotenberg, V. Marry, N. Malikova, and P. Turq. Molecular simulation of aqueous solutions at clay surfaces. *J. Phys.: Condens. Matter*, 22:284114, 2010.
- [139] S. Y. Lee and S. J. Kim. Dehydration behaviour of hexadecyltrimethylammonium-exchanged smectite. *Clay Miner.*, 38:225–232, 2003.
- [140] R. Atkin, V. S. J. Craig, E. J. Wanless, and S. Biggs. The influence of chain length and electrolyte on the adsorption kinetics of cationic surfactants at the silica–aqueous solution interface. *J. Colloid Interface Sci.*, 266:236–244, 2003.
- [141] S. Kimball, P. Mattis, et al. GIMP - GNU Image Manipulation Program, 2008. URL <http://www.gimp.org>.
- [142] G. Schaftenaar and J. H. Noordik. Molden: a pre- and post-processing program for molecular and electronic structures. *J. Comput.-Aided Mol. Design*, 14:123–134, 2000.
- [143] Persistence of Vision Pty. Ltd. Persistence of Vision (TM) Raytracer (Version 3.6), 2004. URL <http://www.povray.org/download/>.
- [144] W. Humphrey, A. Dalke, and K. Schulten. VMD – Visual Molecular Dynamics. *Journal of Molecular Graphics*, 14:33–38, 1996.
- [145] H. B. Bröker, E. A Merritt, et al. Gnuplot 4.4, 2010. URL <http://www.gnuplot.info>.

- [146] L. Lamport. *LATEX: A Document Preparation System*. Addison-Wesley, Massachusetts, second edition, 1994.



---

**Extended Figures**

**Figure A.1** – (a) Side view and (b) top view of a  $C_8TMA^+$  ion adsorbed parallel to the montmorillonite surface. (a) and (b) are snapshots of the simulated equilibrium configuration for the monolayer arrangement at a coverage of  $0.75 C_8TMA^+ / A_{uc}$ . Ball and stick colors: beige (Si), gray-blue (Al), red (O), white (H), blue (N), brown (C), red ( $Cl^-$ ).

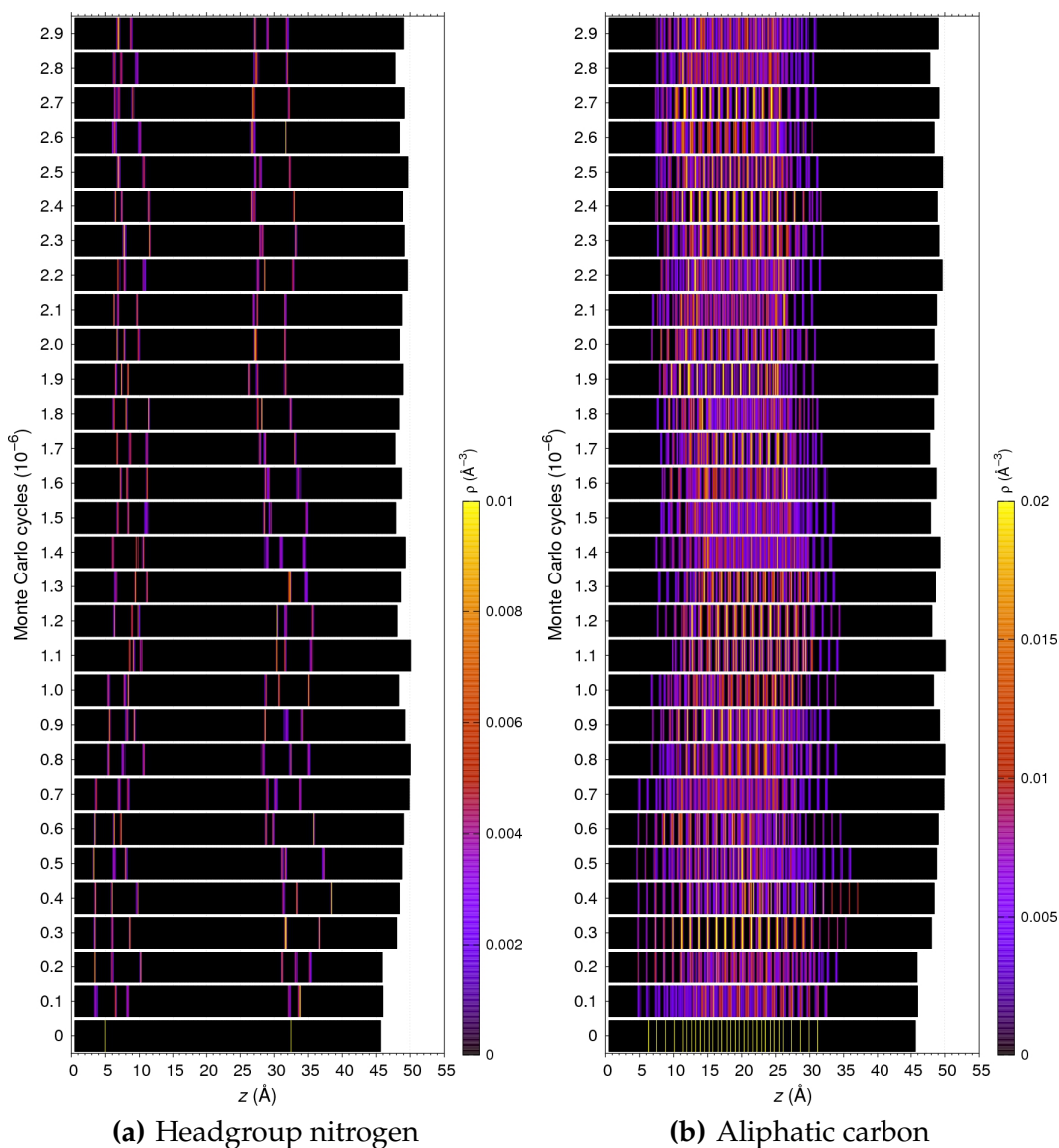


**Figure A.2** – Vertical atomic density profiles for (a) headgroup nitrogen and (b) aliphatic carbon atoms of  $C_{16}TMA^+$  as functions of the distance  $z$  from the muscovite surface for the bilayer arrangement at a coverage of  $0.75 C_{16}TMA^+ / A_{uc}$ . The graphs show the evolution of the atomic densities of the system with simulation time. The density profiles were sampled every 100 000 MC cycles over 100 MC cycles. The extension of the water film between the muscovite–water interface ( $z = 0 \text{ \AA}$ ) and the water–vacuum interface is indicated by black bars.

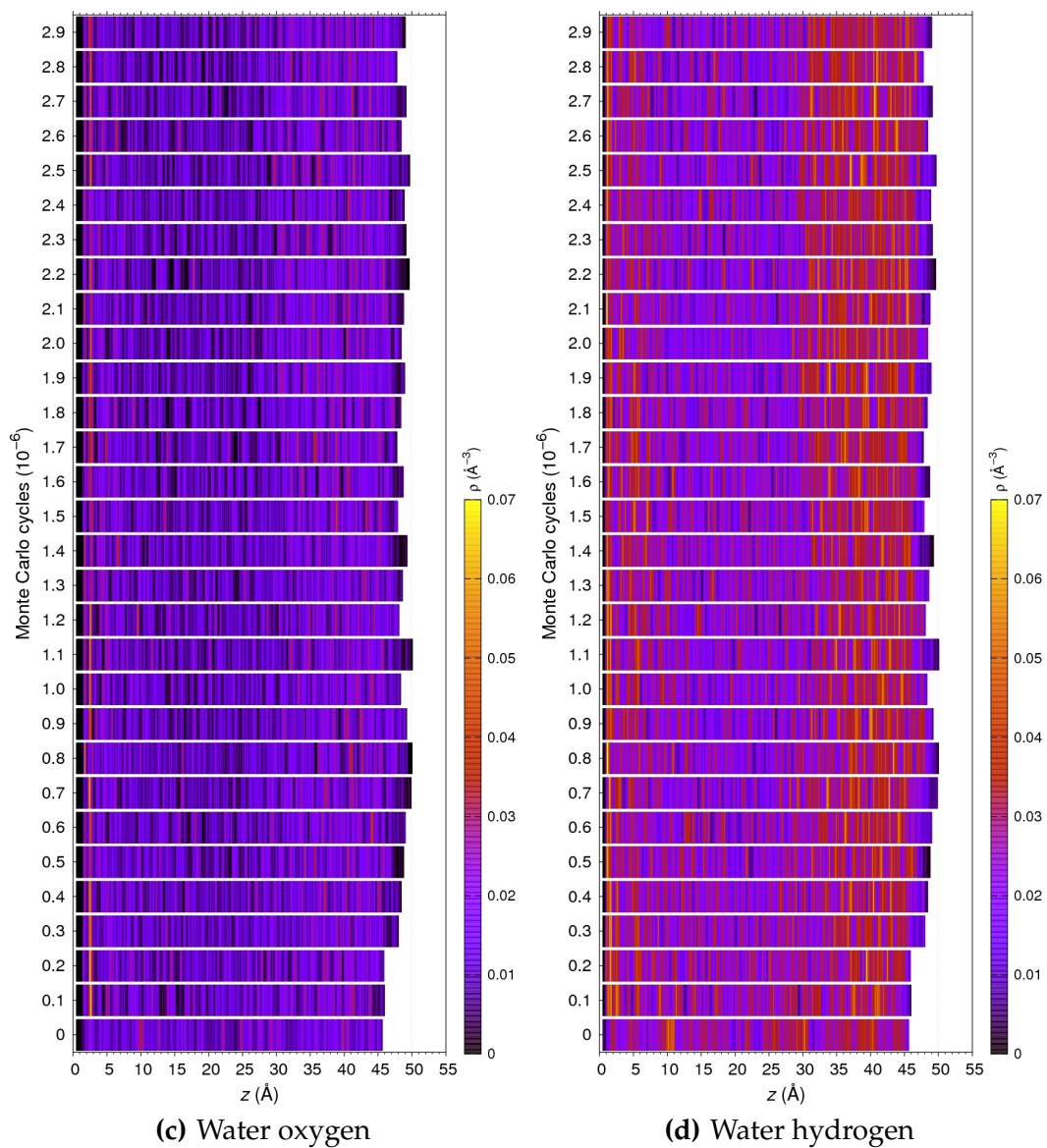


**Figure A.2** – continued. Vertical atomic density profiles for water (a) oxygen and (b) hydrogen atoms for the bilayer arrangement at a coverage of  $0.75 C_{16}TMA^+ / A_{uc}$  as functions of the distance  $z$  from the muscovite surface.



---

## Used Software

**Table B.1** – Software employed for the calculations of this work.

Purpose	Software
Monte Carlo simulations	mclay [22]
Calculation of the energetically optimized geometries and the partial atomic charges of $C_nTMA^+$	GAMESS-US [104, 105]
Programming language used for data analysis	Fortran 95

**Table B.2** – Software employed for the creation of figures and typesetting.

Purpose	Software
Visualization of atoms and molecules	GIMP 2.6.11 [141] MOLDEN 5.0 [142] POV-Ray 3.6[143] VMD 1.8.7 [144]
Data plots	gnuplot 4.4 [145]
Typesetting	$\LaTeX 2_\epsilon$ [146]



# Curriculum Vitae

## Personal Details

Full Name: Birthe Klebow  
Date of Birth: 24 February 1983  
Place of Birth: Uelzen

## Education

Since 05/08 Scientific assistant and PhD student  
*Institute of Radioecology and Radiation Protection,  
Leibniz Universität Hannover*

09/07 – 02/08 Stipendiary in the program  
“International Understanding at School”  
administered by the Robert Bosch Foundation  
*Gymnázium Na Pražáčce, Prague, Czech Republic*

2002 – 2007 Erste Staatsprüfung für das Lehramt an Gymnasien  
Thesis: Zur Modellierung nichtlinearer funktionaler  
Zusammenhänge  
*Leibniz Universität Hannover*

1995 – 2002 Abitur  
*Herzog-Ernst Gymnasium Uelzen*





## Scientific Publications and Presentations

B. Klebow and A. Meleshyn. Aggregation of Alkyltrimethylammonium Ions at the Cleaved Muscovite Mica–Water Interface: A Monte Carlo Study. *Langmuir*, 27: 12968-12976, 2011.

B. Klebow and A. Meleshyn. Monte-Carlo-Untersuchungen zur Struktur von Alkyltrimethylammonium-Aggregaten an der Grenzfläche zwischen Montmorillonit und Wasser. Talk at *GDCh-Wissenschaftsforum Chemie 2011*, Bremen, Germany, Sept. 04 – 09, 2011.

B. Klebow and A. Meleshyn. Monte Carlo Study of the Aggregation of Alkyltrimethylammonium Ions at the Montmorillonite–Water Interface. Talk at *Goldschmidt 2011*, Prague, Czech Republic, Aug. 14 – 19, 2011.

B. Klebow and A. Meleshyn. Monte Carlo Study of Alkyltrimethylammonium Monolayer and Bilayer Aggregates at the Muscovite–Water Interface. Poster presentation at *Clays in Natural & Engineered Barriers for Radioactive Waste Confinement, 4th international meeting*, Nantes, France, Mar. 29 – Apr. 01, 2010.

B. Klebow and A. Meleshyn. Adsorption of Alkyltrimethylammonium Surfactants on Muscovite Mica – A Monte Carlo Study. Talk at *DFG-IUSS Symposium on Advances of Molecular Modeling of Biogeochemical Interfaces – Perspectives for soil research*, Jena, Germany, Sept. 06 – 07, 2009.

B. Klebow and A. Meleshyn. Monte-Carlo-Simulation der Adsorption quartärer Ammoniumtenside an Muskovit. Poster presentation at *GDCh-Wissenschaftsforum Chemie 2009*, Frankfurt, Germany, Aug. 30 – Sept. 02, 2009.

B. Klebow and A. Meleshyn. Monte Carlo Simulation of Quaternary Alkylammonium Surfactant Adsorption on Muscovite Mica. Talk at *XIV International Clay Conference*, Castellaneta Marina, Italy, June 14 – 20, 2009.



## Acknowledgements

It is a pleasure to thank the many people who made this work possible. First of all, I would like to express my gratitude to Prof. Dr. Rolf Michel for providing excellent working conditions at the institute and giving me the opportunity to complete my thesis. I am grateful to Dr. Artur Meleshyn, the head of our former working group, for his guidance and support over the past years. For his assistance in calculating the refined geometries and the charge distributions of the organic cations, I would like to thank Dr. Henryk Wicke. For proofreading parts of this manuscript I would like to thank Dr. Artur Meleshyn, Dr. Henryk Wicke, Christian Gräf, Dr. Beate Riebe, Christoph Mahrtdt, and Christoph Affeldt. Furthermore, I would like to thank my colleagues at the IRS for the great working atmosphere and many inspiring discussions. The vast majority of the calculations presented in this work were performed on the Central Services Information Technology compute cluster. The support of the RRZN compute cluster team is gratefully acknowledged.